
Electronic Thesis and Dissertation Repository

2-1-2024 2:30 PM

Analyses For Assessing The Centreline Translation, Asymmetrical Wind-Field, And Velocity Fluctuations Of Tornado Vortices

Niall C. Bannigan, *Western University*

Supervisor: Savory, Eric, *The University of Western Ontario*

Co-Supervisor: Orf, Leigh, *University of Wisconsin-Madison*

A thesis submitted in partial fulfillment of the requirements for the Master of Engineering Science degree in Mechanical and Materials Engineering

© Niall C. Bannigan 2024

Follow this and additional works at: <https://ir.lib.uwo.ca/etd>



Part of the [Environmental Engineering Commons](#), and the [Other Mechanical Engineering Commons](#)

Recommended Citation

Bannigan, Niall C., "Analyses For Assessing The Centreline Translation, Asymmetrical Wind-Field, And Velocity Fluctuations Of Tornado Vortices" (2024). *Electronic Thesis and Dissertation Repository*. 9939. <https://ir.lib.uwo.ca/etd/9939>

This Dissertation/Thesis is brought to you for free and open access by Scholarship@Western. It has been accepted for inclusion in Electronic Thesis and Dissertation Repository by an authorized administrator of Scholarship@Western. For more information, please contact wlsadmin@uwo.ca.

Abstract

Tornadoes present an ever-increasing threat to communities worldwide, especially those with geographic conditions that place them in the path of several tornadoes annually. These conditions are likely to be exacerbated by ongoing trends in the climate. As such, it is necessary to move towards experimental and numerical tornado-like vortex studies that allow for more advanced simulation methods. Novel techniques for tracking and analysing tornado vortices simulated at high spatial and temporal resolution are presented herein. Significant wandering of the tornado's position and large peaks in the velocity field can be captured, demonstrating tangential gusting at more than 1.5 times the conventional peak average value. These gusts were also demonstrated to occur over a wider range of distance from the tornado centre than previous methods would detect. Finally, recommendations for spatial and temporal scaling of the results of conventional analyses are presented to guide the future of tornado-like vortex research.

Keywords Tornado, Vortex modelling, Centre of rotation tracking, Temporal wind-field fluctuations, Spatial wind-field fluctuations, Tornado scaling factors.

Summary for Lay Audience

When reading the word “tornado”, most people would likely imagine a funnel of rotating air touching from the sky to the ground, leaving destruction in its path. Though this may seem simple to replicate in a laboratory or computer model, simulating a realistic tornado is not trivial. There are many types of tornadoes and parameters that characterize their motion. The most notoriously difficult phenomena to capture in simulations are the presence of asymmetry about the vertical axis of rotation and the tilting of the vertical axis resulting from motion of the tornado vortex. Wind engineering studies published today can generate tornado-like vortices but are often not able to replicate these additional complexities or exclude them from their analyses. This work presents novel a method to use tornado velocity wind-fields to pinpoint the location of a vortex’s centre in time and space in a consistent manner. By considering the spatial and temporal variation of the velocity data it is possible to determine not just the average velocity but also its expected range and other statistics. A timescale is defined for the average duration of a rotation of a tornado, which is useful in separating rapid fluctuations from the mean motions. Another scale introduced details how much a tornado’s velocity varies in space from the velocities averaged over the circumference. This permits the use of conventional, simplistic velocity measurements to compute the range of expected velocity values. As a result, the tornadoes produced in any given simulation (so long as there are sufficiently well-resolved data available) would more accurately represent the real-world natural phenomena. This is especially important considering that these simulations are often used to design infrastructure and protect lives in future severe weather events.

Co-Authorship Statement

This thesis is composed of two distinct but related articles of research performed by the present author acting as the primary author with Dr. Eric Savory and Dr. Leigh Orf providing technical advice and feedback on the written work. The data used in the development of the arguments of the research chapters herein are derived from large-scale supercell simulations performed on the National Centre for Supercomputing Applications (NCSA) Blue Waters supercomputer by Dr. Leigh Orf with a modified Bryan Cloud Model, version 1 (CM1) model. These data were classified and tracked by the present author and novel tornado analyses were developed under the supervision of Dr. Eric Savory.

An earlier version of Chapter 2, entitled “Tracking the centre of asymmetric vortices using wind velocity vector data fields”, is published in *Boundary-Layer Meteorology* and is currently accessible on the internet as of 1 January, 2023. This chapter has been adapted for this thesis.

A version of Chapter 3, entitled “Quantifying the asymmetry in tornado vortex wind-fields using numerical simulations of supercell thunderstorms”, is to be submitted to the *Journal of Wind Engineering and Industrial Applications* following this thesis’ submission.

The final chapter of this thesis, Chapter 4, is a summary of the two preceding chapters and also includes recommendations for future work on the present datasets and tornado-like vortex research generally.

Dedication

I would like to dedicate this thesis to Emilia, for always reminding that I am on the right path when I feel most lost.

Acknowledgements

I should like to wholeheartedly thank Dr. Eric Savory for always refining my work to reveal its best aspects from the very first time I met him in the classroom as an undergraduate to my completion of this Master of Engineering Science graduate degree. It has been a long journey and Dr. Eric Savory has been eternally patient with my careful attention to detail. Many thanks to Dr. Leigh Orf for providing such complex and beautiful datasets to work on; the unique opportunity was worth the many months of challenging analyses. I have learnt so much about data handling and visualization, entirely inspired by his dedication to both of these often neglected steps in research.

I should also like to thank the ever-evolving Advanced Fluid Mechanics group, to be one of its members for so long has been a privilege and an honour. I extend particular thanks to Mr. Dwaipayan Sarkar, Ms. Shivani Jariwala, Mr. Nicholas Dudalski, and Mr. Kyle Graat for your warm welcome to the group as a young undergraduate and for your continual friendship. I learned much from watching you all and receiving your feedback over the years. Additionally, I should like to thank Mr. Haoran Du for encouraging me to take frequent breaks for exercise, banter, and thoughtful discussion.

I should also like to thank Ms. Emilia Krzeminska and Mr. Jakob Wilk for helping me to perform tedious data sorting and saving tasks when I was failing to find the time for them myself, this favour will never be forgotten.

I should like to express my gratitude to my parents for being patient with my continuously shifting timelines and erratic schedule during my time in both undergraduate and graduate degrees and providing me shelter and nourishment during that time. I will channel this support into the fruitful future you both have envisioned for me.

Finally, this work would not have been possible without the funding provided by the Natural Sciences and Engineering Research Council (NSERC) of Canada and the Ontario Graduate Scholarship (OGS) Program and I am honoured to have received their support.

Table of Contents

Abstract	ii
Summary for Lay Audience	iii
Co-Authorship Statement	iv
Dedication	v
Acknowledgements	vi
Table of Contents	vii
List of Tables	x
List of Figures	xi
List of Appendices	xvi
List of Nomenclature	xvii
1 Introduction	1
1.1 A General Discussion of Tornadoes	1
1.1.1 Analytical Modelling	2
1.1.2 Tornado Vortex Chambers	4
1.1.3 Laboratory-Scale Computational Fluid Dynamics Modelling	6
1.1.4 Field Data Collection	8
1.1.5 Full-Scale Computational Fluid Dynamics Modelling	10
1.1.6 Summary of Published Literature	12
1.2 Motivation	12
1.3 Objectives	15

1.4	Thesis Layout	16
	References	18
2	Tracking the Centre of Asymmetric Vortices...	32
2.1	Introduction	32
2.1.1	Background of Tornado Modelling	33
2.1.2	Vortex Centre Identification Methods	35
2.1.3	Tornado Centre Identification	43
2.2	Methodology Details	44
2.2.1	Data Processing	45
2.3	Results and Discussion	51
2.3.1	Results	51
2.3.2	Comparisons of Methods	53
2.4	Conclusions and Recommendations	57
	References	59
3	Quantifying the Asymmetry in Tornado Vortex Wind-Fields...	65
3.1	Introduction	65
3.1.1	Vortex Models	67
3.1.2	Tornado Vortex Chambers	69
3.1.3	Data Sources	72
3.1.4	Objectives of the Present Study	73
3.2	Methodology	74
3.2.1	Data Processing	74
3.2.2	Coordinate Conversion	78
3.2.3	Variability of Velocity Profiles	81
3.2.4	Maximum-to-Average Velocity Ratio	83
3.2.5	Spatial-Peak Factor	83

3.2.6	A Vortex Timescale	84
3.2.7	Turbulence Analysis	84
3.2.8	Fixed Probe Analysis	87
3.3	Results and Discussion	88
3.4	Conclusions	110
	References	113
4	Concluding Remarks	123
4.1	Summary and Conclusions	123
4.1.1	Tracking the Centre of Asymmetric Vortices	125
4.1.2	Quantifying the Asymmetry in Tornado Vortex Wind-Fields	126
4.2	Contributions	129
4.3	Recommendations for Future Work	130
	Appendices	132
	Curriculum Vitae	144

List of Tables

1.1	Overview of key characteristics found in tornado analysis methods in the literature	13
2.1	Summary of main characteristics of previous vortex identification methods .	38
2.2	Comparison of the time taken to analyze a given horizontal plane of the tornado by previously developed vortex tracking methods with the proposed method	53
3.1	Summary of referenced tornado data (with the year of simulation provided in parentheses) extracted from numerically simulated supercell thunderstorms	73
3.2	Summary of lifespan of the main vortex in each tornado dataset. All times are given with respect to the initial time, t'_1 s, in each dataset	78
3.3	Summary of the studies with equivalent S and the heights and radii over which velocity profile data are available	82
3.4	Summary of the present data characteristics. The core radius, r_c , and tangential velocity at r_c , $u_t(r_c)$, were the average values over the height of the domain and the range in each represents the variation with respect to time .	90
B.1	Comparison of the number of times the program failed to find a loop about a centre and/or interpolate for a centre using different c values	138

List of Figures

1.1	The velocity profile of a Rankine combined vortex model, showing the solid body rotation core that transitions to a freely decaying outer region at radius, r_c , where tangential velocity, u_t , is a maximum	2
1.2	A generic schematic representation of an experimentally or computationally simulated TVC with updraft radius r_{out} , inlet height h , domain height H , and domain radius R . They commonly feature an axisymmetric inlet, sometimes dependent on height, and a constant vertical velocity outlet . . .	4
2.1	Labelled example of a vortex tangential velocity profile after normalization	34
2.2	Near-surface storm-relative horizontal wind-field vectors at $t = 5579$ s in the simulated tornado analyzed in the present work, indicating a snapshot in time where the tornado vortex was highly asymmetric	36
2.3	Coordinate system schematic showing the vertical vorticity component of a point of interest, O , on the horizontal plane	37
2.4	Schematic diagram representing the direction spanning vortex identification method in [39]. (a) Defining four vector label ranges (A–D) based on orientation and (b) example vector-field with an identified core region using a structured Cartesian grid system	41
2.5	Cylindrical coordinate system conversion schematic	45

2.6	Finding the centre of an asymmetric vortex system using artificial data for illustrative purposes as an example where $n_s = 5$. (a) Schematic example of tornado dataset with vectors (shown as black arrows) on an isotropic grid (shown as dashed lines), (b) 5 vectors (shown in red) selected based on n_s , (c) lines perpendicular to the selected vectors' orientation drawn (shown in blue), (d) identified intersections of each line drawn (shown as green squares), (e) location of average intersection identified (shown as white circle), and (f) nearest vector identified (shown in red) and nearest vectors from identified vector that complete a loop (shown in blue) then used to interpolate for the location of zero-velocity (shown as white circle)	47
2.7	Schematic view of vortex region case checking where the red circles indicate the data points. Complete rotation loop in (a) one of the four quadrants, (b) left or right halves, (c) top or bottom halves, and (d) the entire area	50
2.8	Plan view of the tornado following the centre at $z = 15$ m a.g.l. throughout the entire life cycle of the vortex from $t_1 = 5000$ s to $t_2 = 6300$ s. The motion of the vortex centre is shown relative to the dataset domain boundaries (moving at $(u_{m,x}, u_{m,y}) = (10.5, 15.2)$ m·s ⁻¹) and relative to the ground. Note that	52
2.9	Comparison of the accuracy of various methods in tracking the vortex core centre on a representative wind-field data sample at $t = 5687$ s and $z = 165$ m a.g.l. The † in the figure legend represents methods that identify a region and ‡ represents those that identify point locations	54
3.1	Schematic representation of a Rankine vortex's tangential velocity profile after scaling the velocity by maximum u_t and radius by r_c for three different heights scaled as $\hat{z} = z/r_c$	70
3.2	Trace of the (a) T ₁ , (b) T ₂ , and (c) T ₃ tornado centre positions through time on each xy-plane slice of data	76

3.3	Variation of the maximum absolute tangential wind velocity relative to the ground for all tornado datasets. The labels identify events of significance that occurred over the duration of each tornado life-cycle	77
3.4	Demonstration of the differences in cylindrical coordinate spacing when using equal arc length spacing (shown as red circles) versus equal angular spacing (shown as dark-blue dots) for (a) at $\hat{r} = 0.1$, (b) at 1.0, and (c) at 5.0	79
3.5	Schematic of the coordinate transformation, shown for the velocity components	80
3.6	Plan-view, schematic representation of tower probe placement and motion relative to a tornado centre that is also in motion relative to the reduced domain inside a larger, simulation domain	88
3.7	Comparison of the normalized profiles of spatially averaged tangential velocities present in various tornado vortices at height and time slices representative of the time series of each tornado	90
3.8	Demonstration of the spread of the normalized profiles of spatially averaged tangential velocities. The shaded region indicates the range of normalized velocity bounded by the average value \pm one standard deviation	92
3.9	The ratio, \hat{U}_t , of the peak maximum tangential velocity, $\langle u_t \rangle$, present in the entire tornado to the peak circumferential average tangential velocity, u_t , at $\hat{z} \approx$ (a) 0.00, (b) 0.50, and (c) 1.00 plotted against time	94
3.10	Time averaged statistics of the ratio of the peak maximum tangential velocity present in the entire tornado to the peak circumferential average tangential velocity over all heights	95
3.11	The variation of the spatial peak factor, κ , (see Eq. 3.15) with time at $\hat{z} \approx$ (a) 0.00, (b) 0.50, and (c) 1.00	97
3.12	Time averaged statistics of the spatial peak factor over all heights	98

3.13	A visualisation of the change over time of the defined timescale, τ , at $\hat{z} =$ (a) 0.00, (b) 0.50, and (c) 1.00	100
3.14	Time averaged statistics of a timescale computed for each height of each tornado dataset	101
3.15	Temporally smoothed grid-scale and SGS TKE as a proportion of the total TKE averaged over different time-block lengths and shown at various ver- tical and radial locations surrounding the vortex at (a) north, (b) east, (c) south, and (d) west of the tornado centre	105
3.16	Temporally smoothed statistics of the normalized total TKE, \hat{k}_T , averaged over different time-block lengths and shown at various vertical and radial locations surrounding the vortex at (a) north, (b) east, (c) south, and (d) west of the tornado centre	106
3.17	Temporally-smoothed statistics of the TI across different time-block lengths and positions, vertically and radially, surrounding the vortex at (a) north, (b) east, (c) south, and (d) west of the tornado centre	108
3.18	Horizontal velocity magnitude from sensors on a hypothetical tower at $r(t'_{1/2}, z_i = 1) = r_c$	109
A.1	Finding the tornado centre using artificial data for illustrative purposes as an example. (a) Schematic example of tornado dataset with vectors (shown as black arrows) on an isotropic grid (shown as dashed lines), (b) vector components (x in purple and y in blue), (c) location of zero velocity (be- tween x components in purple and y components in blue), (d) interpolated vector components, (e) location of zero horizontal velocity (shown as red circle), and (f) tornado centre location	137

B.1	Comparing the mode of identified tornado centre points, found by varying c , with the failed results of the different c values used. The data shown are taken relative to the simulation domain for all timesteps at height $z = 15$ m a.g.l.	139
C.1	Non-smoothed grid-scale and SGS TKE as a proportion of the total TKE averaged over different time-block lengths and shown at various vertical and radial locations surrounding the vortex at (a) north, (b) east, (c) south, and (d) west of the tornado centre	140
C.2	Non-smoothed statistics of the normalized total TKE, \hat{k}_T , averaged over different time-block lengths and shown at various vertical and radial locations surrounding the vortex at (a) north, (b) east, (c) south, and (d) west of the tornado centre	142
C.3	Non-smoothed statistics of the TI across different time-block lengths and positions, vertically and radially, surrounding the vortex at (a) north, (b) east, (c) south, and (d) west of the tornado centre	143

List of Appendices

Appendix A	Summary of Processing Algorithm	132
Appendix B	Comparison of Scale Factor, c	138
Appendix C	TKE and TI Analyses Without Temporal Smoothing	140

List of Nomenclature

Latin Letters

\bar{u}_3	Sample skewness
$\bar{u}_{3,m}$	Modified sample skewness
\hat{U}	Ratio of maximum velocity over average velocity component
A	Three-dimensional velocity gradient, s^{-1}
S	Strain-rate tensor, $rad \cdot s^{-1}$
u	Velocity vector, $m \cdot s^{-1}$
v	Eigenvector of the real symmetric tensor component, 1
w	“Reduced” velocity vector, $m \cdot s^{-1}$
A	Area, m^2
a	Logarithmic spiral amplitude, m
b	y-intercept of rotated vector directions, m
b_2	Sample kurtosis
$b_{2,m}$	Modified sample kurtosis
C	Generic constant used in Burgers’ vortex model, $m \cdot s^{-1}$
c	User adjustable scaling parameter, 1
f	General function, used in Sullivan’s vortex model

H	Domain height, m
h	Height, m
I	Turbulent intensity, $\text{m}\cdot\text{s}^{-1}$
k	Turbulent kinetic energy, $\text{m}^2\cdot\text{s}^{-2}$
l	Length, m
m	Slope of rotated vector directions, 1
N	Number of points remaining after a filtering operation, 1
n	Index counter variable, 1
O	Origin of coordinate system
Q'	Cross-sectional volume flow rate, $\text{m}^2\cdot\text{s}^{-1}$
R	Domain radius, m
r	Radius, m
S	Swirl ratio, 1
s	Arc length of a curve, m
T	Duration of raw tornado data, s
t	Time, s
u	Velocity component, $\text{m}\cdot\text{s}^{-1}$
w	“Reduced” velocity component, $\text{m}\cdot\text{s}^{-1}$

x	First Cartesian (horizontal) coordinate, m
y	Second Cartesian (horizontal) coordinate, m
z	Third Cartesian (vertical) coordinate, m
T	Indicates the shorthand name of a given tornado dataset

Greek Letters

α	Angle between spiral radius and tangent, rad
β	Dummy integration variable used in $f(r)$
Δ	Modifier to indicate a difference of a given variable
δ	Dummy integration variable used in $f(r)$
Γ	Circulation strength of vortex, $\text{m}^2 \cdot \text{s}^{-1}$
γ	Dummy integration constant used in $f(r)$
κ	Spatial-peak factor, 1
λ	Eigenvalue of the symmetric tensor, $\text{rad}^2 \cdot \text{s}^2$
H	(Normalized) helicity, $\text{m} \cdot \text{s}^{-2}$
∇	Cartesian coordinates differential operator
ν	Kinematic viscosity of the fluid, $\text{m}^2 \cdot \text{s}^{-1}$
ω	Magnitude of vorticity, $\text{rad} \cdot \text{s}^{-1}$
ϕ	Selected filter cut-off for standard deviation computation

Ψ	Rotated vector tips area span, m^2
ψ	Projection of α for oblique viewing angles, rad
ρ	Planar viewing angle, rad
σ	Standard deviation of given variable
τ	A timescale for rotation of a tornado vortex, s
θ	Azimuthal position, rad
Ω	Spin tensor, $\text{rad}\cdot\text{s}^{-1}$
ω	Vorticity vector, $\text{rad}\cdot\text{s}^{-1}$

Superscripts

-	Temporal average operator
^	Normalized value operator (often in relation to r_c)
+	Modifier of Ψ to increase area of centre search
$\langle \rangle$	Spatial average operator
$\lceil \rceil$	Round up operator
$\lfloor \rfloor$	Round to nearest value operator
$\lfloor \rfloor$	Round down operator
'	Relating to the temporal region of interest
T	Matrix transpose operator

Subscripts

1	Start of a series or the first component of a variable (or dataset)
1/2	Halfway in a series of values
2	End of a series or the second component of a variable (or dataset)
3	The third component of a variable (or dataset)
<i>b</i>	Indicating a block of time over which turbulence analyses occur
<i>c</i>	Relating to the core radius where the average u_t value is a maximum
<i>I</i>	Related to number of filtered intersections
<i>i</i>	Index of matrix or dimension of vector
<i>j</i>	First alternative matrix index or vector dimension
<i>k</i>	Second alternative matrix index or vector dimension
<i>O</i>	Relating to the centre of a frame of reference
<i>r</i>	Radial component
<i>t</i>	Tangential component
<i>w</i>	Temporal window index size
<i>x</i>	First Cartesian (horizontal) component
<i>y</i>	Second Cartesian (horizontal) component
<i>z</i>	Vertical Cartesian or cylindrical component

B	Relating to Burgers' vortex model
in	Relating to the inlet of a (TVC) domain
int	Relating to the intersection point of two lines in the centre search process
m	Relating to the motion needed for a tornado to stay within a domain's limits
out	Relating to the outlet of a (TVC) domain
R	Relating to Rankine's vortex model
S	Relating to Sullivan's vortex model
s	Scaling factor
T	Total TKE quantity
tower	Relating to the "probe tower" analysis
W	Relating to Wen's vortex model

Abbreviations

ABL	Atmospheric boundary-layer
BC	Boundary condition
CFD	Computational fluid dynamics
CM1	(Brian) Cloud Model, version 1
EF	Enhanced Fujita (scale)
F	Fujita (scale)

IC	Initial condition
LES	Large-eddy simulation
NCSA	National Center for Supercomputing Applications
NTP	Northern Tornadoes Project
PIV	Particle-image velocimetry
RANS	Reynolds-averaged Navier-Stokes
RMS	Root-mean-square
SGS	Sub-grid scale
TBL	Tornado boundary-layer
TI	Turbulent intensity
TKE	Turbulent kinetic energy
TVC	Tornado vortex chamber

Chapter 1

1 Introduction

This chapter will cover basic tornado mechanics, their simulation, and the relevance of their study, as well as lay out the thesis contents.

1.1 A General Discussion of Tornadoes

Though there are many ways to define a tornado, it is widely understood to be a rapidly rotating column that connects a cloud, often a cone-shaped funnel cloud, to the ground and which forms, under appropriate conditions, in the natural environment [1]. Tornadoes are classified by the damage they produce, which can be roughly translated into an equivalent wind speed. This is known as the Enhanced Fujita (EF) scale, which originated as the Fujita (F) scale [2] before developing into its current but still evolving form today. The EF scale uses wind speed estimates of a three-second gust to classify tornadoes from 0–5: 90–130, 135–175, 180–220, 225–260, 270–310, and 315+ kilometres-per-hour, respectively [3] (in the U.S.A., these classifications are defined in miles-per-hour [4]).

Regulatory codes often do specify the wind speeds from tornado flows that buildings must be able to withstand if the failure of that structure poses at least moderate risk to human life and it is located in a tornado prone region [5]. These standards prescribe calculations for different categories of buildings depending on their purpose and geographic location that determine the maximum wind speed a building can withstand. Damage from a tornado of EF 3 or higher begins to enter the “total devastation” range [6], which may be prohibitively expensive to attempt to prepare for. This, and the fact that the vast majority of tornadoes recorded are of EF 1 and below [7], explains why preparedness for tornadic events tends to focus on events of an EF 2 rating or below for most communities. This is also why EF 2 is often the limit of tornado-like vortex simulations in both experimental and numerical test

facilities for wind engineering.

A review of the published literature on tornado modelling and field data collection methods found in meteorological and wind engineering studies is presented in the following sections. This includes an examination of several techniques (and their limitations) associated with tornado data derived from field measurements and models developed through analytical, experimental, small-scale numerical and full-scale meteorological simulations. A summary of the defining features of each of these tornado analysis methods is found in Table 1.1.

1.1.1 Analytical Modelling

Analytical modelling was the earliest method used to model vortices, although, it was not initially used for tornadoes in particular. The most well-known analytical model for a tornado is the Rankine combined vortex model [8], which has a forced inner, inviscid region of circulation with an abrupt transition to an exponential decaying velocity region (Fig. 1.1).

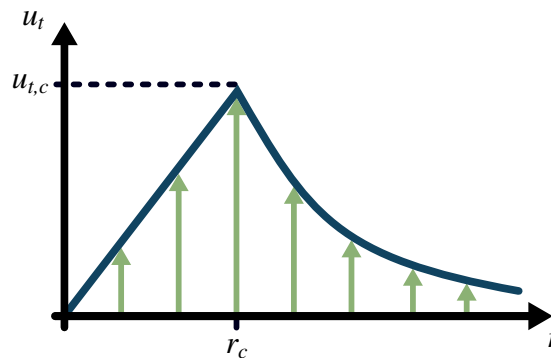


Figure 1.1: The velocity profile of a Rankine combined vortex model, showing the solid body rotation core that transitions to a freely decaying outer region at radius, r_c , where tangential velocity, u_t , is a maximum

The radius of maximum tangential velocity, r_c , is a commonly referenced position in tornado analysis and only includes the maximum circumferentially averaged tangential veloc-

ity. This model assumes symmetry of the vortex shape around the axis of rotation (axisymmetry), which occurs because only the tangential velocity is modelled, not the radial or vertical components, and the velocity is not dependent on the angular position, θ . The Rankine combined vortex model is, however, still used for validation in many tornado modelling studies (e.g., [9–11]) because it matches observations made above the tornado boundary-layer (TBL) where the tangential velocity dominates [12]. Another common axisymmetric vortex model (not specifically for tornadoes), is that of Burgers [13] and Rott [14], which solves the Navier-Stokes equations to obtain three-dimensional velocity and pressure fields. Sullivan [15] added a free-slip condition for the ground boundary and introduced a second cell to the vortex, meaning the core region had a flow reversal that was separate from the flow outside, with vertical sheaths of flow at the core (as observed by Hoecker [16]) and a downdraft at the central axis. Although Burgers [13], Rott [14], and Sullivan [15] produced more complex vortex models than Rankine [8] before them, Kuo's [12] axisymmetric method is preferred because it models a tornado, rather than a generic vortex, and included three-dimensional equations that were simplified by Wen [17] and Wen and Ang [18] for use in engineering studies. These models demonstrated large radial inflow inside the core and also introduced a dependence on height with respect to the TBL for all three velocity components. Whilst Jischke and Parang's [19] model considers an azimuthal dependence, it does so only briefly before averaging around the circumference when discussing the results. Later studies focus on applying the tornado model to wind-loading by considering the velocity and pressure distributions found within a tornado (e.g., [9, 20, 21]). This does not, however, resolve the discrepancy between both axisymmetry and fixed axis assumptions and what is observed in nature. A no-slip boundary interaction with the ground surface is also commonly assumed (e.g., [17, 22, 23]) or a constant stress sub-layer with a slip layer on top is applied [24]. However, Davies-Jones and Wood [10] applied a free-slip condition because it resulted in a tornado that more closely resembled the conditions seen in a real event. Overall, the analytical models must force a tornado velocity or pressure distribution

rather than permit one to develop naturally because they are, for the most part, steady-state analyses without the time-dependent boundary conditions (BCs) for the inflow components expected for a real tornado-like vortex. Even though Baker and Sterling [23] successfully included temporal fluctuations in the velocity field to model debris trajectories, it remains a steady-state and axisymmetric model.

1.1.2 Tornado Vortex Chambers

Testing theories about vortex formation, stability, motion, and wind-loading effects has frequently utilised a tornado vortex chamber (TVC). A proof-of-concept TVC was introduced by Ying and Chang [25] where a rotating mesh screen (2.00 m in diameter) at the periphery added angular momentum to air being pulled in via an exhaust fan at the top of the 2.44 m chamber (Fig. 1.2).

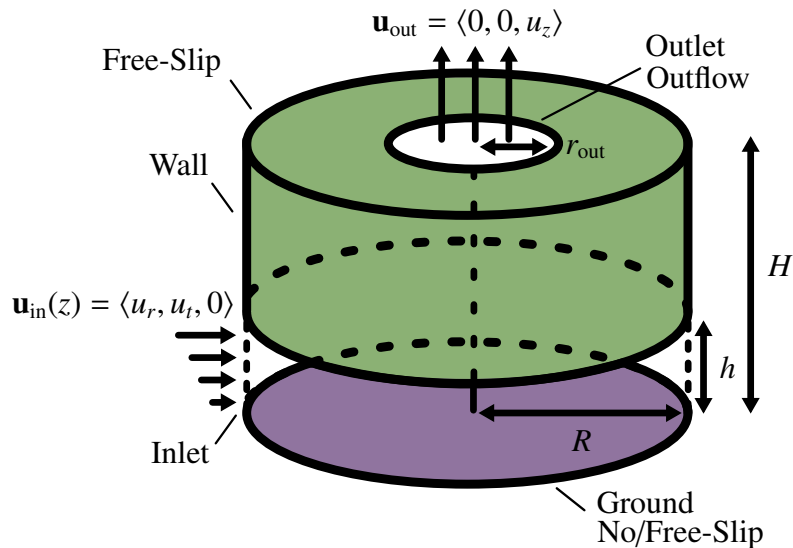


Figure 1.2: A generic schematic representation of an experimentally or computationally simulated TVC with updraft radius r_{out} , inlet height h , domain height H , and domain radius R . They commonly feature an axisymmetric inlet, sometimes dependent on height, and a constant vertical velocity outlet

In such a setup, the total inflow is related to the total outflow such that both cross-sectional

flow rates are equivalent. A simple definition for this value, based on Fig. 1.2, is

$$Q' = 2\pi R h \mathbf{u}_{\text{in}} = \pi r_{\text{out}}^2 \mathbf{u}_{\text{out}} \quad (1.1)$$

The original TVC design was developed further in [26] where a large collection area and a mesh were added to straighten the outflow. For the inflow, Church *et al.* [27] decoupled the circulation within the chamber from the circulation beyond it. This TVC type remains known as the Ward-type simulator and is very common in experimental tornado-like vortex simulation (e.g., [20, 28–33]). Wan and Chang [34] used a slightly larger form of Ying and Chang’s [25] TVC to generate a more realistic two-celled vortex with both up- and down-drafts and the ability to measure the three-dimensional flow-field. Subsequently, Baker [30] added a second, vertical hot-wire film probe to analyse the vertical and horizontal kinematic profiles. In [35], the hot-wires were able to rotate about the TVC vertical axis but an azimuthal dependence was not considered. More recently, non-intrusive particle-image velocimetry (PIV) provided two-dimensional planes of data from a single camera sensor, producing much more detailed and resolved information about the flow-field (e.g., [36–39]). This method may be extended to use multiple cameras for more advanced vortex structure analysis [40]. Further improvements to the TVC design included adding a section of translating ground to provide control of the axial tilt and including either a rough ground texture for more realistic ground interaction [31] or a heated bed for analysis of thermal boundary effects [35]. The latter study also replaced the rotating mesh found in the original Ward-type TVC design with fans installed ahead of the inflow to impart circulation. Mishra *et al.* [41] used slotted vanes rather than fans for smoother and more stable vortex generation. Haan *et al.*’s [42] TVC permitted the motion of the entire vortex generator by a crane arm with height control over a large ground surface. However, the most versatile and large-scale TVC to-date is the WindEEE dome with a 25.0 m diameter convection chamber that permits simulation of vortices up to 5.0 m in diameter (i.e., $2r_c$), significantly larger than

any other TVC available [43]. This simulator is similar in design to the original Ward-type except that several fan arrays are placed at the periphery to impart various symmetric and asymmetric flow patterns with a much higher fidelity than previously possible. However, in each of the aforementioned TVCs, the location of the centre of a tornado vortex and whether it was wandering, had asymmetry, or had axial tilt was not or could not be determined due to a lack of interest or limitations of their set-ups. Diamond and Wilkins [31] noted that the tilt and translation of the tornado simultaneously enhanced the wind speed on one side of the vortex while diminishing it on the other; Zhang and Sarkar [37] and Refan and Hangan [40] noted that vortex wandering, especially at low swirl, had the same effect. It should be clear that whilst several of these studies highlighted the discrepancy between tornadic loading and straight-line boundary flows on infrastructure (e.g., [20, 36, 44]), the additional spatial-temporal variation of kinetic energy in a tornado can be, in part, attributed to its centre wandering, asymmetric flow, and axial tilting.

1.1.3 Laboratory-Scale Computational Fluid Dynamics Modelling

Recently, computational-fluid dynamics (CFD) modelling has become the dominant method to produce and analyse tornadoes. CFD domains usually model existing or planned TVC configurations to assess the influence of different swirl ratios, inlet/outlet conditions, or ground roughness parameters (e.g., [45–47]). A cylindrical domain of a given radius and height of a laboratory-scale TVC was common for this reason, with the inlet as part of the radial boundary, which was set to constant angular rotation with no actual inlet flow (e.g., [45, 46, 48–50]) or to constant tangential and radial (inwards) velocity (e.g., [47, 51–55]). The inflow velocity, \mathbf{u}_{in} , sometimes depended on height but seemingly never on θ . A circular cut-out in the chamber top plate was often set as a pressure outflow or constant vertical velocity outlet (other components set to zero). The remaining sections of the wall and top plate were often free-slip. Finally, the floor was set up as a no-slip ground (e.g., [46, 47, 52–58]) or, to prevent vortex instability and (counter-intuitively)

align more closely with the results of TVC experiments [46, 48, 52], a free-slip may be used (e.g., [45, 48, 51]). This setup is summarized in Fig. 1.2, in the previous section. Early CFD simulations forced axisymmetry about the vertical axis in the solution of the Navier-Stokes equations and used a simple two-dimensional vertical slice domain (e.g., [45, 46, 48–52, 59]) but did not necessarily exclude the azimuthal velocity component. These simulations needed to make such assumptions to conserve the limited available computing power at their respective times; for example, around 3×10^4 cells of constant size in Rotunno’s [46] model in 1979 compared to 1.8×10^6 in Gairola and Bitsuamlak’s [58] model 40 years later. However, the overall domain size did not change much in this time as it was often desired to replicate the findings of a specific laboratory experiment. Given that several decades have passed since some of these studies, some limitations have been largely mitigated. However, post-processed analyses in many CFD studies still focus on horizontal planes of temporally and circumferentially averaged data (e.g., [47, 53–58, 60]). Although this was necessary for quantitative comparisons, averaging over space and time neglects much of the flow physics including smaller sub-vortices or excessive maximum velocities nearly double the average tangential velocities that may occur far outside of r_c (e.g., [61–63]). Selvam and Millett [59] note that, compared to a straight-line atmospheric boundary-layer (ABL) flow, a tornado vortex applied almost double the loading to a structure when measured from the same locations for a steady-state analysis. This is dependent on the section of the vortex impacting a given structure, but if the translation of a tornado is also taken into account, it is possible to achieve tilting of the vortex and thereby greater asymmetry. Thus, there is potential for a higher magnitude of loading [54, 61, 63] in certain areas over others, which could not be identified in a time-averaged or spatially-smoothed dataset. Although the relationship between asymmetry and wind-loading effects does not necessarily exhibit unbounded growth to infinity [60], the CFD studies that permit such realism observed large pressure differences. This was still true across a short distance, particularly when interacting with a structure or ground roughnesses that caused sub-vortices

to form [64], even though it may also reduce the average tangential velocity [55].

1.1.4 Field Data Collection

For tornadoes to be simulated or modelled accurately, there must be both qualitative and quantitative sources of data against which the tornado structure and the velocity or pressure fields may be compared. Observing tornado events in nature is the preferred method of building databases to help researchers improve their simulation capabilities [65]. Methods of obtaining data from tornado events include damage surveys (e.g., [66]), photogrammetry (e.g., [67]), weather station probes (e.g., [66]), mobile weather stations (e.g., [68]), and Doppler radar (e.g., [69]). Damage surveys are not able to directly quantify the wind speeds and pressure profiles of interest in the present work and, therefore, are not discussed further here. Photogrammetry is where single images, successive photographs, or videos are used to trace the motion of prominent particles (i.e., large debris) in a tornado vortex to obtain information about the kinematics, vortex motion, or tilt. This method is useful in that the shape and size of the vortex funnel cloud can provide context to probe- and radar-derived data [70, 71]. However, it is limited in that fully three-dimensional information requires at least two camera perspectives [72] and particles are unlikely to be numerous enough to fully capture the velocity and pressure fields, especially the maximum and minimum values [67]. From photogrammetry techniques, it was observed that tornadoes changed in shape with time, tilted significantly from the vertical axis (but only high above the ground, e.g., over 900 m in [66]), and demonstrated intense vertical mixing within the core wall radius, r_c [70]. Weather station probes, both fixed and mobile, are useful for capturing data at a given location but when compared with Doppler radar techniques, which can penetrate the vortex cloud to measure storm strength rapidly, give only very crude point-location information. However, they are useful for providing a datum to compare with Doppler radar-derived kinematic data (e.g., [68, 70, 73–75]). Donaldson [69] demonstrated how a tornado centre position may be identified by a single Doppler radar setup but requires

the assumption that the vortex is both axisymmetric and circular in its horizontal cross-section—an assumption also made by [65, 76–80]. Additionally, Brown *et al.* [76] showed that if the size of the vortex is known, it is possible to determine the maximum velocity of the tornado vortex and develop a tangential velocity profile. Tilting of the vertical axis of the tornado can be detected with this method, as demonstrated in [73, 76, 79–81], though only far above the ground (e.g., at a height of 500 m in [80]). The tilting was not neglected in these studies but dealt with by re-aligning the horizontal slices of data onto a vertical axis such as in [73, 81]. It was often the case that asymmetry of the tornado was detected but had to be neglected as the radial (with respect to the radar system) velocity could not be quantified (e.g., [68, 69, 71, 73, 74, 77, 81]). Other Doppler radar studies did not have this issue but still opted to neglect the asymmetry (e.g., [65, 79, 80]) or were only able to measure it via probe instruments (e.g., [71, 81] noted a $10 \text{ m}\cdot\text{s}^{-1}$ wind speed radial velocity component). Wood and Brown [77] theorised that asymmetry could be accounted for by using multiple radar beams but Lee *et al.* [78] demonstrated that, by taking advantage of the velocity gradient of the signal, only one beam was required in certain cases, however, this still required the assumption of a nearly circular plan-view profile. Further, Markowski *et al.* [74, 75] noted the complexity of a real-life tornado where they observed multiple vortices combining around a common axis to form a larger vortex. This further highlights the problem with assuming the tornado vortex has a simple, circular cross-section when trying to assess the vortex’s damage potential based on radial distance from the tornado centre. A similar issue arises when utilising the swirl ratio, conventionally defined as

$$S = \frac{r_{\text{out}}\Gamma}{2Q'h} \quad (1.2)$$

where r_{out} is the radius of the updraft region, Γ is the circulation value at r_{out} , Q' is the volumetric flow rate through the updraft cross-section, and h is the height of the inflow region (see Fig. 1.2). Karstens *et al.* [68] showed that relying on S results in discrepan-

cies between the predicted and actual damage of a simulated vortex versus a real tornado measured at an equivalent value of S . Thus, S alone cannot determine the vortex structure without better resolved, near surface measurements. Kosiba and Wurman [73] and Wurman *et al.* [71] attempted to address this issue and the former noted that the height of the maximum tangential velocity was near to or at the top of the TBL. Conversely, Kosiba and Wurman [81] and Refan *et al.* [65] found it to be well within the TBL, with the former finding that the upper edge of the TBL was very near to the ground at around 10 m in their particular case. Wurman *et al.* [70] attempted to capture the entire life-cycle of a tornado by using more than 55 radars to maintain a minimum of two signals at all times and, thus, directly derive velocity information. By implementing all of the field data techniques discussed in this section, it is possible to validate tornado modelling techniques by capturing actual tornadoes' initial conditions (ICs), BCs, and TBL data, and, from the photogrammetric data, ensure that any tornado-like vortex produced demonstrates tilting, translation, and asymmetry comparable to its natural counterpart.

1.1.5 Full-Scale Computational Fluid Dynamics Modelling

Meteorologists do not have the same objectives as wind engineers when it comes to producing tornadoes using CFD techniques and this is reflected in the model setup. Meteorological CFD models represent an effort to model tornadoes at full-scale by including the effects of precipitation and buoyancy in the system of equations (e.g., [82–84]). Early studies (e.g., [82–85]) used two-dimensional and axisymmetric domains just as the early CFD studies did, which was also a result of the computational limitations at the time. These simulations were within domains of approximately $24 \times 24 \times 10$ km, which ensured the tornado intensity was not restricted [86], with grid spacings of around 0.5 to 1.0 km at 10 s timesteps [83]. They also used a staggered grid of the different variables in the domain so that the computational efficiency was higher (e.g., [82]). However, these domains have grown significantly to the order of $1000 \times 1000 \times 100$ km and beyond (e.g., [87–92]) to

allow tornadic supercell formation with minimal IC and BC forcing. However, it should be noted that only recently has the finest resolution within these domains been comparable to that of the engineering-focused models: from 8960 cells in Walko’s [84] 1988 study or approximately 8.28×10^5 in Wicker and Wilhelmson’s [93] in 1995 (a three-dimensional domain) to over 2.51×10^{11} with minimum grid spacing of 10 m in Orf’s [90] in 2019. The domain setup for a meteorologically informed simulation, in general, involved a free-slip boundary for the top and ground surfaces and an open boundary at the horizontal edges (e.g., [83–85, 87, 89, 90, 92–95]). Some studies instead used a no-slip BC for the ground layer (e.g., [82, 88, 96–98]) or for the lateral boundary [e.g., 99]. However, they are rare in meteorological studies because the full-scale vortices generated from no-slip BCs resulted in too much interaction between the flow above the upper edge of the TBL and the flow within it [84], single-cell flows created by a large updraft [85], and a much more rapid vortex decay than anticipated [87]. Additionally, these same studies also required more velocity forcing at the domain limits than the studies that did not use the no-slip BC to generate a tornado. Wicker and Wilhelmson [93] noted that higher resolution at the ground level would be required to achieve a no-slip tornado that avoided the issues outlined previously. In [82] and [93], a solid-body rotation cloud was set at a given swirl, based on field observation, and the temperature, pressure, and precipitation equations manifested a vortex flow because the rotation caused an updraft due to low pressure suction. However, Wicker and Wilhelmson [93] and Markowski [100] also had an initial thermal bubble, which rises up to encourage convection from surface to cloud. Alternatively, Naylor and Gilmore [95] found that it was not realistic to use this thermal bubble and instead used an initial updraft “nudging” technique where a vertical velocity IC was gently induced in a specified region terminating once the wind speed reached $10 \text{ m}\cdot\text{s}^{-1}$. This technique was also used in [89]. Schenkman *et al.* [87], Orf [92], Mashiko [101], and Li *et al.* [102] found that rainfall onto a near-ground vortex rotating about an axis parallel to the ground instigated vertical lift of the axis of rotation leading to a tornado. Many studies (e.g., [83, 87, 89–91, 93–98, 100–

103]) added in sub-grid turbulence modelling to account for the dissipation of energy from the grid-scale large eddies to the small-scale. It was also found that the release of latent heat by falling rain crucially influences tornado formation.

1.1.6 Summary of Published Literature

In many of the studies described here, and summarised in the following table (Table 1.1), the focus on realistic tornado formation results in detailed representation of characteristics observed in nature (described previously in the field data review) such as multiple vortices, vortex translation, vortex tilting, and asymmetrical flow (e.g., [87, 89, 90, 92–97, 100–103]).

1.2 Motivation

Tornadoes are a globally understood threat, having been recorded on every continent save for Antarctica [104]. Tornado touchdowns are more prevalent around the middle latitudes, both North and South, due to the favourable conditions for formation. For example, Oklahoma, U.S.A. consistently records the most and largest tornado outbreaks in the American continent, in part due to its position relative to the equator but also due to geographical factors [105]. Unsurprisingly, the U.S.A. has one of the longest and most rigorous tornado tracking databases in the world, with partial (but decidedly unreliable) accounts dating back to the late 19th century (retroactively restored through projects such as [106]) and official and methodical tracking beginning in the 1980s with data recovered back to the 1950s [6]. This growing database of tornado outbreak knowledge has shown that the number of tornadoes detected per outbreak has been on the rise since the start of the National Weather Service database [107]. However, this is also attributable to the increase of public awareness allowing for greater forecasting (see [108]) and is mostly constrained to tornadoes of an EF rating between 0 and 1 [7, 109]. Though it is difficult to determine the long

Table 1.1: Overview of key characteristics found in tornado analysis methods in the literature

Data Source	Common Assumptions	Boundary Treatment	Pros	Cons
Analytical	Axisymmetric velocity and shape, steady, vertical axis, and fixed location	No-slip, forced rotation, and uniform inflow	Can use validated fluid dynamics formulae	Difficult to incorporate realistic ICs and BCs
TVC	Axisymmetric velocity, circumferential averaging, tilting negligible, and centre wandering negligible	Forced rotation, outlet suction, and no angular dependence	Realistic ground interaction, safe observation of real flows, and wind-load testing	Limited ability to measure variables and expensive to modify model parameters
Lab-Scale CFD	Axisymmetric velocity, circumferential averaging, and forcing vortex artificially	No-slip ground, free-slip walls, tangential and radial velocity inlet, and vertical velocity outlet/outflow	Possible to take measurements throughout domain and rapidly adjust model parameters	Accuracy of results limited by domain size and IC/BC influence
Field	Axisymmetric velocity and shape and point readings are representative	N/A	Can physically look at the tornado and take any desired readings	Hard to intercept tornadoes, data is distorted by relative position to vortex, high risk to researchers, and expensive
Full-Scale CFD	Forcing of ICs are negligible and can initiate accurate tornado with thermal bubble/updraft nudging	Free-slip ground, open radiative walls, and slight swirl imposed at ceiling	Possible to take measurements throughout domain, far-field BC analyses, and results closely match field observations	Considerable computing power required and cannot currently highly resolve near to the ground

term direction of such a trend, it is clear that the potential for tornado formation becomes more likely as the average global temperature rises, leading to greater vortex intensity, a longer active season, and the occurrence of tornadic events in regions that previously had not experienced significant tornadoes [110].

Canada is one of several countries that has recently experienced many minor tornado events. They are most often found in Ontario and parts of Québec, hazardous enough to be newsworthy and leaving behind, collectively, hundreds of millions of dollars in damage and many people injured (e.g., [111–114]). The ability to report on and confirm the presence of tornadoes after they have passed, especially in some of the extremely remote regions in Canada that are affected, is only possible due to the efforts of the Northern Tornadoes Project (NTP). As with the databases available in the U.S.A., it takes time to collate historic and ongoing data and synthesize coherent observations of trends in tornado occurrence and prevalence. However, it is clear that the majority of tornadoes occurring in Canada are at the EF 2 or lower level (see [115]) with none (yet) recorded to extend far above this as in the U.S.A. Also, while the costs associated with the damage done by tornadoes do not historically reach into the billions of dollars as in the U.S.A. [6], the insurance payouts related to extreme weather have been moderately increasing in the most recent decade [116]. Given that, for the time being, there is no clear, globally consistent increase in higher EF rating tornadoes beyond the EF 2 category, countries seeing upticks in severe weather events leading to larger payouts should find methods to develop infrastructure and public works projects to withstand many minor- to moderate-strength tornadic events. However, to develop and implement such methods, it is crucial to ensure adequate knowledge transfer from theoretical analyses performed on analytical, experimental, or numerical simulations where a complete wind-field dataset is not possible from field measurements alone (as detailed previously in Sect. 1.1.4). This would mean precisely tracking the life-cycle of tornadoes and generating reliable and robust data on the damage expected from a future severe weather event. In the field of meteorology, numerical simulations of supercell

thunderstorms that cover vast areas of land (discussed in Sect. 1.1.5) have been the norm for many years but only recently have allowed for finer scales of analysis comparable to that of laboratory TVC experiments or numerical models. This fine-scale data computed over large domains requires development in the techniques used to analyse tornadoes so that the improved accuracy of the simulations can be fully exploited.

1.3 Objectives

There exists a plethora of published literature on analyses of simulated and real tornado wind-field datasets. However, to ensure informed infrastructure design in the face of climate instability and potential increases in the number of severe storm events, the analyses must be reliable. In the meteorologically-informed simulations used for the work presented herein, the high spatial and temporal resolution of the data presents a unique challenge compared to conventional tornado simulation data. Firstly, the domain is much larger than what would be expected of a TVC and, as such, the tornado's shape and motion is unpredictable. Secondly, the unsteady nature of the flow-field means that time and space averaging of the data must be carefully considered. Finally, there are many unknowns to the data; while they can be analysed on a scale similar to that of wind engineering studies, they are produced with very different ICs and BCs and, as such, should be investigated without *a priori* assumptions as to how the data “should” look. Therefore, it is intended that this body of work shall resolve the following:

- a) Is it possible to firmly designate a datum position of radius, $r = 0$, for tornadoes demonstrating asymmetry about the vertical axis,
- b) Can this tracking through space and time be applied quickly and reliably no matter the input dataset,
- c) Is consideration of spatial and/or temporal variation in the dataset flow-field quanti-

ties important, and

- d) To what extent can all of these modifications to the conventional tornado analyses found throughout published literature actually be useful to wind engineering experiments where it is not possible to simulate full-scale and meteorologically accurate tornado vortices?

1.4 Thesis Layout

High spatio-temporal resolution tornado wind-field data derived from large-scale and meteorologically accurate supercell thunderstorm simulations are analysed in two chapters to achieve the objectives described previously. The data analysed are only the velocity data with a focus on the tangential component, once they have been converted from the given Cartesian coordinate domain. The resolution of the data is not consistent across datasets and as such shall be described, in detail, in the subsequent chapters. This thesis is written in the “integrated article” format that is comprised of two complete bodies of research that have been collated here.

In the first, the method used to take an isometric grid-spacing tornado dataset and convert it into a spatially consistent cylindrical-coordinate-based domain is presented. This work allows minimal input from a user and minimal *a priori* adjustments to the program presented to achieve the results shown.

In the second of the two following chapters, the method from the first is applied to three tornado datasets of different levels of complexity and resolutions with success. This allows for in-depth analysis of the temporal and spatial variations present within each case of vortices. Further, these data are used to generate representative scaling factors for current, less extensive tornado and tornado-like vortex datasets. The techniques used to analyse the tornadoes are novel though not exhaustive, providing inspiration for future work in

generating more accurate and reliable simulations of tornadoes in the wind engineering field.

References

- [1] American Meteorological Society (AMS), “Glossary of meteorology,” Nov. 2020. Accessed: Dec. 28, 2023. [Online.] Available: <https://glossary.ametsoc.org/wiki/Tornado>
- [2] T. T. Fujita, *Proposed characterization of tornadoes and hurricanes by area and intensity*. Dept. Geophys. Sci., Univ. Chicago, 1971, vol. 91, p. 42.
- [3] Environment and Climate Change Canada (ECCC), “Enhanced Fujita scale for wind damage,” Sep. 2018, Accessed: Nov. 28, 2023. [Online.] Available: <https://www.canada.ca/en/environment-climate-change/services/seasonal-weather-hazards/enhanced-fujita-scale-wind-damage.html>
- [4] National Weather Service (NWS), “The Enhanced Fujita scale (EF scale),” National Oceanic and Atmospheric Administration (NOAA), Jan. 2023. Accessed: Nov. 28, 2023. [Online.] Available: <https://www.weather.gov/oun/efscale>
- [5] *Minimum Design Loads and Associated Criteria for Buildings and Other Structures*, ASCE/SEI 7-22. American Society of Civil Engineers, Reston, U.S.A., 2022.
- [6] National Centers for Environmental Information (NCEI), “Storm events database,” National Oceanic and Atmospheric Administration (NOAA), July 2023. Accessed: May 20, 2023. [Online.] Available: <https://www.ncdc.noaa.gov/stormevents/>
- [7] S. M. Verbout, H. E. Brooks, L. M. Leslie, and D. M. Schultz, “Evolution of the U.S. tornado database: 1954–2003,” *Weather and Forecasting*, vol. 21, no. 1, pp. 86–93, 2006.
- [8] W. Rankine, *Motions of fluids–hydrodynamics*. Charles Griffin and Company, London, 1877, pp. 574–577.

- [9] Y. Aboelkassem, G. H. Vatistas, and N. Esmail, “Viscous dissipation of Rankine vortex profile in zero meridional flow,” *Acta Mechanica Sinica*, vol. 21, pp. 550–556, 2005.
- [10] R. P. Davies-Jones and V. T. Wood, “Simulated Doppler velocity signatures of evolving tornado-like vortices,” *Journal of Atmospheric and Oceanic Technology*, vol. 23, no. 8, pp. 1029–1048, 2006.
- [11] V. T. Wood and R. A. Brown, “Simulated tornadic vortex signatures of tornado-like vortices having one- and two-celled structures,” *Journal of Applied Meteorology and Climatology*, vol. 50, no. 11, pp. 2338–2342, 2011.
- [12] H. L. Kuo, “Axisymmetric flows in the boundary layer of a maintained vortex,” *Journal of Atmospheric Sciences*, vol. 28, no. 1, pp. 20–41, 1971.
- [13] J. Burgers, “A mathematical model illustrating the theory of turbulence,” vol. 1, pp. 171–199, 1948.
- [14] N. Rott, “On the viscous core of a line vortex,” *Zeitschrift für Angewandte Mathematik und Physik ZAMP*, vol. 9, pp. 543–553, 1958.
- [15] R. D. Sullivan, “A two-cell vortex solution of the Navier-Stokes equations,” *Journal of the Aerospace Sciences*, vol. 26, no. 11, pp. 767–768, 1959.
- [16] W. H. Hoecker, “Three-dimensional pressure pattern of the Dallas tornado and some resultant implications,” *Monthly Weather Review*, vol. 89, no. 12, pp. 533–542, 1961.
- [17] Y.-K. Wen, “Dynamic tornadic wind loads on tall buildings,” *ASCE Journal of the Structural Division*, vol. 101, no. 1, pp. 169–185, 1975.
- [18] Y. Wen and A. Ang, “Tornado risk and wind effect on structures,” in *Proceedings*

- of the Fourth International Conference on Wind Effects on Buildings and Structures, London, U.K., 1975, pp. 63–74.*
- [19] M. C. Jischke and M. Parang, “Properties of simulated tornado-like vortices,” *Journal of Atmospheric Sciences*, vol. 31, no. 2, pp. 506–512, 1974.
- [20] B. H. Fiedler and R. Rotunno, “A theory for the maximum windspeeds in tornado-like vortices,” *Journal of Atmospheric Sciences*, vol. 43, no. 21, pp. 2328–2340, 1986.
- [21] E. Savory, G. A. Parke, M. Zeinoddini, N. Toy, and P. Disney, “Modelling of tornado and microburst-induced wind loading and failure of a lattice transmission tower,” *Engineering Structures*, vol. 23, no. 4, pp. 365–375, 2001.
- [22] Z. Xu and H. Hangan, “An inviscid solution for modeling of tornadolike vortices,” *Journal of Applied Mechanics*, vol. 76, no. 3, pp. 031 011–1–5, Mar. 2009.
- [23] C. Baker and M. Sterling, “Modelling wind fields and debris flight in tornadoes,” *Journal of Wind Engineering and Industrial Aerodynamics*, vol. 168, pp. 312–321, 2017.
- [24] H. Kuo, “Vortex boundary layer under quadratic surface stress,” *Boundary-Layer Meteorology*, vol. 22, pp. 151–169, 1982.
- [25] S. J. Ying and C. C. Chang, “Exploratory model study of tornado-like vortex dynamics,” *Journal of Atmospheric Sciences*, vol. 27, no. 1, pp. 3–14, 1970.
- [26] N. B. Ward, “The exploration of certain features of tornado dynamics using a laboratory model,” *Journal of Atmospheric Sciences*, vol. 29, no. 6, pp. 1194–1204, 1972.
- [27] C. R. Church, J. T. Snow, and E. M. Agee, “Tornado vortex simulation at Purdue

- Univ.” *Bulletin of the American Meteorological Society*, vol. 58, no. 9, pp. 900–909, 1977.
- [28] G. L. Baker and C. R. Church, “Measurements of core radii and peak velocities in modeled atmospheric vortices,” *Journal of Atmospheric Sciences*, vol. 36, no. 12, pp. 2413–2424, 1979.
- [29] C. R. Church, J. T. Snow, G. L. Baker, and E. M. Agee, “Characteristics of tornado-like vortices as a function of swirl ratio: A laboratory investigation,” *Journal of Atmospheric Sciences*, vol. 36, no. 9, pp. 1755–1776, 1979.
- [30] G. L. Baker, “Boundary layer in laminar vortex flows,” Ph.D. dissertation, Purdue Univ., West Lafayette, IN, U.S.A., 1981.
- [31] C. J. Diamond and E. M. Wilkins, “Translation effects on simulated tornadoes,” *Journal of Atmospheric Sciences*, vol. 41, no. 17, pp. 2574–2580, 1984.
- [32] Z. Tang, C. Feng, L. Wu, D. Zuo, and D. L. James, “Characteristics of tornado-like vortices simulated in a large-scale ward-type simulator,” *Boundary-Layer Meteorology*, vol. 166, pp. 327–350, 2018.
- [33] Z. Tang, D. Zuo, D. James, Y. Eguchi, and Y. Hattori, “Experimental study of tornado-like loading on rectangular prisms,” *Journal of Fluids and Structures*, vol. 113, p. 103672, 2022.
- [34] C. A. Wan and C. C. Chang, “Measurement of the velocity field in a simulated tornado-like vortex using a three-dimensional velocity probe,” *Journal of Atmospheric Sciences*, vol. 29, no. 1, pp. 116–127, 1972.
- [35] Y. Mitsuta and N. Monji, “Development of a laboratory simulator for small scale atmospheric vortices.” *Natural Disaster Science*, vol. 6, no. 1, pp. 43–54, 1984.

- [36] P. Hashemi Tari, R. Gurka, and H. Hangan, “Experimental investigation of tornado-like vortex dynamics with swirl ratio: The mean and turbulent flow fields,” *Journal of Wind Engineering and Industrial Aerodynamics*, vol. 98, no. 12, pp. 936–944, 2010.
- [37] W. Zhang and P. P. Sarkar, “Near-ground tornado-like vortex structure resolved by particle image velocimetry (PIV),” *Experiments in Fluids*, vol. 52, pp. 479–493, 2012.
- [38] M. Refan, “Physical simulation of tornado-like vortices,” Ph.D. dissertation, Univ. Western Ontario, London, ON, Canada, 2014.
- [39] M. Refan and H. Hangan, “Characterization of tornado-like flow fields in a new model scale wind testing chamber,” *Journal of Wind Engineering and Industrial Aerodynamics*, vol. 151, pp. 107–121, 2016.
- [40] M. Refan and H. Hangan, “Near surface experimental exploration of tornado vortices,” *Journal of Wind Engineering and Industrial Aerodynamics*, vol. 175, pp. 120–135, 2018.
- [41] A. R. Mishra, D. L. James, and C. W. Letchford, “Physical simulation of a single-celled tornado-like vortex, part a: Flow field characterization,” *Journal of Wind Engineering and Industrial Aerodynamics*, vol. 96, no. 8, pp. 1243–1257, 2008.
- [42] F. L. Haan, P. P. Sarkar, and W. A. Gallus, “Design, construction and performance of a large tornado simulator for wind engineering applications,” *Engineering Structures*, vol. 30, no. 4, pp. 1146–1159, 2008.
- [43] H. Hangan, “The Wind Engineering Energy and Environment (WindEEE) Dome at Univ. Western Ontario, Canada,” *Wind Engineers, Japan Association for Wind Engineering*, vol. 39, no. 4, pp. 350–351, 2014.

- [44] F. L. Haan, V. K. Balaramudu, and P. P. Sarkar, “Tornado-induced wind loads on a low-rise building,” *Journal of Structural Engineering*, vol. 136, no. 1, pp. 106–116, 2010.
- [45] R. Rotunno, “Numerical simulation of a laboratory vortex,” *Journal of Atmospheric Sciences*, vol. 34, no. 12, pp. 1942–1956, 1977.
- [46] R. Rotunno, “A study in tornado-like vortex dynamics,” *Journal of Atmospheric Sciences*, vol. 36, no. 1, pp. 140–155, 1979.
- [47] H. Hangan and J. Kim, “Swirl ratio effects on tornado vortices in relation to the Fujita scale,” *Wind and Structures*, vol. 11, no. 4, pp. 291–302, 2008.
- [48] B. H. Fiedler, “Numerical simulation of axisymmetric tornadogenesis in forced convection,” pp. 41–48, 1993.
- [49] D. S. Nolan and B. F. Farrell, “The structure and dynamics of tornado-like vortices,” *Journal of the Atmospheric Sciences*, vol. 56, no. 16, pp. 2908–2936, 1999.
- [50] D. S. Nolan, “A new scaling for tornado-like vortices,” *Journal of the Atmospheric Sciences*, vol. 62, no. 7, pp. 2639–2645, 2005.
- [51] F. H. Harlow and L. R. Stein, “Structural analysis of tornado-like vortices,” *Journal of Atmospheric Sciences*, vol. 31, no. 8, pp. 2081–2098, 1974.
- [52] T. Wilson and R. Rotunno, “Numerical simulation of a laminar end-wall vortex and boundary layer,” *The Physics of Fluids*, vol. 29, no. 12, pp. 3993–4005, Dec. 1986.
- [53] L. Kuai, F. L. Haan Jr, W. A. Gallus Jr, and P. P. Sarkar, “CFD simulations of the flow field of a laboratory-simulated tornado for parameter sensitivity studies and comparison with field measurements,” *Wind and Structures*, vol. 11, no. 2, pp. 75–96, 2008.

- [54] D. Natarajan and H. Hangan, “Large eddy simulations of translation and surface roughness effects on tornado-like vortices,” *Journal of Wind Engineering and Industrial Aerodynamics*, vol. 104-106, pp. 577–584, 2012.
- [55] A. Gairola, G. T. Bitsuamlak, and H. M. Hangan, “An investigation of the effect of surface roughness on the mean flow properties of “tornado-like” vortices using large eddy simulations,” *Journal of Wind Engineering and Industrial Aerodynamics*, vol. 234, p. 105348, 2023.
- [56] T. Ishihara, S. Oh, and Y. Tokuyama, “Numerical study on flow fields of tornado-like vortices using the LES turbulence model,” *Journal of Wind Engineering and Industrial Aerodynamics*, vol. 99, no. 4, pp. 239–248, 2011.
- [57] Z. Liu, C. Zhang, and T. Ishihara, “Numerical study of the wind loads on a cooling tower by a stationary tornado-like vortex through LES,” *Journal of Fluids and Structures*, vol. 81, pp. 656–672, 2018.
- [58] A. Gairola and G. Bitsuamlak, “Numerical tornado modeling for common interpretation of experimental simulators,” *Journal of Wind Engineering and Industrial Aerodynamics*, vol. 186, pp. 32–48, 2019.
- [59] R. P. Selvam and P. C. Millett, “Computer modeling of tornado forces on a cubic building using large eddy simulation,” *Journal of the Arkansas Academy of Science*, vol. 57, no. 1, pp. 140–146, 2003.
- [60] A. Sengupta, F. L. Haan, P. P. Sarkar, and V. Balaramudu, “Transient loads on buildings in microburst and tornado winds,” *Journal of Wind Engineering and Industrial Aerodynamics*, vol. 96, no. 10, pp. 2173–2187, 2008.
- [61] T. Ishihara and Z. Liu, “Numerical study on dynamics of a tornado-like vortex with touching down by using the LES turbulence model,” *Wind and Structures*, vol. 19, no. 1, pp. 89–111, 2014.

- [62] Z. Liu and T. Ishihara, “Numerical study of turbulent flow fields and the similarity of tornado vortices using large-eddy simulations,” *Journal of Wind Engineering and Industrial Aerodynamics*, vol. 145, pp. 42–60, 2015.
- [63] Z. Liu and T. Ishihara, “Study of the effects of translation and roughness on tornado-like vortices by large-eddy simulations,” *Journal of Wind Engineering and Industrial Aerodynamics*, vol. 151, pp. 1–24, 2016.
- [64] S. Verma, R. Panneer Selvam, Z. Tang, and D. Zuo, “Comparison of tornado-induced pressures on building from CFD model with TTU experimental measurements,” *Journal of Wind Engineering and Industrial Aerodynamics*, vol. 228, p. 105076, 2022.
- [65] M. Refan, H. Hangan, J. Wurman, and K. Kosiba, “Doppler radar-derived wind field of five tornado events with application to engineering simulations,” *Engineering Structures*, vol. 148, pp. 509–521, 2017.
- [66] T. T. Fujita, U.S.A. Weather Bureau, and Univ. Chicago, “A detailed analysis of the Fargo tornadoes of June 20, 1957,” *U.S.A. Government Printing Office*, vol. 30, 1960.
- [67] W. H. Hoecker, “Wind speed and air flow patterns in the Dallas tornado of April 2, 1957,” *Monthly Weather Review*, vol. 88, no. 5, pp. 167–180, 1960.
- [68] C. D. Karstens, T. M. Samaras, B. D. Lee, W. A. Gallus, and C. A. Finley, “Near-ground pressure and wind measurements in tornadoes,” *Monthly Weather Review*, vol. 138, no. 7, pp. 2570–2588, 2010.
- [69] R. J. Donaldson, “Vortex signature recognition by a Doppler radar,” *Journal of Applied Meteorology and Climatology*, vol. 9, no. 4, pp. 661–670, 1970.

- [70] J. Wurman, D. Dowell, Y. Richardson, P. Markowski, E. Rasmussen, D. Burgess, L. Wicker, and H. B. Bluestein, “The second verification of the origins of rotation in tornadoes experiment: VORTEX2,” *Bulletin of the American Meteorological Society*, vol. 93, no. 8, pp. 1147–1170, 2012.
- [71] J. Wurman, K. Kosiba, and P. Robinson, “In situ, Doppler radar, and video observations of the interior structure of a tornado and the wind–damage relationship,” *Bulletin of the American Meteorological Society*, vol. 94, no. 6, pp. 835–846, 2013.
- [72] G. S. Forbes and H. B. Bluestein, “Tornadoes, tornadic thunderstorms, and photogrammetry: A review of the contributions by T. T. Fujita,” *Bulletin of the American Meteorological Society*, vol. 82, no. 1, pp. 73–96, 2001.
- [73] K. Kosiba and J. Wurman, “The three-dimensional axisymmetric wind field structure of the Spencer, South Dakota, 1998 tornado,” *Journal of the Atmospheric Sciences*, vol. 67, no. 9, pp. 3074–3083, 2010.
- [74] P. Markowski, Y. Richardson, J. Marquis, J. Wurman, K. Kosiba, P. Robinson, D. Dowell, E. Rasmussen, and R. Davies-Jones, “The pretornadic phase of the Goshen County, Wyoming, supercell of 5 June 2009 intercepted by VORTEX2. Part I: Evolution of kinematic and surface thermodynamic fields,” *Monthly Weather Review*, vol. 140, no. 9, pp. 2887–2915, 2012.
- [75] P. Markowski, Y. Richardson, J. Marquis, R. Davies-Jones, J. Wurman, K. Kosiba, P. Robinson, E. Rasmussen, and D. Dowell, “The pretornadic phase of the Goshen County, Wyoming, supercell of 5 June 2009 intercepted by VORTEX2. Part II: Intensification of low-level rotation,” *Monthly Weather Review*, vol. 140, no. 9, pp. 2916–2938, 2012.

- [76] R. A. Brown, L. R. Lemon, and D. W. Burgess, “Tornado detection by pulsed Doppler radar,” *Monthly Weather Review*, vol. 106, no. 1, pp. 29–38, 1978.
- [77] V. T. Wood and R. A. Brown, “Effects of radar proximity on single-Doppler velocity signatures of axisymmetric rotation and divergence,” *Monthly Weather Review*, vol. 120, no. 12, pp. 2798–2807, 1992.
- [78] W.-C. Lee, B. J.-D. Jou, P.-L. Chang, and S.-M. Deng, “Tropical cyclone kinematic structure retrieved from single-Doppler radar observations. Part I: Interpretation of Doppler velocity patterns and the GBVTD technique,” *Monthly Weather Review*, vol. 127, no. 10, pp. 2419–2439, 1999.
- [79] P. M. Markowski, T. P. Hatlee, and Y. P. Richardson, “Tornadogenesis in the 12 May 2010 supercell thunderstorm intercepted by VORTEX2 near Clinton, Oklahoma,” *Monthly Weather Review*, vol. 146, no. 11, pp. 3623–3650, 2018.
- [80] H. B. Bluestein, K. J. Thiem, J. C. Snyder, and J. B. Houser, “Tornadogenesis and early tornado evolution in the El Reno, Oklahoma, supercell on 31 May 2013,” *Monthly Weather Review*, vol. 147, no. 6, pp. 2045–2066, 2019.
- [81] K. A. Kosiba and J. Wurman, “The three-dimensional structure and evolution of a tornado boundary layer,” *Weather and Forecasting*, vol. 28, no. 6, pp. 1552–1561, 2013.
- [82] R. E. Eskridge and P. Das, “Effect of a precipitation-driven downdraft on a rotating wind field: A possible trigger mechanism for tornadoes?” *Journal of Atmospheric Sciences*, vol. 33, no. 1, pp. 70–84, 1976.
- [83] J. B. Klemp and R. B. Wilhelmson, “The simulation of three-dimensional convective storm dynamics,” *Journal of Atmospheric Sciences*, vol. 35, no. 6, pp. 1070–1096, 1978.

- [84] R. L. Walko, “Plausibility of substantial dry adiabatic subsidence in a tornado core,” *Journal of Atmospheric Sciences*, vol. 45, no. 16, pp. 2251–2267, 1988.
- [85] P. A. C. Howells, R. Rotunno, and R. K. Smith, “A comparative study of atmospheric and laboratory-analogue numerical tornado-vortex models,” *Quarterly Journal of the Royal Meteorological Society*, vol. 114, no. 481, pp. 801–822, 1988.
- [86] B. H. Fiedler, “On modelling tornadoes in isolation from the parent storm,” *Atmosphere-Ocean*, vol. 33, no. 3, pp. 501–512, 1995.
- [87] A. D. Schenkman, M. Xue, and M. Hu, “Tornadogenesis in a high-resolution simulation of the 8 May 2003 Oklahoma city supercell,” *Journal of the Atmospheric Sciences*, vol. 71, no. 1, pp. 130–154, 2014.
- [88] W. Mashiko, “A numerical study of the 6 May 2012 Tsukuba city supercell tornado. Part I: Vorticity sources of low-level and midlevel mesocyclones,” *Monthly Weather Review*, vol. 144, no. 3, pp. 1069–1092, 2016.
- [89] L. Orf, R. Wilhelmson, B. Lee, C. Finley, and A. Houston, “Evolution of a long-track violent tornado within a simulated supercell,” *Bulletin of the American Meteorological Society*, vol. 98, no. 1, pp. 45–68, 2017.
- [90] L. Orf, “A violently tornadic supercell thunderstorm simulation spanning a quarter-trillion grid volumes: Computational challenges, I/O framework, and visualizations of tornadogenesis,” *Atmosphere*, vol. 10, no. 10, p. 578, 2019.
- [91] N. Snook, M. Xue, and Y. Jung, “Tornado-resolving ensemble and probabilistic predictions of the 20 May 2013 Newcastle–MooreEF5 tornado,” *Monthly Weather Review*, vol. 147, no. 4, pp. 1215–1235, 2019.
- [92] L. Orf, “Modeling the world’s most violent thunderstorms,” *Computing in Science & Engineering*, vol. 23, no. 3, pp. 14–24, 2021.

- [93] L. J. Wicker and R. B. Wilhelmson, “Simulation and analysis of tornado development and decay within a three-dimensional supercell thunderstorm,” *Journal of Atmospheric Sciences*, vol. 52, no. 15, pp. 2675–2703, 1995.
- [94] N. Snook and M. Xue, “Effects of microphysical drop size distribution on tornadogenesis in supercell thunderstorms,” *Geophysical Research Letters*, vol. 35, no. 24, 2008.
- [95] J. Naylor and M. S. Gilmore, “Vorticity evolution leading to tornadogenesis and tornadogenesis failure in simulated supercells,” *Journal of the Atmospheric Sciences*, vol. 71, no. 3, pp. 1201–1217, 2014.
- [96] W. S. Lewellen, D. C. Lewellen, and R. I. Sykes, “Large-eddy simulation of a tornado’s interaction with the surface,” *Journal of the Atmospheric Sciences*, vol. 54, no. 5, pp. 581–605, 1997.
- [97] D. C. Lewellen, W. S. Lewellen, and J. Xia, “The influence of a local swirl ratio on tornado intensification near the surface,” *Journal of the Atmospheric Sciences*, vol. 57, no. 4, pp. 527–544, 2000.
- [98] D. C. Lewellen and W. S. Lewellen, “Near-surface intensification of tornado vortices,” *Journal of the Atmospheric Sciences*, vol. 64, no. 7, pp. 2176–2194, 2007.
- [99] R. Davies-Jones, “Can a descending rain curtain in a supercell instigate tornadogenesis barotropically?” *Journal of the Atmospheric Sciences*, vol. 65, no. 8, pp. 2469–2497, 2008.
- [100] P. M. Markowski, “What is the intrinsic predictability of tornadic supercell thunderstorms?” *Monthly Weather Review*, vol. 148, no. 8, pp. 3157–3180, 2020.
- [101] W. Mashiko, “A numerical study of the 6 May 2012 Tsukuba city supercell tornado.

- Part II: Mechanisms of tornadogenesis,” *Monthly Weather Review*, vol. 144, no. 9, pp. 3077–3098, 2016.
- [102] J. Li, F. Ping, S. Zhou, and X. Shen, “Numerical simulation of a strong tornado in eastern China with different microphysical schemes,” *Atmospheric Science Letters*, vol. 20, no. 2, p. e875, 2019.
- [103] L. Orf, R. Wilhelmson, and L. Wicker, “Visualization of a simulated long-track EF5 tornado embedded within a supercell thunderstorm,” *Parallel Computing*, vol. 55, pp. 28–34, 2016.
- [104] H. Brooks and C. A. Doswell, “Some aspects of the international climatology of tornadoes by damage classification,” *Atmospheric Research*, vol. 56, no. 1, pp. 191–201, 2001, conference on European Tornadoes and Severe Storms.
- [105] S. Daneshvaran and R. E. Morden, “Tornado risk analysis in the U.S.A.” *The Journal of Risk Finance*, vol. 8, no. 2, pp. 97–111, Jan. 2007.
- [106] T. P. Grazulis, *A 110-Year Perspective of Significant Tornadoes*. American Geophysical Union (AGU), 1993, pp. 467–474.
- [107] M. K. Tippett and J. E. Cohen, “Tornado outbreak variability follows Taylor’s power law of fluctuation scaling and increases dramatically with severity,” *Nature Communications*, vol. 7, 2016.
- [108] C. A. Doswell, A. R. Moller, and H. E. Brooks, “Storm spotting and public awareness since the first tornado forecasts of 1948,” *Weather and Forecasting*, vol. 14, no. 4, pp. 544–557, 1999.
- [109] National Weather Service (NWS), “Storm prediction center maps, graphics, and data page,” Mar. 2023. Accessed: Mar. 28, 2023. [Online.] Available: <https://www.spc.noaa.gov/wcm/>

- [110] W. S. Ashley, A. M. Haberlie, and V. A. Gensini, “The future of supercells in the United States,” *Bulletin of the American Meteorological Society*, vol. 104, no. 1, pp. E1–E21, 2023.
- [111] M. Gillis, “May 21 storm Canada’s sixth costliest weather event, Insurance Bureau of Canada says,” *Ottawa Citizen*, Jun. 2022, Accessed: Aug. 3, 2022. [Online.] Available: <https://ottawacitizen.com/news/local-news/may-21-storm-sixth-costliest-weather-event-in-canadian-history-insurance-bureau-of-canada-says>
- [112] T. Raymond, “Storms cause significant damage across eastern Ontario; tornado suspected,” *CTV News*, July 2022. Accessed: Aug. 3, 2022. [Online.] Available: <https://ottawa.ctvnews.ca/storms-cause-significant-damage-across-eastern-ontario-tornado-suspected-1.6001202>
- [113] M. Both, ““just chaos”: Tornado touches down in Talbotville and narrowly misses restaurant, house,” *CBC/Radio-Canada*, Jun. 2023. Accessed: Jun. 15, 2023. [Online.] Available: <https://www.cbc.ca/news/canada/london/just-chaos-tornado-touches-down-in-talbotville-and-narrowly-misses-restaurant-house-1.6876169>
- [114] J. Kanygin, ““looks almost like a meteor crash”: Central Alberta tornado estimated among Alberta’s strongest,” *CTV News*, July 2023. Accessed: July 5, 2023. [Online.] Available: <https://calgary.ctvnews.ca/mobile/looks-almost-like-a-meteor-crash-central-alberta-tornado-estimated-among-alberta-s-strongest-1.6467364>
- [115] N. T. P. (NTP), “Open data for the Northern Tornadoes Project,” Univ. Western Ontario, London, ON, Canada, Nov. 2023. Accessed: Nov. 27, 2023. [Online.] Available: <https://ntpopendata-westernu.opendata.arcgis.com/>
- [116] M. Hadavi, L. Sun, and D. Romanic, “Normalized insured losses caused by windstorms in Québec and Ontario, Canada, in the period 2008–2021,” *International Journal of Disaster Risk Reduction*, vol. 80, p. 103222, 2022.

Chapter 2

2 Tracking the Centre of Asymmetric Vortices Using Wind Velocity Vector Data Fields

2.1 Introduction

Tornadoes are rapidly rotating columns of air spawned by cumuliform clouds such as thunderstorms that make contact with the Earth's surface. The majority of significant tornadoes (i.e., in the range of EF 2 to 5) develop from supercell thunderstorms [1] and, while the most violent tornadoes are the least common, they cause the most damage and fatalities [2]. In the U.S.A., tornadoes have been historically responsible for a significant number of fatalities, approximately 5000 since 1950 [3], and financial losses on the order of billions of dollars. For example, the tornadoes of Mayfield (Kentucky) in December 2021, Nashville (Tennessee) in March 2020, and several southern states in January 2017 were responsible for 93, 25, and 24 deaths and \$3.9, \$1.1, and \$1.2 billion in damage, respectively [4]. For regions where tornadoes are most prevalent, there has been a significant reduction in fatalities over the past several decades as a direct result of improved forecasting and better alerting of the public during severe weather events [5]. Additionally, observational and numerical studies of tornadoes have improved the understanding of their behaviour, allowing for longer tornado warning lead-times [6] and the development of better design codes for buildings to withstand the wind-loading of a tornado [7]. Despite these advances, the available options for accurately pinpointing their paths in advance of their formation are limited, not to mention the tornado warning false alarm rate is about 75% in the United States [8].

2.1.1 Background of Tornado Modelling

Many attempts have been made to develop models for tornadoes—absent their parent storm—to identify the key characteristics of formation, translation, and structural wind-loading generation. Analytical models, often used as reference, include those of Kuo [9] and Wen [10]. Attempts to model tornadoes experimentally include the Ward-type vortex simulator [11], later modified to the Purdue simulator [12], and more recently the large-scale WindEEE dome [13]. Similarly, TVC models have been developed using computer simulation techniques that make use of large-eddy simulation (LES) (e.g., [14]) or Reynolds-averaged Navier-Stokes (RANS) models (e.g., [15]). Recently, cloud model simulations of supercell thunderstorms have been conducted at a high resolution to permit the formation of physically realistic tornadoes within the simulation (e.g., [16]). This contrasts with the much simpler CFD approaches where tornadoes are forced externally by artificially imposed boundary conditions. These physically based, simulated tornadoes exhibit much of the behaviour of observed storms but require massively parallel supercomputers to execute. One such simulation is the subject of the vortex identification and tracking method described herein.

The extraction of useful results from any type of simulated tornado involves comparing between analytical models, chamber models, numerical simulations, and real-world tornadoes to validate and critique the velocity and/or pressure-fields in the data (e.g., [13, 15, 17]). It should be noted that many models are engineering-focused (e.g., [10, 14, 18–20]) and, thus, are idealized, reduced-scale, subsets of the more realistic cloud models found in meteorological research (e.g., [16]). These models neglect the parent storm in simplified, uniform conditions that are imposed at the domain boundaries. To be able to quantitatively compare their results with the work of others at a common scale, researchers must first normalize the tangential velocity, u_t , profiles of the wind-field with respect to the maximum u_t , which can be denoted as \hat{u}_t . It is common practise to then generate a plot (see Fig. 2.1) of these

data with respect to the radial distance, r , normalized to the radius of the maximum u_t (the core), r_c , which can be denoted as \hat{r} . (e.g., [10, 13–15]).

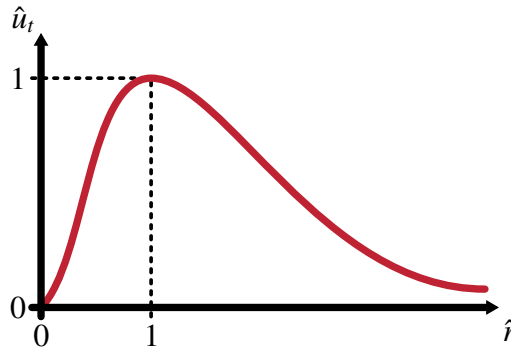


Figure 2.1: Labelled example of a vortex tangential velocity profile after normalization

The concept of plotting the normalized tangential velocity against the normalized radius is derived from the Rankine vortex model [21]. The centre of the vortex is, therefore, located where this ratio is equal to zero and crucial to providing the datum for the velocity profile for tornado analyses. However, this location is usually identified without much consideration of its spatial fluctuation in time as in [22]. Often, it is taken at the geometric centre of the simulation chamber or domain (e.g., [12, 17, 23–26]). These considerations are not an unreasonable omission for axisymmetric—the symmetry about an axis of rotation—and fixed-location models (e.g., [14, 24, 27, 28]) or those where the tornado track is pre-defined along a set path (e.g., [15, 28, 29]) since the position is known by definition. This is especially true for studies that are focused on the accuracy of their analytical model characteristics rather than its direct similarities with atmospheric phenomena in nature (e.g., [2, 9, 10, 17, 18, 23]). The asymmetry and wandering of a tornado may also be considered negligible in laboratory settings at very high swirl ratios because the resulting vortex is rotating fast enough to be stable and well-defined [30]. Thus, the consideration of vortex centre motion does not have a significant effect on the results. In Wan and Chang [31], a physical flow-field demonstrating asymmetry is simplified using a low-pass filtering process with a time constant of eight seconds to generate a temporally

and spatially averaged dataset. In each of these instances, however, the described simplifications may become problematic if the instantaneous flow-field is required such as when determining the peak wind-loading present on a building.

Therefore, this chapter attempts to introduce a more robust and reliable method of tornado centre identification for the cases of non-axisymmetric and non-stationary tornadoes, both real-world and simulated. This does not mean, however, that the method will not also function for the more simplistic axisymmetric and stationary cases. The necessity of developing such a method can be seen in cases such as Fig. 2.2, where the centre of the tornado cannot clearly be identified with simplistic methods such as taking the core radius to outline the centre [20, 32] without additional processing or user-intervention. The data in Fig. 2.2 are a snapshot of the near-surface vector-field of the simulated tornado, analyzed herein, and demonstrate that the higher resolution data available in more advanced simulations allow for higher precision in the tracking of tornado centres.

In this chapter, the technique described is for identifying the centre of rotation as a series of point locations both spatially and temporally within a tornado. This will aid future work in understanding tornado translation and the damage potential relative to their centre. Additionally, a thorough description is provided of other methods to track vortices with comparisons to the proposed one that demonstrates, for these well-resolved and highly accurate tornado simulations, the improved robustness, consistency, and precision.

2.1.2 Vortex Centre Identification Methods

More in-depth methods than those mentioned in the previous section for finding the centre of a tornado programmatically have been reported. For example, the use of the local maximum of the vertical component of the vorticity magnitude, ω_z , (see Fig. 2.3). This is found in [33] and considers the velocity derivatives on a hexahedral cell domain as part of a selection scheme (successfully used in [13]). Additionally, Potvin [34] uses ω_z to identify

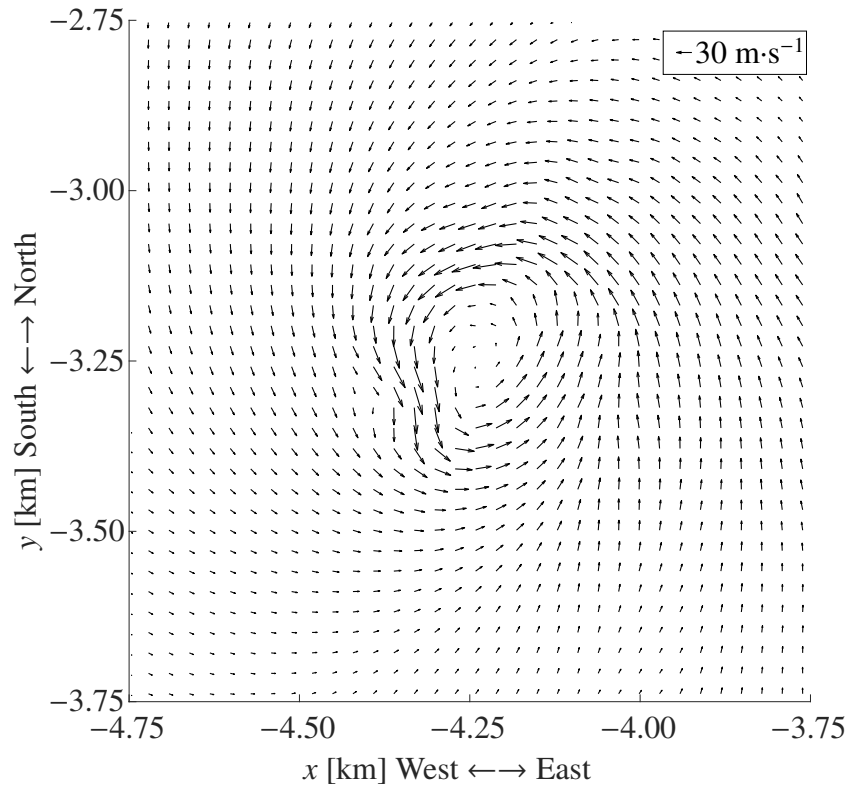


Figure 2.2: Near-surface storm-relative horizontal wind-field vectors at $t = 5579$ s in the simulated tornado analyzed in the present work, indicating a snapshot in time where the tornado vortex was highly asymmetric

regions containing potential vortices and then separates out the flow from possible vortices. Potvin [34] does this using a modified Rankine vortex model and a cost function that, when minimized, indicates a strong relation between the wind-field and the model data. Another example is Aboelkassem *et al.*'s [35] application of a definition (specifically to tornado flows) that states that the vortex centre should be where the tangential velocity, pressure gradient, and vorticity gradient are all zero.

However, tornado-specific analysis has rarely involved more detailed methods of vortex core tracking such as those found in [36–40]. In order to rigorously track a vortex spatially and temporally it becomes necessary to use such methods and so they are employed here for comparison with the method proposed in the present work. Table 2.1 summarizes the following discussion of the methods described above.

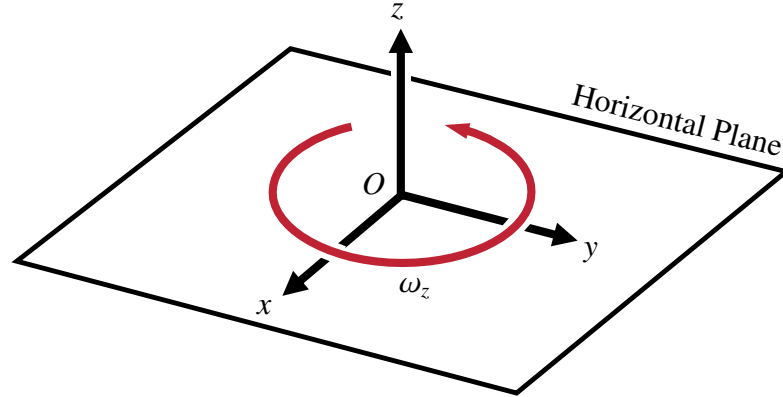


Figure 2.3: Coordinate system schematic showing the vertical vorticity component of a point of interest, O , on the horizontal plane

Levy *et al.* [36] used the normalized helicity, \hat{H} , of the wind-field to identify vortex structures. This scalar quantity is calculated for any given region of interest with

$$\hat{H} = \frac{\mathbf{u} \cdot \boldsymbol{\omega}}{|\mathbf{u}| |\boldsymbol{\omega}|} \quad (2.1)$$

where $\boldsymbol{\omega}$ is the vorticity given by

$$\boldsymbol{\omega} = \nabla \times \mathbf{u} = \left(\frac{\partial u_z}{\partial y} - \frac{\partial u_y}{\partial z} \right) \hat{\mathbf{i}} + \left(\frac{\partial u_x}{\partial z} - \frac{\partial u_z}{\partial x} \right) \hat{\mathbf{j}} + \left(\frac{\partial u_y}{\partial x} - \frac{\partial u_x}{\partial y} \right) \hat{\mathbf{k}}. \quad (2.2)$$

Additionally, $\mathbf{u} = u_x \hat{\mathbf{i}} + u_y \hat{\mathbf{j}} + u_z \hat{\mathbf{k}}$ is the wind-field velocity vector where u_x , u_y , and u_z are the wind speeds in the x , y , and z directions, respectively. Equation 2.1 represents the cosine of the angle between \mathbf{u} and $\boldsymbol{\omega}$ such that when it is small the vectors are assumed by Levy *et al.* [36] to be inside the vortex core. Therefore, \hat{H} should be equal to $+1$ or -1 at the centre point. This has the potential to function well for cases of multiple vortices as it can select all points that have such a \hat{H} value. However, in [36] it is noted that the angle between \mathbf{u} and $\boldsymbol{\omega}$ is not necessarily small.

Jeong and Hussain [37] introduced the λ_2 method for two- or three-dimensional velocity-fields, where λ_2 is the second eigenvalue of their derived symmetric tensor, $\mathbf{S}^2 + \boldsymbol{\Omega}^2$, for

Table 2.1: Summary of main characteristics of previous vortex identification methods

Analysis Method	Benefits	Drawbacks
Levy et al. (1990)	Simple analytical relation Able to handle multiple vortices	Requires 3D data analysis Criterion for detection is not necessarily true for all vortices Identifies a line of vorticity
Jeong and Hussain (1995)	Simple analytical relation Able to handle multiple vortices	Cannot distinguish clustered vortices Identifies a core region only
Sujudi and Haimes (1995)	Uses mathematical relation Capable of identifying vortex as a point	Requires 3D data analysis
Jiang et al. (2002)	Simple criterion, easily implemented No specific data grid type Capable of identifying vortex as a point Able to handle multiple vortices	Cannot distinguish clustered vortices without expensive iteration process
Wong and Yip (2009)	Able to handle skewed data grids Identifies vortex as a point	Requires extensive user input to function at all

vortex identification. This method is based on the assumption that a vortex centre can be identified using local pressure minimum. Jeong and Hussain [37] went further by only using this definition as a starting point for the cases where a pressure minimum may appear without a vortex or a vortex may appear without a pressure minimum. They defined the strain-rate tensor, \mathbf{S} , as

$$\mathbf{S} = \frac{1}{2} (\nabla \mathbf{u} + (\nabla \mathbf{u})^T) \quad (2.3)$$

and the spin tensor, $\mathbf{\Omega}$, as

$$\mathbf{\Omega} = \frac{1}{2} (\nabla \mathbf{u} - (\nabla \mathbf{u})^T) \quad (2.4)$$

which are the symmetric and antisymmetric elements, respectively, of the velocity gradient tensor (given for the two-dimensional case):

$$\nabla \mathbf{u} = \begin{pmatrix} \frac{\partial u_x}{\partial x} & \frac{\partial u_y}{\partial x} \\ \frac{\partial u_x}{\partial y} & \frac{\partial u_y}{\partial y} \end{pmatrix}. \quad (2.5)$$

Then, a vortex region is defined where $\lambda_2 < 0$ given that λ_2 is the second largest eigenvalue of the symmetric tensor, which can be expressed according to Chen *et al.* [41] as

$$\lambda_2 = \left(\frac{\partial u_x}{\partial y} \frac{\partial u_y}{\partial x} - \frac{\partial u_x}{\partial x} \frac{\partial u_y}{\partial y} \right) + \frac{1}{2} \left(\frac{\partial u_x}{\partial x} + \frac{\partial u_y}{\partial y} \right)^2 + \frac{1}{2} \left| \frac{\partial u_x}{\partial x} + \frac{\partial u_y}{\partial y} \right| \sqrt{\left(\frac{\partial u_x}{\partial x} - \frac{\partial u_y}{\partial y} \right)^2 + \left(\frac{\partial u_x}{\partial y} + \frac{\partial u_y}{\partial x} \right)^2}. \quad (2.6)$$

Jeong and Hussain [37] note that this definition of a vortex is versatile and can work for centre identification reliably in several flow-field applications. According to [42], this method is not able to easily identify individual vortices. However, this may be useful in cases where there are many equally powerful vortices clustered together that need to be analyzed as a group to identify the dominant vortex. This method does not identify a point as the vortex centre but, rather, the general region of the vortex core.

Sujudi and Haimes [38] developed an algorithm for checking the divided, three-dimensional regions, or mesh cells, of any shape in a simulation dataset for critical points. The critical points are defined at locations where the slope of the fluid flow streamlines is not definite and the storm-relative velocity is equal to zero. The rate of change of the deformation tensor is computed from the coefficients of a trilinear interpolation function for the fluid

velocity in each direction:

$$\mathbf{A} = \begin{pmatrix} \frac{\partial u_x}{\partial x} & \frac{\partial u_y}{\partial x} & \frac{\partial u_z}{\partial x} \\ \frac{\partial u_x}{\partial y} & \frac{\partial u_y}{\partial y} & \frac{\partial u_z}{\partial y} \\ \frac{\partial u_x}{\partial z} & \frac{\partial u_y}{\partial z} & \frac{\partial u_z}{\partial z} \end{pmatrix}. \quad (2.7)$$

Then, the eigenvalues, λ_i , of the matrix \mathbf{A} are computed and checked such that the critical point search should continue only if there is a real eigenvalue and a pair of complex-conjugate eigenvalues. This is reminiscent of the approach developed by Jeong and Hussain [37], described above. Then, for \mathbf{u} at each node, the eigenvector of the real eigenvalue, \mathbf{v}_i , is subtracted to yield a reduced velocity as

$$\mathbf{w} = \mathbf{u} - \frac{\mathbf{u} \cdot \mathbf{v}_i}{\|\mathbf{v}_i\|^2} \mathbf{v}_i \quad (2.8)$$

where $\|\mathbf{v}_i\|$ is the norm of the eigenvector and each component, w_i , is the equation of a plane. If w_i of just two components is set to 0 then they must intersect, which, for two planes, is a line. Should this line intersect with the cell on two different faces then this implies the cell contains a part of a vortex between the two intersection points. The authors also suggest a more efficient approach whereby the program finds exactly two points on each cell for two different faces where $w = 0$ and uses these to define the line of local swirling flow without compromising accuracy. Orf *et al.* [43] successfully implemented this method and showed that it can identify specific vortex point locations, unlike Jeong and Hussain's [37] method.

Jiang *et al.* [39] developed a combinatorial topology method, utilizing the principle of Sperner's lemma, which is an algorithm for detecting regions of core vortex rotation [44]. The points in an area of interest are labelled according to the range of directions they face, meaning that vectors can be categorized within the wind-field to be compared with other points in a given area (see Fig. 2.4a).

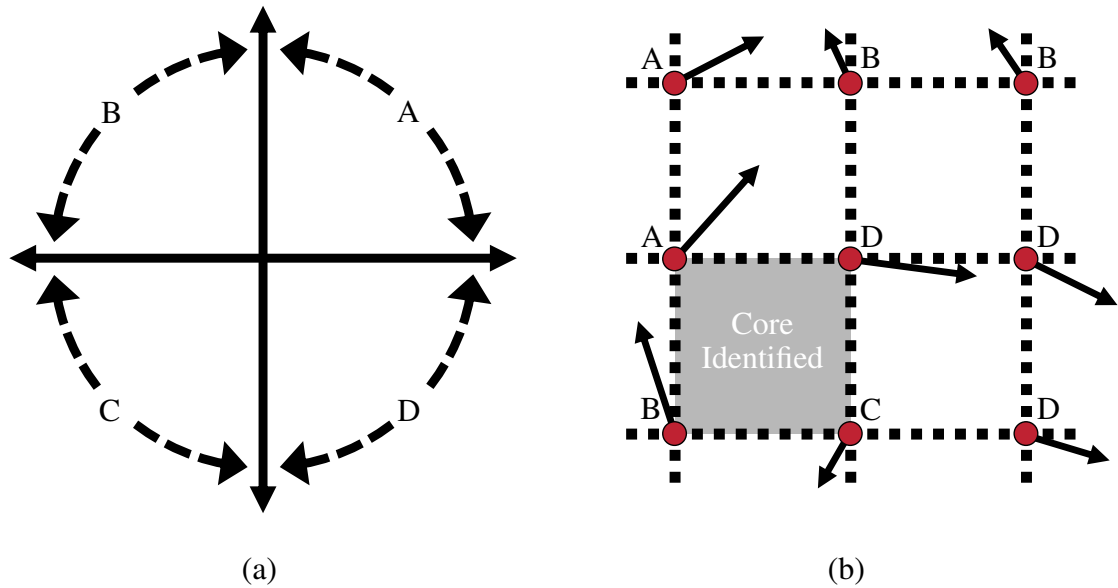


Figure 2.4: Schematic diagram representing the direction spanning vortex identification method in [39]. (a) Defining four vector label ranges (A–D) based on orientation and (b) example vector-field with an identified core region using a structured Cartesian grid system

Notably, this method can apply to flow-field data of both structured and unstructured grids. The points immediately around each point of interest are evaluated to determine if all of the categories are present in such a way that the area contained between the identified vertices is a vortex (see Fig. 4b). This method, alone, does not explicitly identify a single point as the centre, but, by interpolating the vector-field, can do so through iteration until the area enclosed by the vertices is sufficiently small that it may be approximated as a point. This method is also capable of identifying multiple vortices while only generating some false positives in complex flow-fields, as noted by the authors.

Wong and Yip [40] present a method of locating the centre of a rotation in circulating and spiralling vector flow-fields by creating a logarithmic spiral to align with a given flow-field that could identify the pattern of the flow using

$$r = ae^{\theta \cot \alpha} \quad (2.9)$$

where r is the radius of a point on the spiral from its centre, a is the rate of growth of the

spiral and determines the direction of rotation, θ is the angle with respect to the x -axis in a polar coordinate system, and α is the angle of the radial line from the centre to the tangent of the spiral at position (r, θ) . Since Wong and Yip [40] also worked with cases of centre location at oblique viewing angles to the wind-field plane, they redefined α as ψ using an additional parameter, ρ , to hold the viewing angle such that only when the viewing angle is normal to the plane are the two parameters equivalent. Following this, the vectors are all rotated by $\pi - \psi$ to force them to point to the centre of the spiral. Thus, the centre of the rotation is identified as the point with the most intersections, n_c , of the area spanning $\Psi + \Psi^+$ from each of the rotated vector tips. If the viewing angle is normal to the plane, $\Psi = 0$. The sector expansion angle, Ψ^+ , is defined by the user to increase the chance of the true centre being found in distorted or partial datasets. For the cases where the viewing angle is oblique, this location is identified by the greatest overlap of the region that extends at an angle $\psi_{max} - \psi_{min}$ from the tip of the rotated vectors. The authors acknowledged that this method requires α and ρ to be known *a priori* and that the general region of the centre needs to be identified first in order to avoid errors (e.g., in cases of multiple vortices in proximity). Thus, the algorithm's utility for the automation of the centre identification and tracking process is greatly reduced.

Although each of the aforementioned methods in this section have relevant applications in tornado modelling and research, they are unable to precisely identify the centre of a tornado while meeting the following criteria:

- a) Output a single point on a data-grid plane as the centre location,
- b) Operate in a computationally efficient manner, and
- c) Require minimal user-input or *a priori* information in order to function.

To relate key characteristics of tornadoes to the radius from the vortex centre and precisely track translation during their lifespans—even when there is not just a single, well-defined, axisymmetric vortex—requires the introduction of a novel method, which is the objective

of the present work.

2.1.3 Tornado Centre Identification

In this chapter, the data used were captured from a large-scale supercell simulation performed on the National Centre for Supercomputing Applications (NCSA) Blue Waters supercomputer using a modified version of the Bryan Cloud Model, version 1 (CM1) model [45, 46]. CM1 is a three-dimensional, nonhydrostatic, fully compressible cloud model designed for idealized studies of atmospheric phenomena such as thunderstorms. CM1 contains prognostic variables for wind, potential temperature, pressure, turbulence kinetic energy, cloud water, cloud ice, rain, snow, and hail/graupel. The model has been tuned to run efficiently on modern massively parallel supercomputer architectures and has produced some of the highest resolution thunderstorm simulations conducted to date (e.g., [16]). The tornado used in the development of the present method was produced in such a simulation. This generated a large amount of data points and timesteps necessitating the use of a centre-tracking algorithm for any type of analysis, as outlined in the previous section. From 25–27 April 2011, central and south-eastern U.S.A. experienced one of the largest tornado outbreaks ever recorded, with 348 tornado-related deaths and over \$10 billion of damage [4]. The simulation analyzed in this work was executed within 27 April 2011 mid-afternoon environmental conditions upwind of the day’s outbreak where a record 216 tornadoes were observed. The tornado from the simulation that is utilized in the present work appears to be representative of one of the 30 tornadoes rated EF 3 and EF 4 that occurred during the real-life event [47, 48], with peak tangential wind velocities relative to the domain of approximately $75 \text{ m}\cdot\text{s}^{-1}$ and a core diameter of 500 m. 1300 seconds of three-dimensional velocity data at 30 m grid resolution and single second timesteps, spanning much of the tornado’s life, were analyzed with the vortex tracking code described in this chapter. Finley *et al.* [49] presented preliminary results from a simulation in this same environment where a violent long-path tornado formed. As is the case with all of

the CM1 simulations described, the tornado formed naturally within the three-dimensional environment, unconstrained by artificial symmetries or external forcing as in TVC simulations. The tornado was freely able to move and tilt within the domain of 160 km in each horizontal dimension and 20 km vertically. However, a constant horizontal velocity vector ($\mathbf{u}_m = \langle 15.2, 10.5 \rangle [\text{m} \cdot \text{s}^{-1}]$) was subtracted from the velocity data to account for this free motion. Thus, a smaller, sample sub-domain of approximately 3.3-by-5.7 km horizontally and 330 m vertically was extracted from within the simulation domain, effectively capturing the tornado by moving with it through the storm. This sample domain is the only volume of the simulation used in the analysis performed in this study. It became apparent that the other methods of vortex centre identification, used previously in tornado model work and discussed above, are insufficient if attempting to analyze these data using a coordinate system defined with the tornado centre as the origin. This study presents a novel programmatic method of vortex identification that is relevant to the field of tornado vortex simulation and greatly improves the precision of both centre tracking and the subsequent data analyses taken with respect to that centre.

2.2 Methodology Details

When analyzing wind-field data from a tornado, or any given vortex, it is helpful to know the relative position of a point of interest with respect to the centre of the rotation and to identify that centre in a consistent way to track its motion in space and time. Details of the unpacking of the tornado simulation wind-field data and the assumptions and method involved in tracking the centre of the vortex are given in the following section and concisely summarised by the series of equations found in Appendix A.

2.2.1 Data Processing

The tornado wind-field data from the numerical simulation, based on an isotropic 30 m mesh, are organized in Cartesian coordinates and, thus, to best analyze them with respect to the centre of the vortex it is necessary to convert them into cylindrical coordinates with their origin at the centre and base of the tornado. Each file contains an array for each of the velocity components in the x , y , and z directions as u_x , u_y , and u_z , respectively. These velocities need to be converted to tangential, radial, and vertical velocity components u_t , u_r , and u_z , respectively, with respect to the vortex centre (O), as shown in Fig. 2.5.

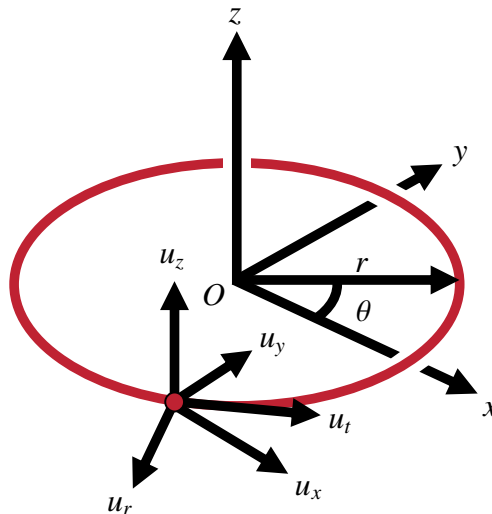


Figure 2.5: Cylindrical coordinate system conversion schematic

The cylindrical coordinate system components are defined as r for the radius from O , θ for the angle with respect to the x -axis of the Cartesian coordinate, and z for the vertical axis (the same as in the Cartesian coordinates). This tornado is fully three-dimensional as opposed to axisymmetric; hence, before locating the centre of the vortex, it is necessary to describe how that centre should be defined. In this study, the tornado centre is defined in the region where the gradient of u is a local minimum and is surrounded by a significant number of vectors displaying large curl in the horizontal plane and, ultimately, where u_x and $u_y = 0 \text{ m}\cdot\text{s}^{-1}$ [21, 40]. The analysis begins, therefore, by considering only one horizontal

slice of data at a time so that the analyses are in two-dimensions. The results of each individual analysis do not affect any subsequent analyses and therefore can be solved for either sequentially or concurrently. The velocity vector curl is simply the vorticity, ω , and is determined using Eq. 2.2 for a two-dimensional plane. The velocity vectors of interest are those located near where ω is a local maximum. There may be cases where multiple equally well-defined tornadoes appear in these supercell simulations, as well as in nature [50]. However, in the present work there is clearly a single dominant tornado vortex that encounters partial and minor vortices in the simulation. A schematic example of the wind-field is shown in Fig. 2.6a before any coordinate conversion has been performed and with vector arrows representing \mathbf{u} .

The number of local maxima of $\nabla \times \mathbf{u}$ identified is determined by

$$n_s = \left\lfloor \frac{\min \{n_x, n_y\}}{c} \right\rfloor \quad (2.10)$$

where n is the scaling-factor rounded to the nearest integer based on the size of the dataset, n_x is the number of points in x , n_y is the number of points in y , and c is the scaling parameter that is determined through a trial-and-error approach. The \lfloor and \rfloor brackets are used together here to indicate that the fractional components of values are rounded, down if less than 0.5 or up if 0.5 or greater, to the nearest integer, respectively. Equation 2.10 is used to ensure that, for a given dataset size and resolution, the number of points used for vortex detection is not so few that the search results are inconclusive and not so many that the points identified begin to include those that are not part of a well-defined vortex. For this study, n_x is 190, n_y is 111, and c is set at a value of 6 (see Appendix B for comparison of the impact of c values on the results). Therefore, $n_s = 19$ and the largest n_s values of $\nabla \times \mathbf{u}$ are identified (schematically shown in Fig. 2.6b using $n_s = 5$, as an example). Following this selection, the spatial averages (indicated by \langle and \rangle brackets) of the x and y positions of the maximum curl locations, x_c and y_c , and their standard deviations, σ_x and σ_y , are computed. Note that

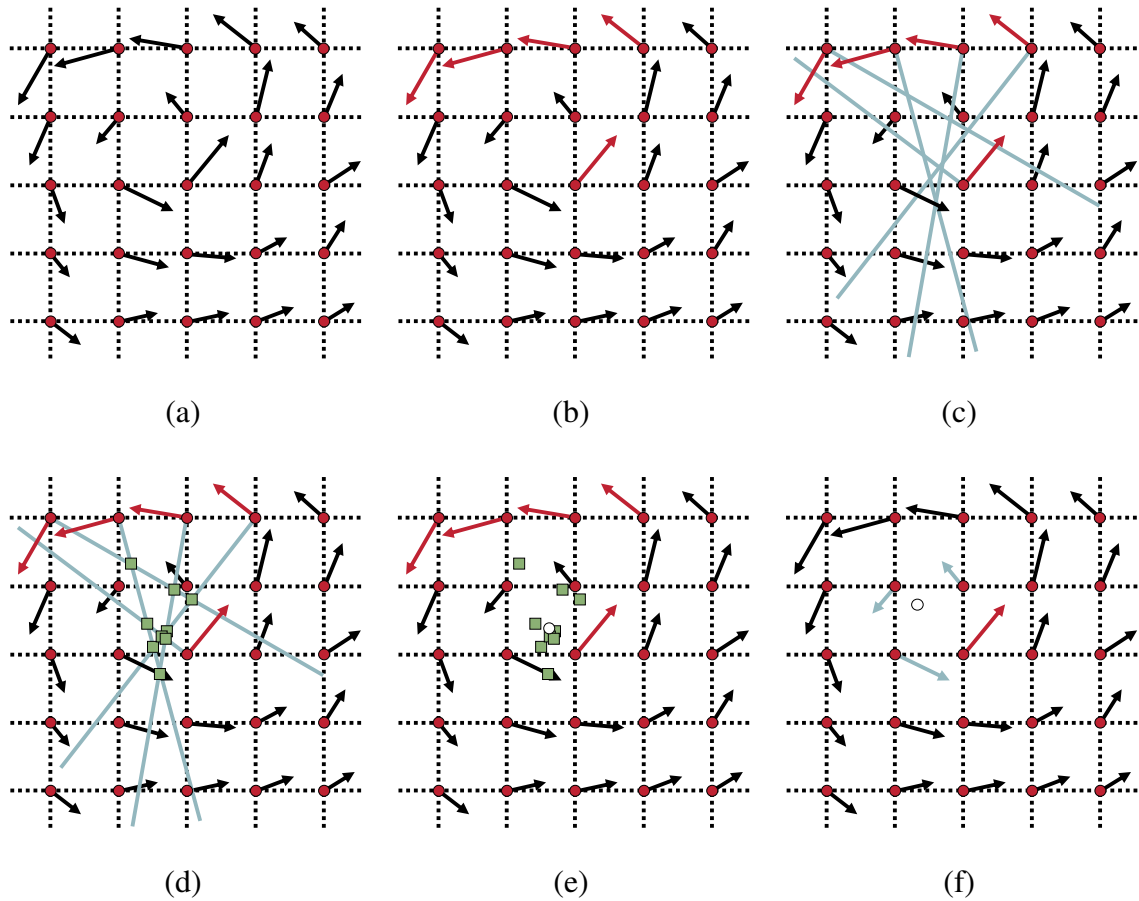


Figure 2.6: Finding the centre of an asymmetric vortex system using artificial data for illustrative purposes as an example where $n_s = 5$. (a) Schematic example of tornado dataset with vectors (shown as black arrows) on an isotropic grid (shown as dashed lines), (b) 5 vectors (shown in red) selected based on n_s , (c) lines perpendicular to the selected vectors' orientation drawn (shown in blue), (d) identified intersections of each line drawn (shown as green squares), (e) location of average intersection identified (shown as white circle), and (f) nearest vector identified (shown in red) and nearest vectors from identified vector that complete a loop (shown in blue) then used to interpolate for the location of zero-velocity (shown as white circle)

σ_x and σ_y are always rounded up since x_c and y_c are indexed positions, not interpolated. By rounding up, this method provides a more conservative approach to the number of points eliminated from the search within each standard deviation. Using a desired number of standard deviations, ϕ , the next step is to eliminate all points from the centre search that fall outside of the area of the ellipse centred on $[\langle x_c \rangle, \langle y_c \rangle]$ of lengths $2\phi^{1/2}\sigma_x$ and $2\phi^{1/2}\sigma_y$

using

$$\frac{(x_{c,i} - \langle x_c \rangle)^2}{\sigma_x^2} + \frac{(y_{c,i} - \langle y_c \rangle)^2}{\sigma_y^2} \leq \phi. \quad (2.11)$$

It should be noted that, if multiple vortices are present in a given dataset, an additional step should be inserted here to weight the filtering of selected points by location relative to other identified maximum curl positions. The analysis would then proceed for each identified region regardless of how many vortices are present. The remaining number of points, $N = 1, 2, \dots$, are refined further using a technique developed from the methodology used by Wong and Yip [40] to find the centre of rotating fields at any given angle of observation to the plane of rotation. Their technique is not applied directly here because, as mentioned in Sect. 2.1.2, it requires knowledge of the location of the vortex region within the domain before applying the analysis technique and it is designed for axisymmetric-dominant systems. In the present study, the data are often highly asymmetric during the tornado's lifetime. This includes the presence of a secondary, smaller vortex close to the main vortex that could skew the results considerably if Wong and Yip's [40] method were to be applied directly (see Sect. 2.3). Thus, the principle of using the overlapping of all the regions of confidence extending from the rotated velocity vector tips to identify the centre has been adapted so that lines perpendicular to the velocity vector directions are drawn at each of the n_s locations of x_c and y_c , minus those that did not satisfy Eq. 2.11. This is achieved by determining the equation of a line perpendicular to the identified velocity vectors (see Fig. 2.6c). The intersections of these lines are identified by setting the x and y in the equation of a given line equal to the x and y of another (Fig. 2.6d), which results in

$$\begin{aligned} x_{\text{int}} &= \frac{b_j - b_i}{m_i - m_j} \\ y_{\text{int}} &= \frac{m_j b_i - m_i b_j}{m_j - m_i} \end{aligned} \quad (2.12)$$

where x_{int} and y_{int} are the x and y positions of the line intersections, respectively, b is the y -intercept of the lines with the domain ordinate, m is the slope of the lines, and i refers

to the first line selected and varies from 1 to $N - 1$ in an incremental loop to be compared with line j , which varies from $i + 1$ to N in an incremental loop contained within i to avoid comparing the same intersection with itself or double counting intersections.

A similar averaging technique to that applied to the maximum vorticity locations is also used here for the intersections. The standard deviation and point elimination techniques above are applied, with the addition that any intersection outside of the domain is ignored before averaging (see Fig. 2.6e). Then, the position of this final averaged point of intersections is checked for an indication that either it does not fall within the selection region or the location is so close to the domain edge that the program will attempt to search outside of it in the subsequent centre searching process. In the case of a null error, the location found will be replaced with the location of maximum z -direction vorticity in the wind-field or the minimum pressure that are both able to approximately, but not exactly, identify a centre.

The average, although very useful in narrowing the area of search, is not used directly to find the centre position as it is less accurate for the times in the tornado data where the shape of the vortex is highly asymmetric. Instead, the point in the data nearest to this point is selected (see Fig. 2.6f) and a c -by- c grid is created with this nearest point at the centre and the points immediately surrounding it comprising the rest of the grid. This is done under the assumption that the tornado centre will be located at the position of zero horizontal, ground-relative velocity that will likely fall somewhere in between the discrete data points. Thus, within this reduced grid, the most helpful location to begin with is at the grid location of minimum velocity. This new grid is limited to size c -by- c to keep the search within the identified vortex core and not detecting other vortices that also have a local velocity minimum, even if it is lower than that within the main vortex. In finding multiple vortices, this technique can be used on each individual vortex to find their centres rather than identifying their general region. If the previously identified point is not the

minimum, then whichever point is the actual minimum velocity is defined as the centre of a three-by-three grid of the velocities of the points immediately surrounding it.

Of the remaining nine points, there are three vortex region cases checked: rotation within one of the four quadrants of the grid; rotation within the left, right, top, or bottom of the grid; or rotation about the entire grid situated about the point in the centre (see Fig. 2.7).

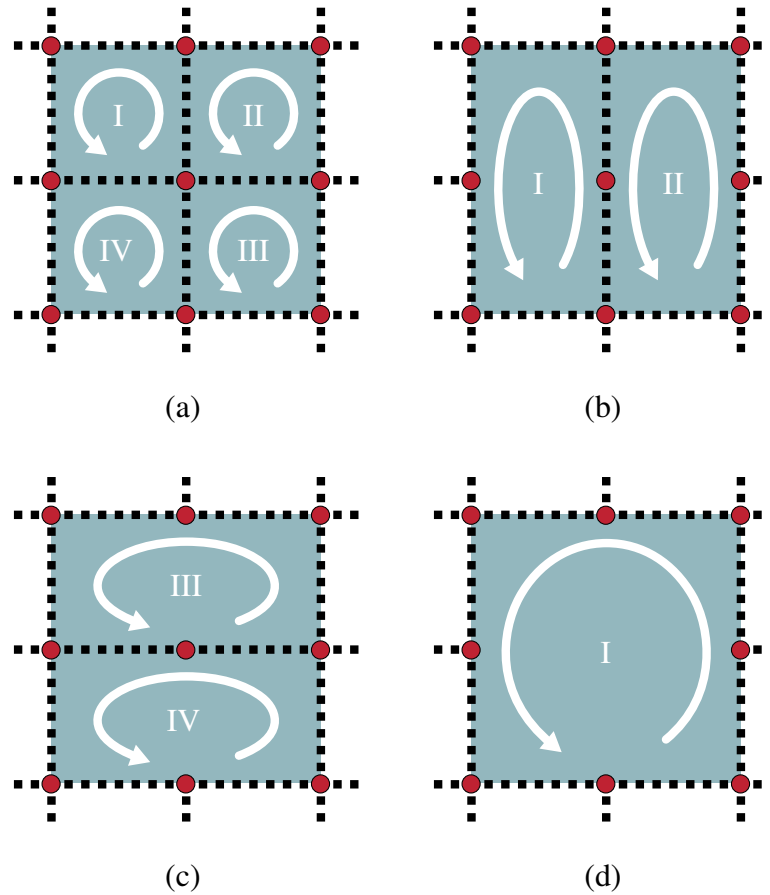


Figure 2.7: Schematic view of vortex region case checking where the red circles indicate the data points. Complete rotation loop in (a) one of the four quadrants, (b) left or right halves, (c) top or bottom halves, and (d) the entire area

A complete loop is identified based on the sum of the vector signs comprising the loop adding to zero for both x and y directions. This is similar to the technique described in [39], although here it is able to be expanded to incorporate any desired number of points into the loop for different vortex shapes. The number of successfully identified possible loops are stored and the sum of the tangential velocity magnitudes of each vector around each path

is calculated so that, for two similar paths, the one having the smallest cumulative velocity around its loop is considered to contain the centre of the vortex.

This method can be implemented iteratively, if the smaller grid size is still large, to narrow down a vortex region for larger tornadoes or for higher spatial resolution wind-field data where the search array may include more than c^2 vectors. If no successful path is identified, the search is repeated and skips the previously identified minimum velocity vector up to a total of c times. If this still fails to identify a path, then the point that would be substituted for the final averaged intersections in the case of error, as described above, is defaulted to as the designated tornado centre.

The four corners of the loop found above are bilinearly interpolated for the position where $u_x = 0$ and $u_y = 0$, unless no path is found in which case this interpolation step (see Fig. A.1) is omitted.

Therefore, the searching portion of the algorithm is concluded, as seen in Fig. 2.6f, and it would be trivial to now analyze any given tornado with its centre as the origin of a cylindrical coordinate domain and make use of vortex-relative radial, tangential, and vertical velocities.

2.3 Results and Discussion

The results of the methods described above are detailed in the following section, including a discussion of the impact of the findings in contrast to the methods used by others described in Sect. 2.1.2.

2.3.1 Results

The programmatic methods described above were applied to the simulated tornado-producing supercell dataset as mentioned in Sect. 2.1.3. The fully tracked tornado centre may be found

below in Fig. 2.8 for both the simulation-domain-relative tracking and the ground-relative tracking. The ground-relative tracking was created by multiplying the removed velocity vector, u_m , by time since the start of the dataset ($t = 5000$ s), t_1 , and adding this distance to the given point associated with each timestep, respectively.

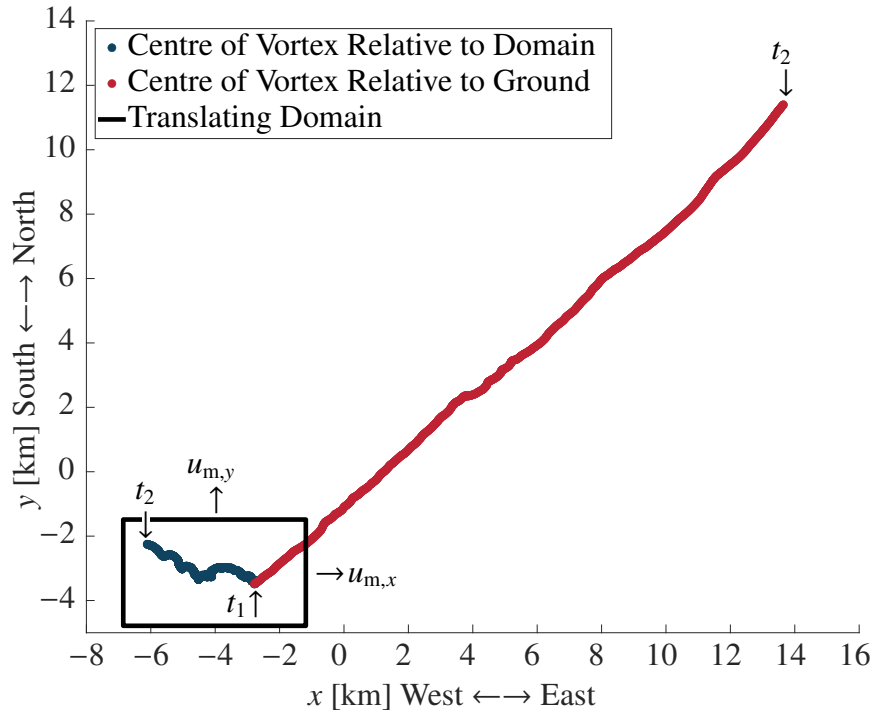


Figure 2.8: Plan view of the tornado following the centre at $z = 15$ m a.g.l. throughout the entire life cycle of the vortex from $t_1 = 5000$ s to $t_2 = 6300$ s. The motion of the vortex centre is shown relative to the dataset domain boundaries (moving at $(u_{m,x}, u_{m,y}) = (10.5, 15.2)$ m·s⁻¹) and relative to the ground. Note that

For the purpose of testing that this method functions as intended, each timestep involved an independent search of the velocity-field. To minimize computation time, it would be prudent to reduce the algorithm's search region after the first timestep is analyzed successfully and base each subsequent search of the region off of the previous centre position. This is because the tornado will only be able to move a limited distance per timestep, depending on the temporal resolution and tornado translation velocity. This would also reduce the potential for errors in identifying the centre position introduced by such a large scope of centre search repeated for every timestep.

It was apparent that the path of the vortex could be spatially and temporally defined with a high degree of accuracy, including near to the ground, which is useful in understanding the potential wind-loading on infrastructure and buildings with respect to the vortex centre. From the entirety of the 3.3-by-5.7 km horizontal, 330-m-high sample domain (11 horizontal slices at 30 m spacing), the algorithm failed to interpolate for, or correctly identify, a centre position 1 time out of 1300 CM1 model timesteps when analyzed independently of each other, equating to a 0.08% error rate using $c = 6$. The timesteps where the algorithm needed to reattempt (see Sect. 2.2.1) identifying the centre occurred during peak u_t in the vortex, approximately at the midpoint of the lifespan of the tornado, which is also when it began to combine with a weaker vortex.

2.3.2 Comparisons of Methods

Using the full-size of the dataset domain for several arbitrarily chosen but representative timesteps and heights a.g.l., Table 2.2 shows the time required to execute the searching algorithms for each of the methods detailed in Sect. 2.1.2 compared to the method proposed in this chapter.

Table 2.2: Comparison of the time taken to analyze a given horizontal plane of the tornado by previously developed vortex tracking methods with the proposed method

Analysis Method	Analysis Runtime per Horizontal Plane (ms)	Analysis Runtime per Horizontal Plane (Normalized by the Proposed Method Runtime)
Levy et al. (1990)	8.60	7.61
Jeong and Hussain (1995)	0.52	0.46
Sujudi and Haimes (1995)	8394.48	7428.74
Jiang et al. (2002)	10786.20	9545.31
Wong and Yip (2009)	202.55	179.25
Proposed Method	1.13	1.00

The fastest method is that of Jeong and Hussain [37], with an average solution time of

just 0.52 ms, followed by the proposed method in this chapter and the Levy *et al.* [36] method. Much slower are the methods proposed by Wong and Yip [40], using the overlap of the spans projecting from each vector tip, by Sujudi and Haines [38], using the reduced velocity, and by Jiang *et al.* [39], using the vector directions. The result of implementing each of these methods as intended (without modification) can be seen in Fig. 2.9 on a horizontal view of data, sampled from the simulation described previously.

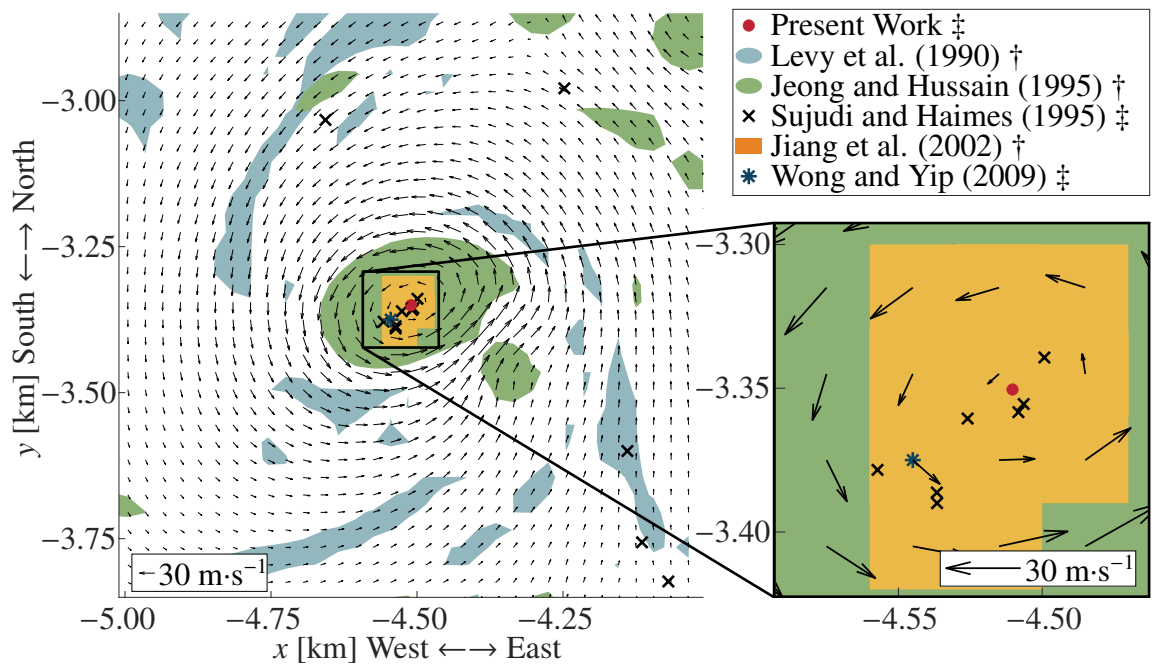


Figure 2.9: Comparison of the accuracy of various methods in tracking the vortex core centre on a representative wind-field data sample at $t = 5687$ s and $z = 165$ m a.g.l. The † in the figure legend represents methods that identify a region and ‡ represents those that identify point locations

Using the Levy *et al.* [36] method, the main tornado vortex appeared to be better described by where $\hat{H} \neq 0$ (not shown in Fig. 2.9) for these data. The regions where $|\hat{H}| \neq 1$ were assumed to be those where the angle between \mathbf{u} and $\boldsymbol{\omega}$ was less than or equal to 15° . In Fig. 2.9, these regions seem to outline a vortex presence but do not provide a definite location of a tornado centre. Even though, as described in [36], the largest ω_z was consistently within the vortex region indicating that $\boldsymbol{\omega}$ is vertical, u_z was often minuscule relative to the horizontal components of \mathbf{u} such that the two vectors were not close to parallel. The sense

of u_z was also not often uniform across the vortex such that the sign of \hat{H} could not be relied upon to identify the vortex rotation direction. Additionally, to accommodate the use of the gradient operator, it was necessary to run the program for all heights in the vortex at the single timestep because, otherwise, there would be no meaningful output. However, this only contributed to a mild increase in computational time.

Jeong and Hussain's [37] method very effectively identifies the main vortex and (when present) a smaller, but still substantial, vortex (Fig. 2.9). However, it is clear that further analysis would be required to identify the centre of the tornado since its position is not given simply by $\lambda_2 < 0$ in this case.

The method of Sujudi and Haines [38] is conceptually similar to the Jeong and Hussain [37] method. However, in [38], the grid of data is divided into tetrahedrons meaning six cells between every cube of eight nodes (for Cartesian coordinates) and, consequently, that two-dimensional analysis is not possible. To accommodate this, the horizontal layers above and below the layer of interest needed to be analyzed. This leads to a dramatic increase in the computation time as each cell must be created, divided, and analyzed. The advantage of this method is that it does very accurately pinpoint the location of vortices but, without filtering, does not leave one definite point (Fig. 2.9).

The method of Jiang *et al.* [39], although the slowest of all the demonstrated methods, is able to capture the main vortex (Fig. 2.9). The region is a regular geometric shape because the area defined is just the region shown to capture each of the direction ranges, so it is only a binary indicator. Only the nearest neighbours to each given point of interest are analyzed and in this comparison the search strategy in their methodology is not implemented where the data are iterated further to group smaller vortices together into larger ones. Additionally, in this comparison each vortex identified is not interpolated and re-analyzed to identify a centre location more precisely. These steps would have required even more time to solve and so, for the purposes of this comparison, are omitted.

The Wong and Yip [40] method is successful in identifying a point that is within the vortex where n_c is a maximum but this point is not the actual tornado centre (Fig. 2.9). The values of $\alpha = \pi/2$ and $\Psi^+ = \pi/4$ are used, as given by Wong and Yip [40] for tornado-like vortices. For the calculation of n_c , only those points that are up to 20 points away are considered, which was determined by Wong and Yip [40], through trial-and-error, to yield valid results. Using $\alpha = \pi/2$ means that the spiral is a circle, which does fit with the vector directions around the main vortex for the most part. To be able to use this method properly, the region of the main vortex would have to be identified *a priori* and only those vectors within this region would be a part of the span overlap analysis. Instead, the entire domain was used for the search and so the spiral component of the method was not useful as this would defeat the purpose of an automatic searching algorithm. Although this method provides a desirable output of just a single point, for a complex and dynamic tornado system, whose centre moves within the domain, it would be useful to combine this methodology with another. For example, identifying an area of maximum vertical vorticity, such as in [34], would narrow down the interrogation region without user-intervention.

Through the method proposed in this chapter, a centre point was clearly identified (Fig. 2.9). This is computed using $c = 6$ and the analysis ran without error and appears to be in the correct location qualitatively as well as being the point matching the criteria for a tornado centre laid out in Sect. 2.2.1. Although this only captures the main vortex and not minor ones, it could (with some effort) be expanded to function with multiple vortices if, for example, the curl locations used to begin the analysis were grouped by nearest neighbours to prevent searching between two different vortices.

Using the coordinate transformed data, it is possible to average the tangential velocity around each circumference and identify that the data in Fig. 2.9 yield a vortex radius (taken as the circumference of maximum average tangential velocity) of approximately 130 m from the identified centre. By normalizing the distance from the centre identified by the

proposed method to the other point identifying methods, it is possible to compare the accuracy of each. Levy *et al.* [36], Jeong and Hussain [37], and Jiang *et al.* [39] all identify vortex structures in a region so they cannot be compared in this manner. However, it is clear that the latter two of these three methods manage to successfully capture the vortex centre point. The Levy *et al.* [36] method, however, struggled to provide any region of interest with the given data. Sujudi and Haimes [38] identifies a point as near as 5 m from the centre found with the proposed method but as far away as 2 km, which, when normalized, represents 3.73% and 1630% of the radius of the core, respectively. Finally, Wong and Yip [40] identifies a single point 45 m from the centre (or 34.6% when normalized) even after modifying the methodology to suit the dataset better.

2.4 Conclusions and Recommendations

A method of identifying the precise location of a tornado's main vortex centre has been developed that allows for superior tracking in comparison to previous work in tornado research, which make assumptions such as the centre being a fixed location, place the vortex *a priori*, or require user intervention before confirming the centre location. The presented centre-searching method quickly finds solely one centre location for each timestep and horizontal slice of the domain. Previous vortex identification methods have been demonstrated to be deficient in comparison to the presently described method, as they are only able to highlight the region of the vortex, find several centre positions that then require post-processing, or offer an approximate centre location. The benefit of the proposed method is that, having precisely identified the centre of the tornado, one may complete additional analyses on their data to examine the velocity profiles within the vortex, simulate the damage potential relative to the distance from the tornado centre, and track a tornado path throughout its life cycle for both real and simulated vortices. In future work, the scope of the centre searching algorithm may be enhanced by implementing the ability

to identify smaller vortices, that may encroach on the main one, or even identify a centre in cases where there are multiple significant vortices that are not clearly stronger than one other.

References

- [1] J. S. Grams, R. L. Thompson, D. V. Snively, J. A. Prentice, G. M. Hodges, and L. J. Reames, “A climatology and comparison of parameters for significant tornado events in the United States,” *Weather and Forecasting*, vol. 27, no. 1, pp. 106–123, 2012.
- [2] W. S. Lewellen, *Tornado Vortex Theory*. American Geophysical Union (AGU), 1993, pp. 19–39.
- [3] National Centers for Environmental Information (NCEI), “Storm events database,” National Oceanic and Atmospheric Administration (NOAA), July 2023. Accessed: May 20, 2023. [Online.] Available: <https://www.ncdc.noaa.gov/stormevents/>
- [4] National Centers for Environmental Information (NCEI), “U.S. billion-dollar weather and climate disasters,” National Oceanic and Atmospheric Administration (NOAA), July 2023. Accessed: May 20, 2023. [Online.] Available: <https://www.ncei.noaa.gov/access/billions/>
- [5] C. A. Doswell, A. R. Moller, and H. E. Brooks, “Storm spotting and public awareness since the first tornado forecasts of 1948,” *Weather and Forecasting*, vol. 14, no. 4, pp. 544–557, 1999.
- [6] H. E. Brooks and J. Correia, “Long-term performance metrics for National Weather Service tornado warnings,” *Weather and Forecasting*, vol. 33, no. 6, pp. 1501–1511, 2018.
- [7] E. Agee and L. Taylor, “Historical analysis of U.S. tornado fatalities (1808–2017): Population, science, and technology,” *Weather, Climate, and Society*, vol. 11, no. 2, pp. 355–368, 2019.
- [8] J. R. Lim, B. F. Liu, and M. Egnoto, “Cry wolf effect? evaluating the impact of

- false alarms on public responses to tornado alerts in the southeastern United States,” *Weather, Climate, and Society*, vol. 11, no. 3, pp. 549–563, 2019.
- [9] H. L. Kuo, “Axisymmetric flows in the boundary layer of a maintained vortex,” *Journal of Atmospheric Sciences*, vol. 28, no. 1, pp. 20–41, 1971.
- [10] Y.-K. Wen, “Dynamic tornadic wind loads on tall buildings,” *ASCE Journal of the Structural Division*, vol. 101, no. 1, pp. 169–185, 1975.
- [11] N. B. Ward, “The exploration of certain features of tornado dynamics using a laboratory model,” *Journal of Atmospheric Sciences*, vol. 29, no. 6, pp. 1194–1204, 1972.
- [12] C. R. Church, J. T. Snow, G. L. Baker, and E. M. Agee, “Characteristics of tornado-like vortices as a function of swirl ratio: A laboratory investigation,” *Journal of Atmospheric Sciences*, vol. 36, no. 9, pp. 1755–1776, 1979.
- [13] M. Refan and H. Hangan, “Characterization of tornado-like flow fields in a new model scale wind testing chamber,” *Journal of Wind Engineering and Industrial Aerodynamics*, vol. 151, pp. 107–121, 2016.
- [14] Z. Liu, C. Zhang, and T. Ishihara, “Numerical study of the wind loads on a cooling tower by a stationary tornado-like vortex through LES,” *Journal of Fluids and Structures*, vol. 81, pp. 656–672, 2018.
- [15] D. Natarajan, “Numerical simulation of tornado-like vortices,” Ph.D. dissertation, Univ. Western Ontario, London, ON, Canada, 2011.
- [16] L. Orf, “A violently tornadic supercell thunderstorm simulation spanning a quarter-trillion grid volumes: Computational challenges, I/O framework, and visualizations of tornadogenesis,” *Atmosphere*, vol. 10, no. 10, p. 578, 2019.

- [17] C. Baker and M. Sterling, “Modelling wind fields and debris flight in tornadoes,” *Journal of Wind Engineering and Industrial Aerodynamics*, vol. 168, pp. 312–321, 2017.
- [18] E. Savory, G. A. Parke, M. Zeinoddini, N. Toy, and P. Disney, “Modelling of tornado and microburst-induced wind loading and failure of a lattice transmission tower,” *Engineering Structures*, vol. 23, no. 4, pp. 365–375, 2001.
- [19] A. Shehata, A. El Damatty, and E. Savory, “Finite element modeling of transmission line under downburst wind loading,” *Finite Elements in Analysis and Design*, vol. 42, no. 1, pp. 71–89, 2005.
- [20] M. Refan, H. Hangan, J. Wurman, and K. Kosiba, “Doppler radar-derived wind field of five tornado events with application to engineering simulations,” *Engineering Structures*, vol. 148, pp. 509–521, 2017.
- [21] W. Rankine, *Motions of fluids—hydrodynamics*. Charles Griffin and Company, London, 1877, pp. 574–577.
- [22] Z. Tang, C. Feng, L. Wu, D. Zuo, and D. L. James, “Characteristics of tornado-like vortices simulated in a large-scale ward-type simulator,” *Boundary-Layer Meteorology*, vol. 166, pp. 327–350, 2018.
- [23] R. Davies-Jones, “Can a descending rain curtain in a supercell instigate tornadogenesis barotropically?” *Journal of the Atmospheric Sciences*, vol. 65, no. 8, pp. 2469–2497, 2008.
- [24] A. Altalmas and A. El Damatty, “Finite element modelling of self-supported transmission lines under tornado loading,” *Wind & structures*, vol. 18, no. 5, pp. 473–495, 2014.

- [25] J. Wang, S. Cao, W. Pang, and J. Cao, “Experimental study on effects of ground roughness on flow characteristics of tornado-like vortices,” *Boundary-Layer Meteorology*, vol. 162, pp. 319–339, 2017.
- [26] A. Razavi and P. P. Sarkar, “Laboratory study of topographic effects on the near-surface tornado flow field,” *Boundary-layer meteorology*, vol. 168, pp. 189–212, 2018.
- [27] A. Hamada and A. El Damatty, “Behaviour of guyed transmission line structures under tornado wind loading,” *Computers & Structures*, vol. 89, no. 11, pp. 986–1003, 2011, computational Fluid and Solid Mechanics 2011.
- [28] T. G. Pecin, A. A. D. Almeida, and J. L. Roehl, “Tornadic mechanical global actions on transmission towers,” *Journal of the Brazilian Society of Mechanical Sciences and Engineering*, vol. 33, no. 2, pp. 131—138, Apr 2011.
- [29] V. Beck and N. Dotzek, “Reconstruction of near-surface tornado wind fields from forest damage,” *Journal of Applied Meteorology and Climatology*, vol. 49, no. 7, pp. 1517–1537, 2010.
- [30] M. Refan, “Physical simulation of tornado-like vortices,” Ph.D. dissertation, Univ. Western Ontario, London, ON, Canada, 2014.
- [31] C. A. Wan and C. C. Chang, “Measurement of the velocity field in a simulated tornado-like vortex using a three-dimensional velocity probe,” *Journal of Atmospheric Sciences*, vol. 29, no. 1, pp. 116–127, 1972.
- [32] V. T. Wood and R. A. Brown, “Effects of radar proximity on single-Doppler velocity signatures of axisymmetric rotation and divergence,” *Monthly Weather Review*, vol. 120, no. 12, pp. 2798–2807, 1992.

- [33] R. C. Strawn, D. N. Kenwright, and J. Ahmad, “Computer visualization of vortex wake systems,” *AIAA Journal*, vol. 37, no. 4, pp. 511–512, 1999.
- [34] C. K. Potvin, “A variational method for detecting and characterizing convective vortices in cartesian wind fields,” *Monthly Weather Review*, vol. 141, no. 9, pp. 3102–3115, 2013.
- [35] Y. Aboelkassem, G. H. Vatistas, and N. Esmail, “Viscous dissipation of Rankine vortex profile in zero meridional flow,” *Acta Mechanica Sinica*, vol. 21, pp. 550–556, 2005.
- [36] Y. Levy, D. Degani, and A. Seginer, “Graphical visualization of vortical flows by means of helicity,” *AIAA Journal*, vol. 28, no. 8, pp. 1347–1352, 1990.
- [37] J. Jeong and F. Hussain, “On the identification of a vortex,” *Journal of Fluid Mechanics*, vol. 285, pp. 69—94, 1995.
- [38] D. Sujudi and R. Haimes, “Identification of swirling flow in 3-D vector fields,” in *Proceedings of 12th Computational Fluid Dynamics Conference*, 1995, p. 1715.
- [39] M. Jiang, R. Machiraju, and D. S. Thompson, “A novel approach to vortex core region detection,” in *Proceedings of VisSym’02*, vol. 2, 2002, pp. 217–225.
- [40] K. Y. Wong and C. L. Yip, “Identifying centers of circulating and spiraling vector field patterns and its applications,” *Pattern Recognition*, vol. 42, no. 7, pp. 1371–1387, 2009.
- [41] Q. Chen, Q. Zhong, M. Qi, and X. Wang, “Comparison of vortex identification criteria for planar velocity fields in wall turbulence,” *Physics of Fluids*, vol. 27, no. 8, pp. 085–101, 08 2015.
- [42] M. Jiang, R. Machiraju, and D. Thompson, *Detection and visualization of vortices*. Cambridge, MA, U.S.A.: Elsevier Academic Press, 2011, vol. 295, pp. 295–310.

- [43] L. G. Orf, B. D. Semeraro, and R. B. Wilhelmson, “Vortex detection in a simulated supercell thunderstorm,” *Atmospheric Science Letters*, vol. 8, no. 1, pp. 29–35, 2007.
- [44] K. H. Rosen, *Handbook of discrete and combinatorial mathematics*. Boston, MA, U.S.A.: CRC Press, 1999.
- [45] G. H. Bryan and J. M. Fritsch, “A benchmark simulation for moist nonhydrostatic numerical models,” *Monthly Weather Review*, vol. 130, no. 12, pp. 2917–2928, 2002.
- [46] G. H. Bryan, “Cloud Model 1 (cm1) homepage,” National Center for Atmospheric Research (NCAR); National Science Foundation (NSF), 2008. Accessed: 2023-04-04. [Online.] Available: <https://www2.mmm.ucar.edu/people/bryan/cm1/>
- [47] A. Curtis and J. W. Mills, “Spatial video data collection in a post-disaster landscape: The Tuscaloosa Tornado of April 27th 2011,” *Applied Geography*, vol. 32, no. 2, pp. 393–400, 2012.
- [48] C. D. Karstens, W. A. Gallus, B. D. Lee, and C. A. Finley, “Analysis of tornado-induced tree fall using aerial photography from the Joplin, Missouri, and Tuscaloosa–Birmingham, Alabama, tornadoes of 2011,” *Journal of Applied Meteorology and Climatology*, vol. 52, no. 5, pp. 1049–1068, 2013.
- [49] C. A. Finley, L. Orf, B. D. Lee, and R. B. Wilhelmson, “High-resolution simulation of a violent tornado in the 27 april 2011 outbreak environment,” in *29th Conference on Severe Local Storms, Stowe, VT*. American Meteorological Society, 2018.
- [50] L. Orf, R. Wilhelmson, and L. Wicker, “Visualization of a simulated long-track EF5 tornado embedded within a supercell thunderstorm,” *Parallel Computing*, vol. 55, pp. 28–34, 2016.

Chapter 3

3 Quantifying the Asymmetry in Tornado Vortex Wind-Fields Using Numerical Simulations of Supercell Thunderstorms

3.1 Introduction

The occurrence and impact of tornadoes have been increasing in many parts of the world. For example, in the U.S.A., there has been a statistically significant $0.66\% \pm 0.26\%$ annual rise in the average number of tornadoes detected per outbreak—from 10 in 1954 to 15 in 2014 [1]. The bulk of this increase is comprised of weaker EF scale 0 and 1 events [2, 3] and can, in part, be attributed to improvements in forecasting ability via public awareness [4], prevention of false-positive warnings, and increased warning lead-times [5]. As the average global temperature rises, it is expected that there will be an increase in favourable conditions for tornado formation, with higher classifications of vortex intensity occurring over a longer period of the year and in regions that have previously not experienced such events [6]. It is important to improve the accuracy of tornado models because, although most tornadoes fall below a damage rating of EF 2, damage costs have accelerated during the past decade [7], with the true costs underestimated by a factor of between 10 and 15% [8]. In the U.S.A alone, there have been approximately 2000–3000 tornado-related fatalities since the 1980s and 5000–7000 since the 1950s [3, 9]. The most powerful tornadoes contribute the most to these figures and are produced by supercell thunderstorm events [10]. Supercell thunderstorms are defined by a persistent rotating updraft known as a mesocyclone that results from the tilting of horizontal vorticity that is present in the storm's large-scale environment as well as generated below ~ 1 km by the storm itself. The low-level vorticity in what is known as the storm's cold pool is generated by horizontal

buoyancy gradients created by variations in hydrometeor loading and thermodynamic cooling from the evaporation, sublimation, and melting of hydrometeors. Both the leading edge of the cold pool as well as regions within the cold pool itself have been shown to serve as an important source of vorticity for both non-tornadic “seed” vortices that can grow to tornado strength, as well as horizontal streamwise vorticity that, when tilted vertically, helps to strengthen the storm’s mesocyclone near the ground, making conditions favourable for long-lived tornadoes [11, 12].

Tornado research focuses on their formation and life-cycle (from the meteorological perspective) and their ability to inflict damage on infrastructure (from the engineering perspective), with both disciplines attempting to model tornado vortices but with different intentions. In meteorology, studies focus on identifying which severe thunderstorms could be capable of producing tornadoes (e.g., [13–15]), the expected wind speed or damage potential from these storms (e.g., [16–18]), and how such information can be used to increase the warning lead time as well as the probability of detection (e.g., [5, 19, 20]). These meteorological computational studies are field-data driven and, as such, are capable of producing thunderstorms representative of those that occur in nature in terms of scale, intensity, and their ability to spawn similarly realistic tornadoes. For wind engineering analyses, understanding the wind-loading caused by a tornado can lead to better-designed infrastructure and greater protection of human life (e.g., [21–23]).

Although there is the potential to couple both disciplines, to the best of the authors’ knowledge, this has yet to be fully exploited. To do this involves applying meteorologically informed ICs and BCs to generate tornado-like vortex data with enough spatial and temporal resolution to be relevant in wind-loading analyses.

3.1.1 Vortex Models

There are many methods available to generate wind-field data representative of a tornado, most notably the analytical methods of Rankine [24], Burgers [25], Sullivan [26], Kuo [27]. Kuo's [27] method was simplified by Wen [28] and Wen and Ang [29] to be more readily used in engineering studies and, as such, the latter two are both preferred. In each model, even if the radial or vertical or both velocities were present, the tangential velocity was the dominant as these are supposed to model vortices (not always tornado vortices but they are all applicable). This tangential velocity will increase from the centre, $r = 0$, where $u_t = 0$ until the peak velocity (or core) radius, r_c , where it is a maximum and then decays as $r \rightarrow \infty$. The methods by which each model achieved this varies, but the characteristics of each u_t profile are more or less interchangeable. The equations that define each velocity profile, in the tangential direction, which are used in this study as a basis of comparison to the velocity data analysed in most wind-engineering studies, are subsequently given starting with Rankine [24],

$$u_{t,R} = \begin{cases} \frac{r \cdot u_t(r_c)}{r_c}, & r \leq r_c \\ \frac{r_c \cdot u_t(r_c)}{r}, & r > r_c \end{cases} . \quad (3.1)$$

The equation for u_t prescribed by Burgers [25] is,

$$u_{t,B} = \frac{\Gamma}{2\pi r} \left(1 - e^{-Cr^2/2\nu} \right) \quad (3.2)$$

where C is a constant of units speed over distance (i.e., $\text{m}\cdot\text{s}^{-1}$) and is an indication of the vortex strength, ν is the kinematic viscosity of the fluid (i.e., air^1) in m^2s^{-1} , and $\Gamma = 2\pi\omega \cdot r^2$ in m^2s^{-1} where ω is the angular velocity prescribed to force the vortex and $r \rightarrow \infty$. The equation for a two-celled vortex, which allows a more realistic downdraft near the centre

¹Leslie and Snow [30] found that the conventional, molecular value produced a core radius much smaller than the experimental TVC they tested, with the same parameters used in the vortex equation, and therefore they prescribed a value of $\nu = 7 \times 10^{-3} \text{m}^2\text{s}^{-1}$

axis, is given from Sullivan [26] as,

$$u_{t,S} = \frac{\Gamma}{2\pi r} \frac{H(\alpha r^2/2\nu)}{f(\infty)} \quad (3.3)$$

where the general function $f(r)$ is given by

$$f(r) = \int_0^r \exp\left(-\gamma + 3 \int_0^\delta \left[\frac{1 - e^{-\beta}}{\beta}\right] d\beta\right) d\delta \quad (3.4)$$

where β and δ are the integration variables. The second fraction term in Eq. 3.3, $f(Cr^2/2\nu)/f(\infty)$, approaches a value of 1 rapidly as $Cr^2/2\nu$ increases past a value of approximately 15 [30].

The profile of u_t given by Wen [28] and Wen and Ang [29] is computed using,

$$u_{t,W} = \begin{cases} u_{t,W}(\hat{z} > 1) \left[1 - e^{-\pi\hat{z}} \cos(2.4\pi\hat{z} \cdot e^{-0.8r^4})\right], & \hat{z} \leq 1 \\ 1.4 \frac{u_t(r_c)}{r} \left[1 - e^{-1.256r^2}\right], & \hat{z} > 1 \end{cases} \quad (3.5)$$

where \hat{z} is the ratio of height, z , to r_c and will be used herein as a physical basis to scale and compare heights across results from different tornado studies and datasets, including those used in the present study. None of the profiles discussed depend on time, t , nor azimuthal position, θ . Jischke and Parang [31] discussed a dependence on θ but neglected it immediately afterwards by averaging over the circumference. Wen [28] and Wen and Ang [29] depart from the other models by adding a dependence on height. The equations for Burgers [25] and Sullivan [26] produced a spiralling motion towards the centre but there was no coupling of the velocity between velocity components, resulting in vortices with a constant velocity distribution profile. However, the present authors could find no instance of an analytical model in the literature that considers the vertical tilt of a tornado-like vortex, which should be present from its translation, and the characteristics of the velocity component profiles in an asymmetric velocity field.

3.1.2 Tornado Vortex Chambers

Unlike analytical models, where the velocity profile was directly prescribed, the tornado-like vortices produced either experimentally or numerically in TVCs had to make use of a mechanism to generate the desired velocity profiles, and, therefore, there is a degree of temporal and spatial fluctuation. These mechanisms imparted angular momentum using guide vanes or active fans that deflected the incident airflow about the geometric central axis of the chamber (e.g., [22, 32–41]). Alternatively, the entire wall, or a small section of it, may have rotated the air being pulled in and, in the reverse frame of reference, achieved much the same as having guide vanes, although this approach appeared to be less favoured recently (e.g., [42–49]). In numerical models, the rotation was accounted for by an equation that was applied to a design usually based on a physical TVC (e.g., [50–64]), although some models permit a dependence on z (e.g., [53, 65–68]), which was not observed to occur in experimental TVC models.

The swirl ratio was referenced in many of the aforementioned works in various forms. However, for the sake of comparison between different tornado datasets and the ones presented herein, it shall be defined by

$$S = \frac{\pi r_c^2 u_t(r_c)}{Q'} \quad (3.6)$$

where Q' is the volumetric flow rate through the relevant inflow boundary area [22]. This formulation was selected here over others that were available for its simplicity in applying it to non-TVC-based domains where only a location to measure Q' will need to be justified. Although it was not the most reliable method for comparing tornadoes of small-scale to full-scale [69], S did provide a satisfactory basis by which the datasets presented herein can be related to previous studies. If the inflow boundary is selected as the surface to calculate Q' , then the radius to this boundary as a multiple of the core radius, $R/r_c = \hat{R}$,

was found to be between 3.6–144.0 and 3.0–72.0 for experimental and numerical studies, respectively. The distributions of \hat{R} in each set of studies were skewed towards the lower end and so, to be conservative and ensure the datasets used in this work can accommodate the computation of Q' , the median of each (approximately $\hat{R} = 17.3$ and 14.6, respectively) will be used to place this hypothetical inlet boundary.

The u_t values presented in the literature were only recently scaled by $u_t(r_c)$, \hat{u}_t and then plotted against $\hat{r} = r/r_c$ (e.g., [34, 36–38, 40, 59]). This is represented schematically in Fig. 3.1, using a Rankine vortex model as an example. Note that the variables used in the scaling remain identical but the values of the variables could change from layer to layer such that the maximum u_t or value of r at that u_t would differ.

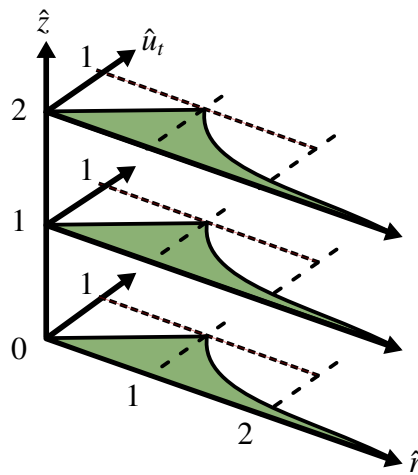


Figure 3.1: Schematic representation of a Rankine vortex's tangential velocity profile after scaling the velocity by maximum u_t and radius by r_c for three different heights scaled as $\hat{z} = z/r_c$

This scaling of velocity and radial position makes comparison of similar tornado intensities by their velocity profiles much simpler, although it forces all data to pass through position [1, 1], which can create visual similarity between dissimilar velocity profile datasets. Therefore, caution should be used when making comparisons between tornadoes by, for example, selecting the data measured from similar locations within vortices of comparable S values. Where possible, \hat{r} was found to range in the aforementioned experimental and

numerical studies, on average, between 0.39–9.40 and 0.22–7.00, respectively.

Tornado-like vortices were simulated in experimental and numerical laboratories with S values between 0.10–1.30 and 0.31–2.44, respectively, resulting in tornadoes of many different r_c values (from 0.5–69.0 and 0.8–115.0 cm, respectively). Depending on the S values of the datasets discussed in the next section, the u_t profiles found in the published literature will be selected based on comparable S values. The u_t profiles used in the comparisons made herein shall be measured from equivalent heights by using a height scaled to the core radius size, $\hat{z} = z/r_c$, as this quantity was readily available in the present datasets and the literature but is also a location with a physical basis in reality. As for \hat{r} , the average values of the upper and lower bounds of \hat{z} in the literature ranged from 0.33–3.05 and 0.60–2.00 for the aforementioned experimental and numerical studies, respectively. Conventionally, the selected height for measurement of the tornado variables (if scaled at all) would be tied to the simulation domain parameters such as the outlet radius (e.g., [35, 38], etc.). This is problematic in the case of the data used in this study where there were no such boundary conditions and the simulation domain was extremely large, such that an equivalent radius would be massive and arbitrarily defined. Refan and Hangan [39], Tang *et al.* [40], and Hangan and Kim [65] scale the height by the height at which $u_t(r_c)$ was a maximum, which could be a valid alternative. However, such data were not always readily available across all of the studies and so, for simplicity and consistency, scaling the height by the average r_c across all heights (for those datasets with only one measured r_c , that was chosen for the normalization factor) was preferred herein.

The importance placed on the damage rating of a tornado implies that all tornadoes may be categorized into well-defined, discrete types. However, there is no physical basis for considering that a tornado is constant through time and space. Tang *et al.* [41] utilize the velocity and pressure fields of their simulated vortex to analyse such variation by computing the temporal standard deviation, skewness, and kurtosis about the mean values. This use

was limited in that, for a given vortex, the data were measured by a single probe, and only the components' temporal variation was considered—no further analysis of spatial and temporal scaling factors derived from the raw component data were conducted. To the best of the authors' knowledge, this has yet to be examined and so computation of these statistics for the \hat{u}_t profiles are unavailable.

There are clearly many available tornado-like vortex models and these models were able to be compared previously in the literature to each other through various means of scaling such as using the swirl ratio or by normalizing velocity values using both the peak average tangential velocity and the core radius. However, almost none of these studies presented the asymmetry, tilting, and variation in wind gusts—even if present in their models. It should be possible, given enough data samples in both space and time, to conduct a more thorough analysis of the variation of the velocity components. Thus providing a sense of the scale of the asymmetry and tilting in comparison to the overall vortex structure. To perform such analyses, the finely resolved (both spatially and temporally) data from three supercell numerical simulations are used in this study and discussed in the following section.

3.1.3 Data Sources

The data discussed herein, in contrast to those referred to previously, are from tornadoes spawned within meteorological supercell numerical simulations. The parameters describing the reference tornado datasets used in this work are summarised in Table 3.1.

In the present work, the environmental conditions adjacent to a major tornado outbreak that occurred in the Southeastern United States on 27 April, 2011 is used as the ICs for a large eddy cloud model simulation (isotropic grid spacing of 10 m) of an isolated supercell thunderstorm that produces three different tornadoes throughout the storm's life cycle. The model parameters used for the CM1 model simulation in this environment are identical to those noted in [12], with over 1/4 trillion grid zones in, to the authors' knowledge, the

Table 3.1: Summary of referenced tornado data (with the year of simulation provided in parentheses) extracted from numerically simulated supercell thunderstorms

Parameter	Dataset		
	T ₁ (2019)	T ₂ (2022)	T ₃ (2022)
Duration, T [s]	1300	390	600
Domain Size [km]	$120 \times 120 \times 20$	$100 \times 100 \times 25$	$100 \times 100 \times 25$
Temporal Resolution, Δt [s]	1.0	0.2	0.2
Grid Resolution, Δl [m]	30	10	10

largest supercomputer supercell thunderstorm simulation conducted to date. The tornado data analysed in this chapter, saved at a temporal sampling rate of 5 Hz, represent the highest resolution full-physics-driven tornadic simulations known to the authors, and can be compared to both chamber simulations and field data.

As was the case for many of the full-scale tornado models, the surface BC was not set to no-slip as this was found to be ineffective at yielding tornadoes as the resolution needed for the near-ground grid spacing is too small for these large-scales with current computer hardware. Instead, a zero surface strain condition is applied, which is a type of free-slip condition that produces long-lasting tornadoes highly effectively in the CM1 model environment [70].

3.1.4 Objectives of the Present Study

The various methods used to generate a tornado-like vortex in prior literature have been discussed in depth and the advantageous data used in this study have been summarized in the previous sections. Given this, the current study aims to answer the following questions:

- a) Do circumferentially averaged u_r profiles from the present data match that of the published literature,

- b) What do these averaged data not capture in terms of temporal and spatial velocity fluctuation, and
- c) Why is consideration of spatial and/or temporal fluctuation in the computed flow-field quantities important?

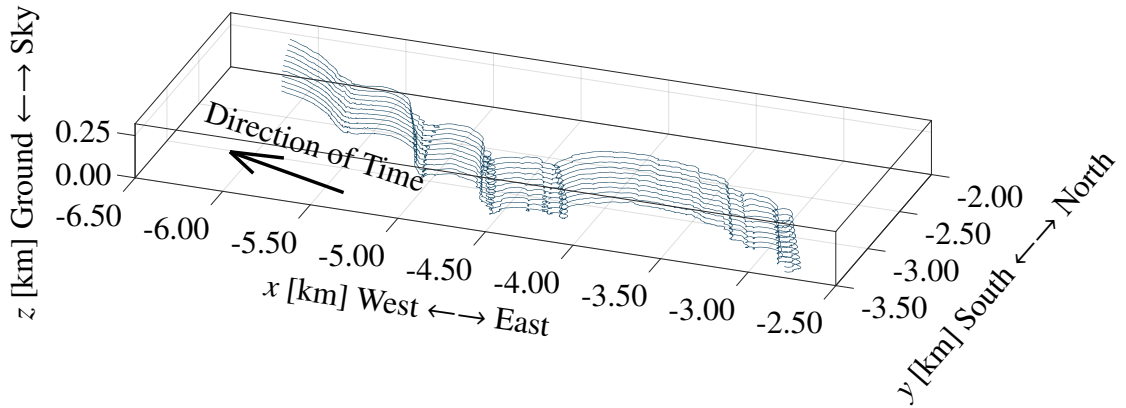
In the subsequent sections of this chapter, the tornado flow-field velocity vector components will be analysed by first using circumferential averaging around the axis of rotation but considering each horizontal plane in isolation. Then the time histories of potential spatial and temporal scaling factors will be explored. Finally, these time histories will be collapsed to provide context of the vertical variation of each of the computed values. Therefore providing future researchers the ability to compute the spread of values about the conventionally averaged one with a statistical basis for the upper and lower bound. This would then permit more accurate infrastructure wind-loading analyses to take place within the tornado-like vortex simulation chambers, both physical and numerical, that already exist without modifications to the simulation setup.

3.2 Methodology

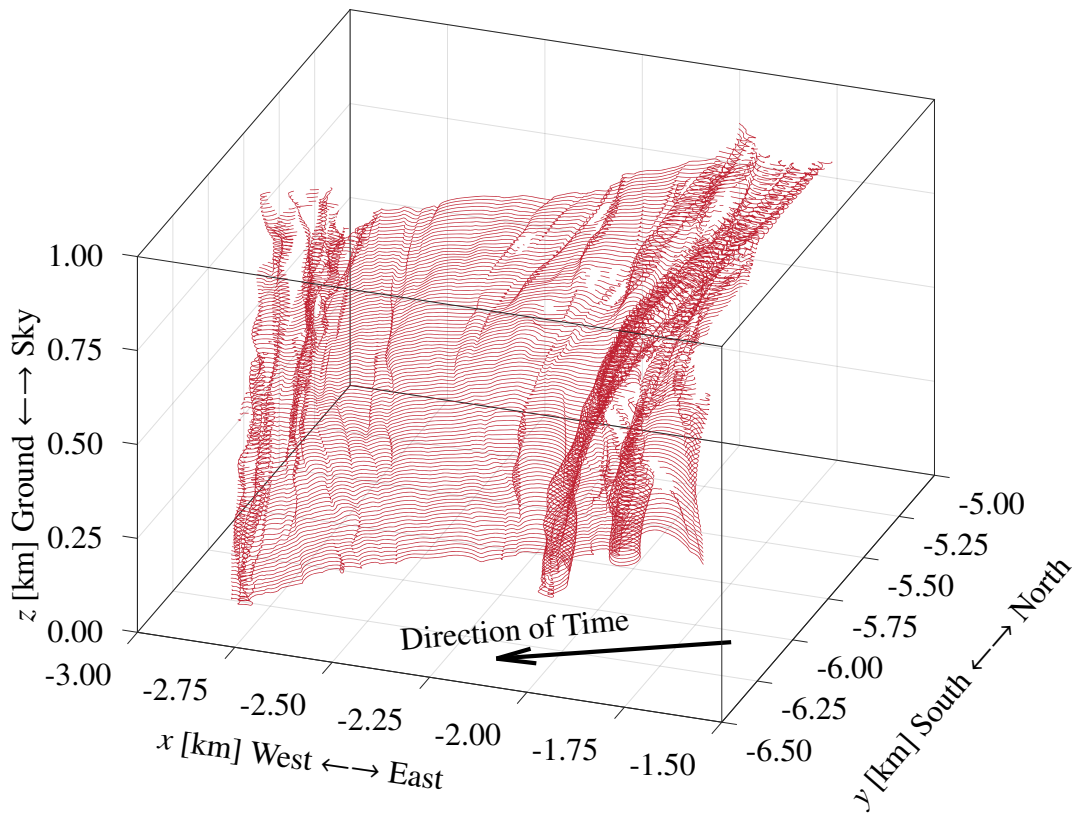
The process used to convert the raw data into a usable dataset for flow-field statistical analyses is described in the following section. Then the calculations used to generate the plots presented in Sect. 3.3 are explained in detail.

3.2.1 Data Processing

Each of the three tornado datasets generated for use in this work, as described in the previous section, is first processed by applying the method of Bannigan *et al.* [71] to locate the centre position of the dominant tornado vortex in each horizontal slice at each vertical height (Fig. 3.2).



(a)



(b)

Note that the axis of rotation is taken to be vertical when considering each horizontal layer of data separately, to limit the scope of the current work. The axis passes through the point of zero horizontal velocity within a tornado core, which is one of several methods to identify the centre of a vortex [72], and by the bounded region of maximum curl [71]. Although

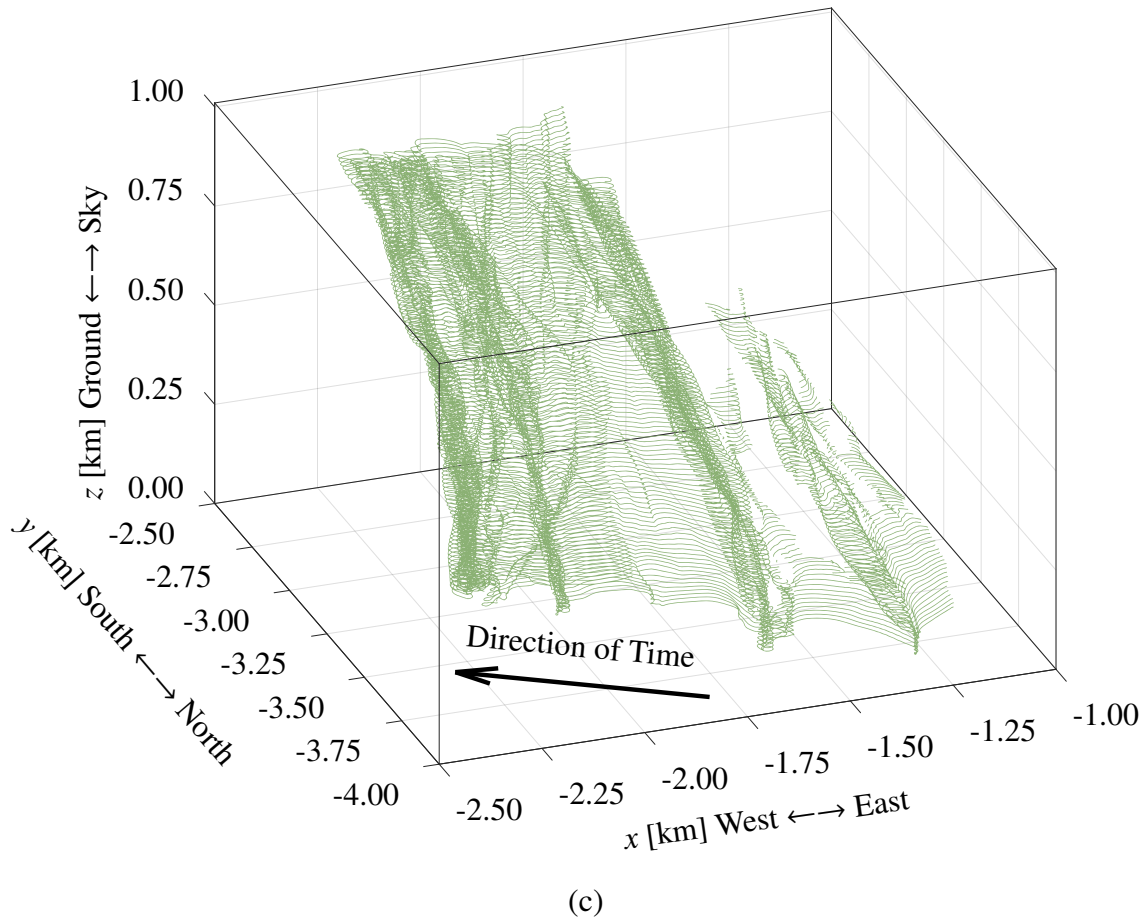


Figure 3.2: Trace of the (a) T_1 , (b) T_2 , and (c) T_3 tornado centre positions through time on each xy -plane slice of data

there are other, valid, methods for finding the centre position of a vortex (e.g., [73–76]), it is beneficial to define the centre of a velocity profile so that the origin of the profile is at a precise point that is spatially consistent with time [71]. This position therefore becomes the datum by which to describe all other locations in that xy -plane of the data. The centre location is computed for the entire lifetime of the simulation data and stored for all timesteps wherever the vortices in each dataset are both visually present and traceable by the centre tracking algorithm for the ground relative² velocity (see Fig. 3.3).

²The velocity in the raw data are relative to the motion of the domain grid, this is to prevent the relevant tornado from escaping the domain or needing to save an excessive amount of data that would not be needed. Thus, from the saved raw signal, the motion of the domain can be added again to the wind-field to get back to the ground relative velocity

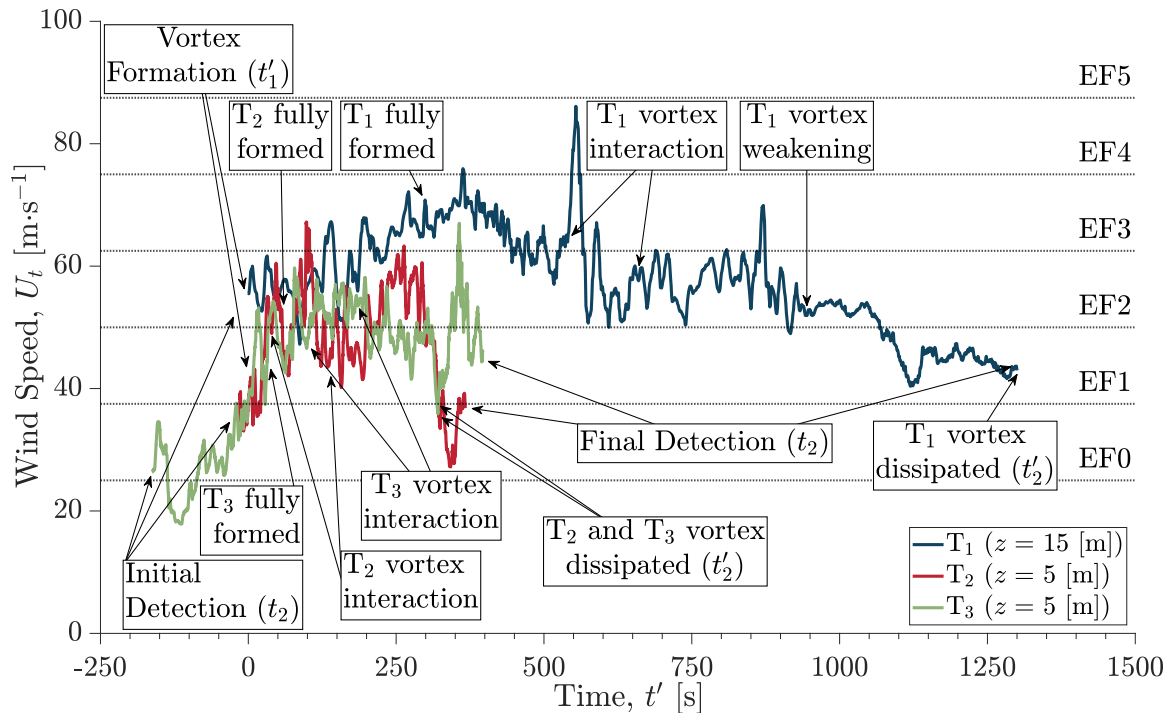


Figure 3.3: Variation of the maximum absolute tangential wind velocity relative to the ground for all tornado datasets. The labels identify events of significance that occurred over the duration of each tornado life-cycle

In each of the simulations, there were many vortices present (e.g., 34 were detected in T_2 over the entire dataset) but only the longest living vortex of greatest intensity was selected as the tornado of interest in each case. Once these vortices were identified, the period of analysis used in the present work was chosen such that the initial time of each vortex's life, $t' = 0$, coincided with the start of the time over which the vortex was visually present in the wind-field and had crossed above the EF 1 threshold until the final time, t'_2 , which was roughly defined by the vortex intensity dropping below the EF 1 rating and was visibly weakening (Fig. 3.3). This definition may be applied to each dataset and indicates tornado dissipation. This ensures that events within the domain that are independent of the vortex of interest are not included in the following analyses. It was necessary to visually check such instances because u_t appears to increase suddenly but this is not necessarily the influence of the tornado itself. For example, in the case of T_3 at $t \approx 350$ s a dominant flow from the south-west of the domain begins and the main vortex has already weakened. Thus,

Table 3.2 summarizes the duration of each tornado in each dataset and the equivalent time relative to the provided data.

Table 3.2: Summary of lifespan of the main vortex in each tornado dataset. All times are given with respect to the initial time, t'_1 s, in each dataset

Parameter	Dataset		
	T ₁	T ₂	T ₃
Initial Detection Time, t_1 [s]	0.0	-20.4	-162.0
Final Detection Time, t_2 [s]	1299.0	367.0	397.0
Vortex Initial Time, t'_1 [s]	0.0	0.0	0.0
Vortex Final Time, t'_2 [s]	1300.0	321.4	319.2
Total Time, T [s]	1300.0	321.4	319.2
Total Timesteps, ΔT	1300	1607	1596

3.2.2 Coordinate Conversion

The Cartesian coordinate system is converted into cylindrical coordinates with the centre of each tornado as the origin of its domain. This allows discussion of tornado variables with respect to a single point that is known, rather than approximated or assumed *a priori*, and, thus, spatially consistent through time. To ensure that the coordinate system does not extend beyond the given dataset, resulting in errors, a programmatic limit is placed on the radius of the new coordinate system so that it is constrained by the minimum of the maximum distances from the origin to the edge of the data in each domain for all horizontal planes. Therefore, the distance from the tornado origin to the outermost circumference, R , of each dataset is fixed over all horizontal layers at each timestep but varies with time. Although this conversion process means that a significant amount of the data is excluded, because the aspect ratio of the xy -planes is not unity, the tornadoes are still represented by the new coordinates as the vortices are much smaller than the original, translating domain. By having fewer points, additional analyses may be conducted more rapidly, focusing on the most crucial data and framed with respect to the tornado centre. The points that form

each circumference are created and spaced at equal arc lengths, not equal angles, so that, as the circumference increases, the resolution of the dataset remains the same and the information within the original Cartesian coordinate system is maintained (see Fig 3.4). The arc length, s , could simply be set equal to the grid spacing of the original domain, Δl , which is 30 m for T_1 and 10 m for the other two datasets. However, s is set to $\Delta l/2$ to achieve a balance between avoiding discarding data within the tornado core where the circumference is small and sub-sampling the datasets. The radial spacing between circumferences is also set to $\Delta l/2$ to maintain consistency of points in the new cylindrical coordinate system rather than biasing or stretching the data in the wind-field.

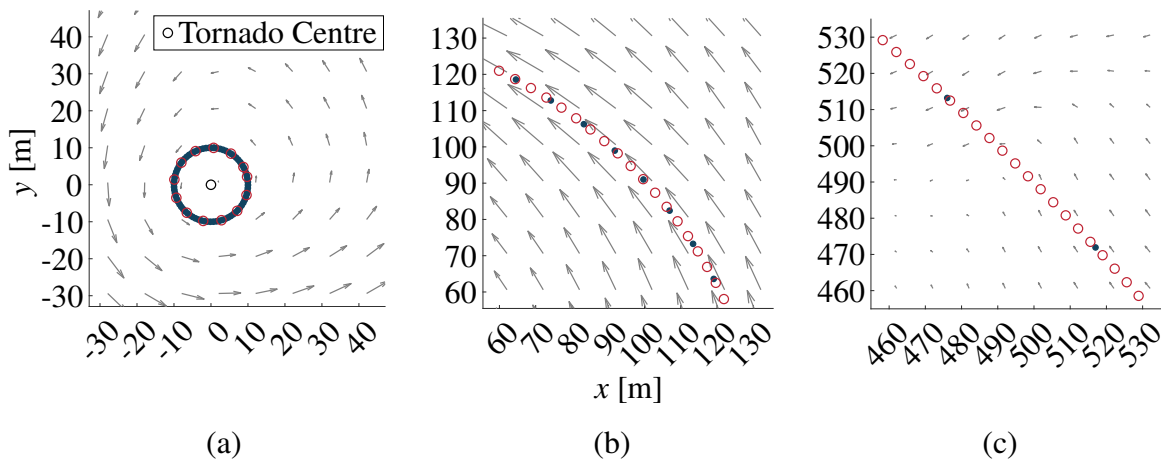


Figure 3.4: Demonstration of the differences in cylindrical coordinate spacing when using equal arc length spacing (shown as red circles) versus equal angular spacing (shown as dark-blue dots) for (a) at $\hat{r} = 0.1$, (b) at 1.0, and (c) at 5.0

The number of points, n_r , around each circumference in this new coordinate system is related to the radius, r , and arc length, s , as described by

$$n_r = \frac{2\pi r}{s} \quad (3.7)$$

The components of each variable in the x -, y -, and z -directions are converted into the radial, r ; tangential, t ; and vertical, z components with respect to the centre of the tornado, O (as in Fig. 3.5 for the velocity components).

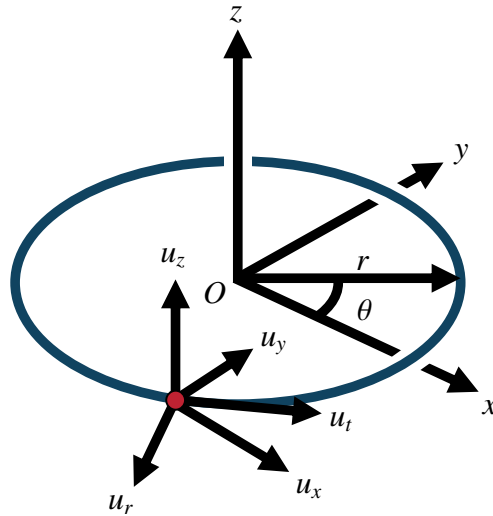


Figure 3.5: Schematic of the coordinate transformation, shown for the velocity components

Next, utilising a bi-linear interpolation method, the x , y , and z components of each desired variable at all points in the cylindrical coordinate system, with respect to the nearest four points of the Cartesian coordinate system, are calculated (see Eq. 3.8 for the velocity vector coordinate transformation).

$$\begin{aligned} u_t &= \frac{x - x_O}{r} u_y - \frac{y - y_O}{r} u_x \\ u_r &= \frac{x - x_O}{r} u_x - \frac{y - y_O}{r} u_y \end{aligned} \quad (3.8)$$

The vertical velocity, u_z , in cylindrical coordinates remains the same as in Cartesian coordinates. It is now possible to compute the spatial and temporal quantities of any variable desired for further analysis, as long as it exists within the dataset. For the scope of the present work, the focus of this analysis will be limited to the velocity vector-field because the asymmetry and tilting discussed is directly in reference to the velocity. These same analysis techniques could also be extended to apply to the pressure field.

3.2.3 Variability of Velocity Profiles

As explained in Sect. 3.1, it is common to use the circumferentially averaged tangential velocity profile to analyse tornadoes. Thus, it shall be replicated here by taking the average of values around each circumference from the identified velocity centre in each tornado case. The timestep shall be chosen to be the nearest to the halfway point, $t'_{1/2}$, to be as fully developed as possible, which is also between the two median values of \hat{R} found in the literature (see Sect. 3.1.2). For T₁, T₂, and T₃, these times are $t' = 713, 196,$ and 133 s with $\hat{R} = 15, 16,$ and 15 , respectively. To select literature with which the present data may be compared, the S value must be matched as closely as possible, which involves first calculating Q' . Given that there is no artificial forcing of the velocity vectors around the hypothetical inlet surface at \hat{R} radii, Q' will be approximated using,

$$Q' = \langle \mathbf{u} \rangle A \quad (3.9)$$

where $\langle \mathbf{u} \rangle$ is the spatially averaged velocity vector around the relevant radius and over all heights. The resulting value can then be applied to calculate Q' and, subsequently, S for each tornado dataset. Therefore, $S = 1.36, 0.43,$ and 0.55 , respectively. Most of the datasets are thus acceptable to use for comparing to the velocity profiles of the present data but those that match most closely include: Church *et al.* [47], Haan *et al.* [34], Hangan and Kim [65], Kuai *et al.* [66], Ishihara and Liu [60], and Tang *et al.* [40]. The \hat{z} of velocity data available in these studies, for the specified S ratio, are summarised in Table 3.3.

Although not all of the studies selected apply to all of the present data, the selection does include some overlap with each individual dataset having a basis of comparison with at least two of the selected studies. Of the discussed analytical tornado simulation methodologies, Rankine [24], Burgers [25], and Wen [28] will be plotted alongside the above as they each utilize different approaches to produce a vortex flow and are still often cited in the published

Table 3.3: Summary of the studies with equivalent S and the heights and radii over which velocity profile data are available

Study Selected	Type	Swirl ratio, S	Heights, \hat{z}	Radii, \hat{r}
Church <i>et al.</i> [47]	Exp.	0.34	0.60, 3.30	0.32–7.50
Haan <i>et al.</i> [34]	Exp.	1.14	0.10–0.55	0.20–7.60
Hangan and Kim [65]	Num.	1.50	0.18–0.68	0.00–7.30
Kuai <i>et al.</i> [66]	Num.	1.11	0.63	0.00–4.60
Ishihara and Liu [60]	Num.	0.65	0.20–2.00	0.00–2.00
Tang <i>et al.</i> [40]	Exp.	0.17–0.84	0.05–0.34	0.00–8.00

literature. Sullivan [26] is excluded due to its similarity to Burgers [25], but would have also been a valid option.

Now that it will be possible to reasonably compare the present datasets with the available literature, the first step will be to compute the spread around each value from each radius in the averaged tangential velocity profile. In this study, the standard deviation, σ , is used as a simple means of demonstrating this spread at the same time and height ratios in each tornado. This assumes a roughly normal or uniform distribution, which is evaluated by computing the skewness and kurtosis, where the (sample) skewness, \bar{u}_3 , is given by (see [77])

$$\bar{u}_3 = \frac{\frac{1}{n_r} \sum_{i=1}^{n_r} (x_i - \langle x \rangle)^3}{(\sigma_{x_i})^3} \quad (3.10)$$

and the (sample) kurtosis, b_2 , is given by (see [78])

$$b_2 = \frac{\frac{1}{n_r} \sum_{i=1}^{n_r} (x_i - \langle x \rangle)^4}{(\sigma_{x_i})^4} \quad (3.11)$$

or, both can be modified for bias correction as follows, for the cases where $n_r < 30$ (note that $n_r > 3$ otherwise it is not possible to compute a value),

$$\bar{u}_{3,m} = \frac{\sqrt{n_r(n_r - 1)}}{n_r - 2} \bar{u}_3 \quad (3.12)$$

$$b_{2,m} = \frac{n_r - 1}{(n_r - 2)(n_r - 3)} [(n_r + 1)b_2 - 3(n_r - 1)] + 3 \quad (3.13)$$

where x_i is the variable of interest, which, in this case, are the three velocity components at a fixed radius for any timestep or height, $\langle x \rangle$ is the spatial average of x_i around the circumference, n_r is the number of points in a given radius, and σ_{x_i} is the standard deviation of the x_i points. Therefore, these quantities, taken over time and at all heights at $r = r_c$, can be averaged in time and then the standard deviation computed, as with the velocity values, to demonstrate the spatial and temporal fluctuations individually.

3.2.4 Maximum-to-Average Velocity Ratio

If there is a considerable deviation of values about the average, in particular a deviation above the peak average velocity value, it would be desirable to determine whether there is a consistent ratio by which an average velocity can be converted into a reliable estimation of the maximum velocity. Thus, a maximum-to-average velocity ratio is defined by,

$$\hat{U}_t = \frac{\max |u_t|}{\langle u_t(r_c) \rangle_r} \quad (3.14)$$

and applied to each height and timestep so that the maximum velocity present within the tornado is normalized by the averaged velocity at the core radius, r_c .

3.2.5 Spatial-Peak Factor

Another approach to correlating the relationship between the maximum u_t and peak $\langle u_t \rangle_r$ values would be to subtract the latter from the former and then normalise by the spatial standard deviation of values around the averaged circumference. This ratio is commonly known as the gust factor, k , where a fixed location is used to measure a wind-field signal and compute the ratio of the difference of maximum and average values to the standard deviation of that signal. However, in the present cases, what is to be noted as the “spatial-peak

factor” and indicated as κ allows for the motion of the vortex such that the measurements are taken relative to a location of physical quantities (i.e., the radial position of the average velocity is free to change in time as is the location of the maximum tangential velocity value). Therefore, κ , is given by,

$$\kappa(r_c) = \frac{\max |u_t| - \langle u_t(r_c) \rangle_r}{\sigma_{u_t}(r_c)} \quad (3.15)$$

3.2.6 A Vortex Timescale

Thus far, the analyses focus on the spatial variation within the vortex structures, but now some consideration of the temporal fluctuation is considered. If a parcel of air were to be followed, approximately, as it translated around the circumference of each vortex, a timescale associated with that may be defined by

$$\tau = \frac{2\pi r_c}{\langle u_t(r_c) \rangle_r} \quad (3.16)$$

Other timescales may be defined, but τ informs one of the expected fluctuations in the measured parameters every τ seconds versus those present due to other motions occurring in the events that are not a result of the same air parcel arriving at the measurement point.

3.2.7 Turbulence Analysis

In addition to discussion the spread of values about an average, it is also important to understand the higher-frequency fluctuations produced by turbulence present in the tornadoes at various positions within the vortices and how significant those fluctuations are. To compute this, the turbulent kinetic energy will be calculated at several representative locations for several different averaging windows to smooth data within different time-blocks. The representative locations are chosen as before, where the height is based on ratios from the

literature. Additionally, data are collected from the four main cardinal positions. Therefore, there are 36 spatial positions used in this analysis and the average of the turbulence values at each shall be presented, together with their respective temporal ranges.

However, before this takes place, it is necessary to determine a window-size, n_w , in seconds over which the data may be smoothed and to determine what proportion of the total fluctuation energy is being eliminated by subtracting the large-scale fluctuations. First, appropriate time-blocks, b , over which the window averaging may take place shall be established. Values of $t_b = 1.0, 2.5,$ and 5.0 minutes are selected. This is due to the limited temporal data available, especially for T_2 and T_3 where, although they are temporally better resolved than T_1 , the timesteps convert into approximately five minutes of data within the aforementioned time period, t' . To select an appropriate value for n_w , the statistics of the residual velocity, $u_i - (\overline{u_i})_{n_w}$, for odd values of $n_w = 0$ to $(60t_b - 1)$ will be computed. The value(s) at which the size of the window no longer significantly affects any of the quantities shall be selected as the n_w value. In each case, the number of usable computed data will be $N = [60t_b - (n_w - 1)] \cdot t_i$. Once n_w has been determined through inspection, the total turbulent kinetic energy (TKE), k , in $\text{m}^2 \cdot \text{s}^{-2}$ and the root-mean-square (RMS) of velocity fluctuations, I , in $\text{m} \cdot \text{s}^{-1}$ can be computed. I is also known as the turbulent velocity fluctuation associated with the TKE in the domain. The sub-grid scale (SGS) TKE data used as part of the total TKE are computed in these simulations using the CM1 TKE scheme [79] but are no longer available for T_1 and as such the total TKE can only be discussed for the other two datasets. For the sake of completeness, the TKE data without the SGS values from T_1 are still included here but should be regarded with caution.

The analyses are conducted such that the total five minutes are centred on $t'_{1/2}$, cutting off a small amount of data either side for all of the datasets. Thus, five blocks for $t_b = 1.0$ minutes, two for $t_b = 2.5$ minutes, and one for $t_b = 5.0$ minutes. For consistency, the additional timesteps available for T_1 resulting from the larger Δt are neglected. Therefore,

there are 36 locations of eight time-blocks of data from the three velocity components in each of the three tornadoes. To determine how much of the large-scale fluctuations are being subtracted from the residual analysis, the RMS and the variance, σ^2 , of:

- a) the mean signal across the time-blocks, $(\bar{u}_i)_b$,
- b) the window filtered mean signal, $(\bar{u}_i)_{n_w}$, and
- c) the residual of window filtered mean signal, $u_i - (\bar{u}_i)_{n_w}$,

are computed for each spatial location and velocity component and a quantitative comparison of the difference between b) and c) will indicate how much of the total fluctuation energy, given by a), is removed. If all of the values for each velocity component are of the same order of magnitude, then all the components can be summated to compute an overall value for TKE and RMS of the turbulent fluctuations in the subsequent calculations.

The temporal residuals of the velocity components are computed using $u_i - (\bar{u}_i)_{n_w}$ at the nine positions of each cardinal point, separately. The components can then be summed to obtain the TKE for each time-block by,

$$k = \frac{1}{2} \sum_{i=1}^3 \left[\overline{u_i - (\bar{u}_i)_{n_w}} \right]_{t_b}^2. \quad (3.17)$$

To be useful in making comparisons between these datasets and to others in the future, the TKE shall be normalized by the square of the tangential velocity,

$$\hat{k} = \frac{2k}{(\bar{u}_t)_{t_b}^2} \cdot 100\% \quad (3.18)$$

which is chosen as a method of normalisation because it is the dominant velocity component in a tornado by definition.

For the RMS of the turbulent fluctuations, the same method of computation as for TKE will

be employed. The equation is given by,

$$I = \sqrt{\frac{1}{3} \sum_{i=1}^3 [u_i - (\overline{u_i})_{n_w}]^2} \quad (3.19)$$

where I is also normalized using the tangential velocity. This is given as a percentage and referred to as the turbulent intensity (TI),

$$\hat{I} = \frac{I}{\sqrt{(\overline{u_t})_{t_b}^2}} \cdot 100\%. \quad (3.20)$$

3.2.8 Fixed Probe Analysis

A final step to analyse the tornadoes is to consider what the vertical profile of horizontal velocity might look like from a fixed location (relative to the ground) as the tornadoes approach, pass over, and move away from said location. To be rigorous in collecting this information, without generating an overwhelming amount of data, the four principal cardinal positions are selected relative to the vortex centre to place hypothetical sensors for detecting the velocity wind-field. These hypothetical sensors will also be able to detect the velocity at all heights and be completely vertical. These “probe towers” shall be located at a distance of $r = r_c$ from the tornado centre for the r_c value when $t = t'_{1/2}$ at indexed height, $z_i = 1$. This ensures that the vortices in each case are well-developed during the period of analysis, which spans from the time that the final tower probe enters the domain until the first tower probe exits. In the current datasets, the domain of wind-field values are each a slice of a much larger simulation domain. This is done to minimize the resultant file-size without compromising the quality of the subsequent analyses. This action requires approximately following the tornado in the full-size simulation domain at a velocity that

is determined *a priori*³. This domain velocity, \mathbf{u}_m , was chosen to approximately match the bulk motion of the tornado vortex and is a constant. For each tornado, $\mathbf{u}_m = \langle 15.20, 10.50 \rangle$, $\langle 18.75, 9.00 \rangle$, and $\langle 18.75, 9.00 \rangle \text{ m}\cdot\text{s}^{-1}$, respectively, where the first coordinate is the velocity in x and the latter in y . Therefore, to have these so-called probe towers, it is necessary that, relative to the tornado centres, they move at a velocity $\mathbf{u}_{\text{tower}} = -\mathbf{u}_m$. A simplified schematic showing the plan view of this setup can be seen in Fig. 3.6.

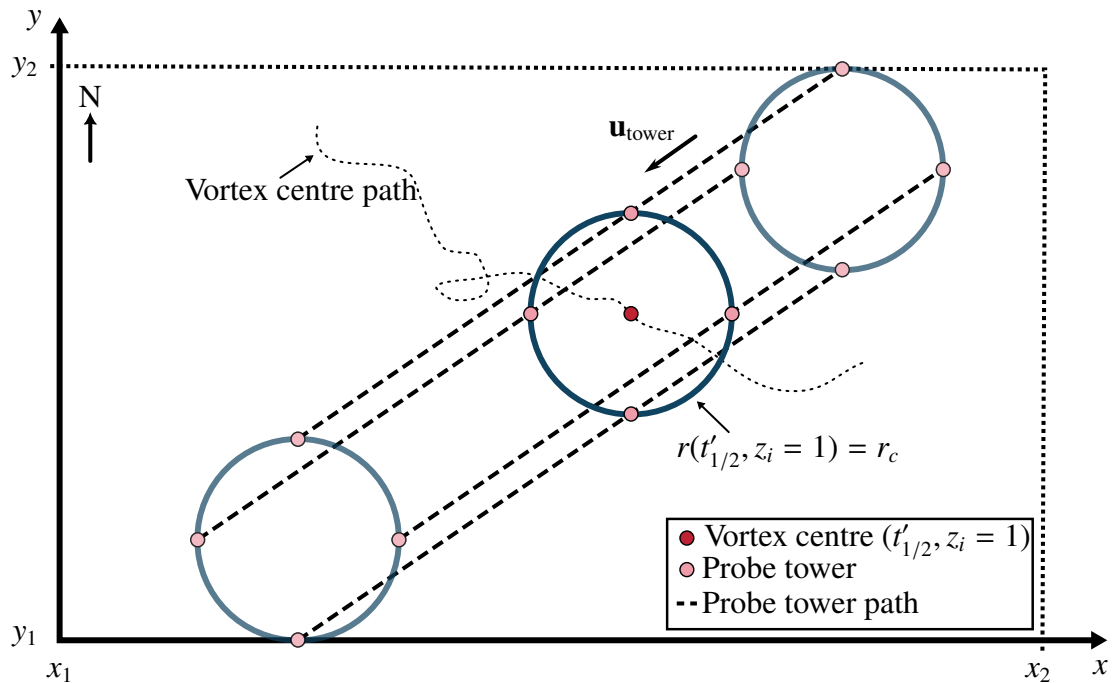


Figure 3.6: Plan-view, schematic representation of tower probe placement and motion relative to a tornado centre that is also in motion relative to the reduced domain inside a larger, simulation domain

3.3 Results and Discussion

The results of applying the methods detailed in the previous sections are discussed here. The data used in the present study are shown to be comparable with those of the literature. Then, the spread of that data is shown and the associated statistics of the velocity distribu-

³All velocities in this study are given with respect to the ground and so each point in the wind-field has had \mathbf{u}_m added again but the positions are fixed in space relative to the reduced domain for simplicity.

tion are computed. The scaling between the average and maximum tangential velocities are computed and the proposed timescale is computed. Finally, an analysis of the turbulence is developed and the vertical profile of the horizontal velocity is shown.

In the present data, r_c was found to be consistent over the height of the tornadoes with average values between approximately 74–195, 30–75, and 75–140 m, for each dataset, respectively (see Table 3.4). The standard deviation about the average values was approximately 5.3, 19.7, and 16.1 m, respectively. In all cases, the maximum r_c value was found to be at around $t'_{1/2}$ and a minimum at t'_1 and t'_2 . The circumferentially averaged core tangential velocities, $\langle u_t(r_c) \rangle_r$ were approximately between 21–45, 18–43, and 24–40 $\text{m}\cdot\text{s}^{-1}$ for each tornado dataset, respectively (see Table 3.4). They had fairly tight standard deviations about the means of 0.78, 3.64, and 2.68 $\text{m}\cdot\text{s}^{-1}$, respectively. Though the velocity values at the ground level of each tornado differed significantly (see Fig. 3.3), when averaging over the entire height of the tornado each fell within similar ranges of values. Averaging again, over time, gives a tangential velocity about the core radius of 34.2, 34.6, and 35.6 $\text{m}\cdot\text{s}^{-1}$, respectively. However, averaging in all of these ways at once is arbitrary and one should be careful when interpreting the results. There is no clear reason for the present tornadoes, which are of different sizes, strengths, durations, and ICs, to collapse to such similar values for the tangential velocity at the core radius.

The above values were then used to generate the ratios used to compare these data with respect to the literature. The available range of \hat{z} were found to be approximately 0 (i.e., ground level) to 1.22, 6.93, and 5.04, respectively. In terms of \hat{z} , values from approximately 0 to 12.11, 17.05, and 9.83, respectively (see Table 3.4).

Table 3.4: Summary of the present data characteristics. The core radius, r_c , and tangential velocity at r_c , $u_t(r_c)$, were the average values over the height of the domain and the range in each represents the variation with respect to time

Dataset	Core Radius, r_c [m]	Core Tangential Wind Speed, $u_t(r_c)$ [$\text{m}\cdot\text{s}^{-1}$]	Swirl ratio, S	Heights, \hat{z}	Radii, \hat{r}
T ₁	75–195	21–45	1.36	0.11–1.22	0.00–12.11
T ₂	30–75	18–43	0.43	0.07–6.93	0.00–17.05
T ₃	75–140	24–40	0.55	0.05–5.04	0.00–9.83

The data from each simulated event, having been processed and filtered such that only the relevant timesteps and horizontal slices of the wind-field data remain, can now be analysed. Firstly, a sample of circumferentially averaged tangential velocity radial profiles, representative of the profile shape across much of the time series, is shown in Fig. 3.7.

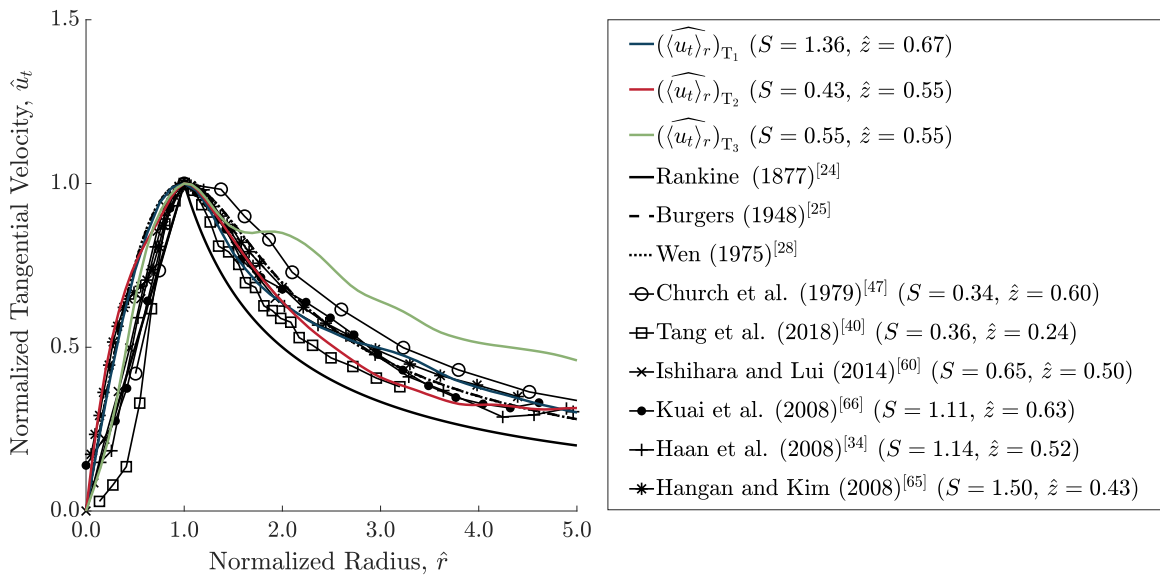


Figure 3.7: Comparison of the normalized profiles of spatially averaged tangential velocities present in various tornado vortices at height and time slices representative of the time series of each tornado

It was determined that either side of the tangential velocity peak, $\hat{r} = 1$, the tornado data in each of the present cases were in close agreement with the published literature for both the analytical and measured profiles. T₁ and T₂ trended together for most of the radii, whereas T₃ was distinct for almost all of the radii. Instead, T₃ followed most closely to Burgers [25]

and Wen [28] for $\hat{r} \leq 1$, but fell below them for $\hat{r} > 1$ and was closer to Hangan and Kim [65].

Before discussing the spread of the velocity data, the statistics of each dataset were computed. It was found that the skewness, \bar{u}_3 , was centred on 0 in all three datasets, with the only difference being that T_1 had much less spread about that time-smoothed average than T_2 and T_3 at around ± 0.2 for the former and ± 0.6 for the latter two. This result was also consistent over all heights. Therefore, the data in all three cases were centred on the mean. A skewness of approximately 0 should be expected if the distributions were perfectly symmetrical about the mean and this is, indeed, generally seen in the data. For the kurtosis, b_2 , a similar result emerged such that the value remained consistent with height in all three cases with a mean with the spread of a single standard deviation of approximately 1.5 ± 0.25 for T_1 , 2.0 ± 0.50 for T_2 and T_3 . This was the unmodified kurtosis meaning that a value of 3 indicates a perfectly normal distribution; since these data were below that threshold it indicates thicker tails (i.e., more extreme velocity values) about the mean value compared to a perfectly normal distribution [80]. Thus, to gain insight into the asymmetry present in these tornado data, the spread of the tangential velocity about the circumferentially averaged profile was analysed (Fig. 3.8).

The sample size was a function of the radius, increasing linearly with r , and so caution should be taken in drawing conclusions from data in the region $\hat{r} \leq 1$. However, it was clear that the spread of the tornado data in each case were significant about $\hat{r} > 1$ for T_1 and T_3 with a standard deviation of approximately 50% of $\hat{u}_t(r_c)$ extending out to about $\hat{r} = 1.25$ and this spread stayed consistently large as $\hat{r} \gg 1$. T_2 displayed a much smaller spread, $\sigma \approx 0.1\hat{u}_t(\hat{r})$ as the radius increased. This may have been caused by another vortex forming nearby. Even though T_2 displayed much less spread, at these timesteps and heights, it should be clear, in all cases, that by being able to place the circumferentially averaged value alongside a standard deviation, it should be possible to generate subsequent

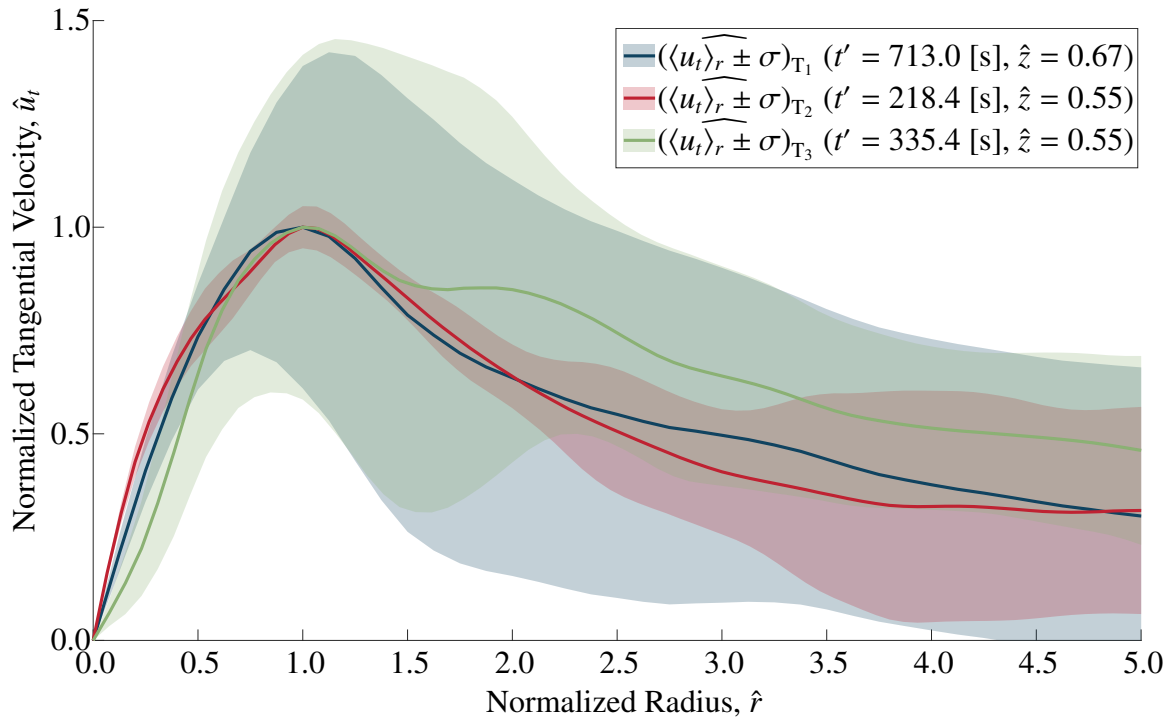
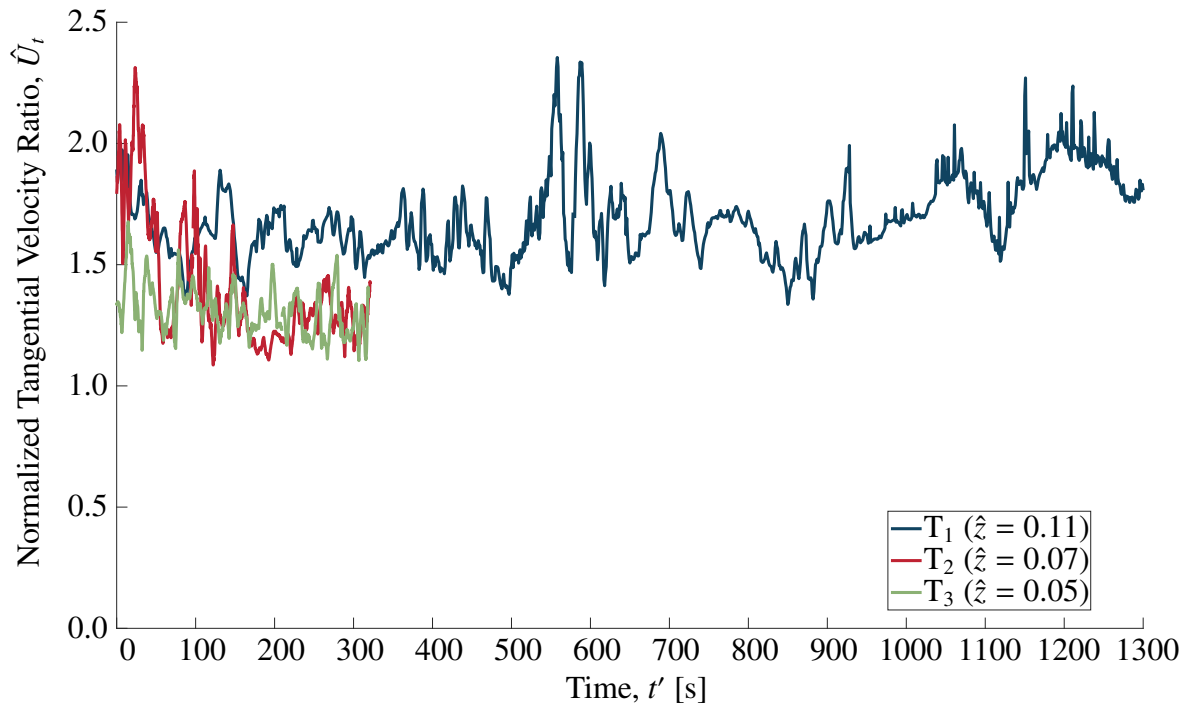


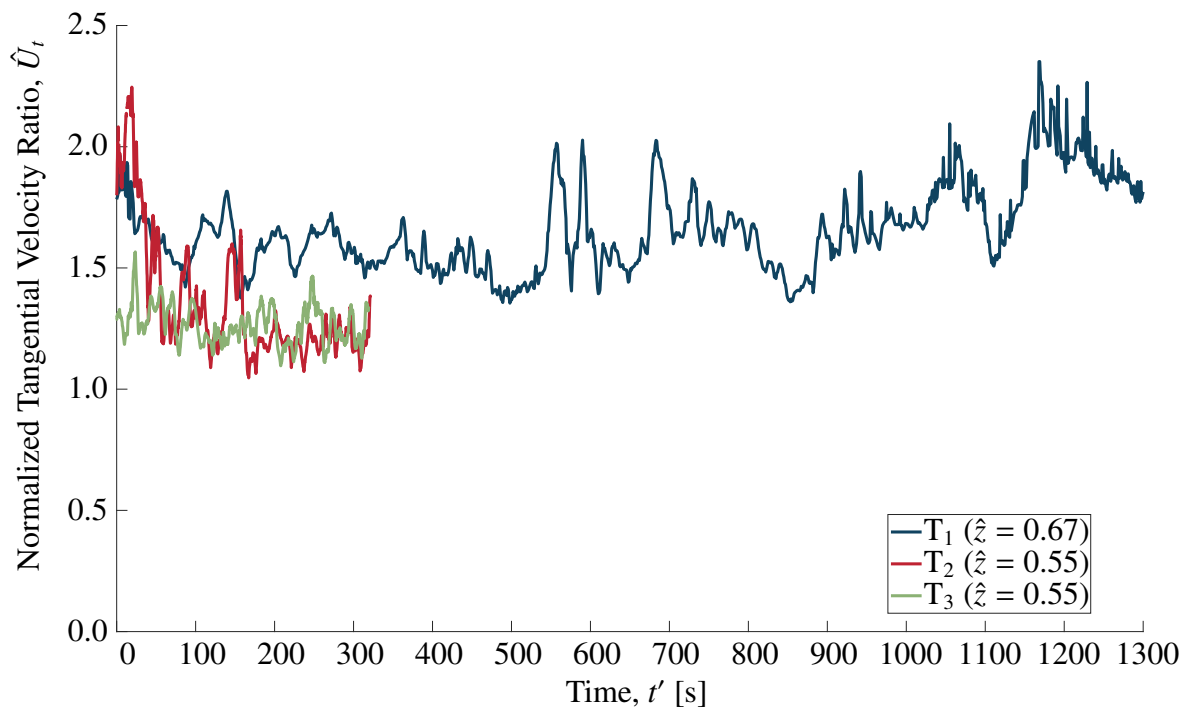
Figure 3.8: Demonstration of the spread of the normalized profiles of spatially averaged tangential velocities. The shaded region indicates the range of normalized velocity bounded by the average value \pm one standard deviation

wind-loading analysis to any desired statistical confidence level in the value.

Next, it was considered whether a consistent ratio, \hat{U}_t , could be determined to relate each tornado's maximum $\langle u_t \rangle$ to the instantaneous maximum, u_t , value (Fig. 3.9).



(a)



(b)

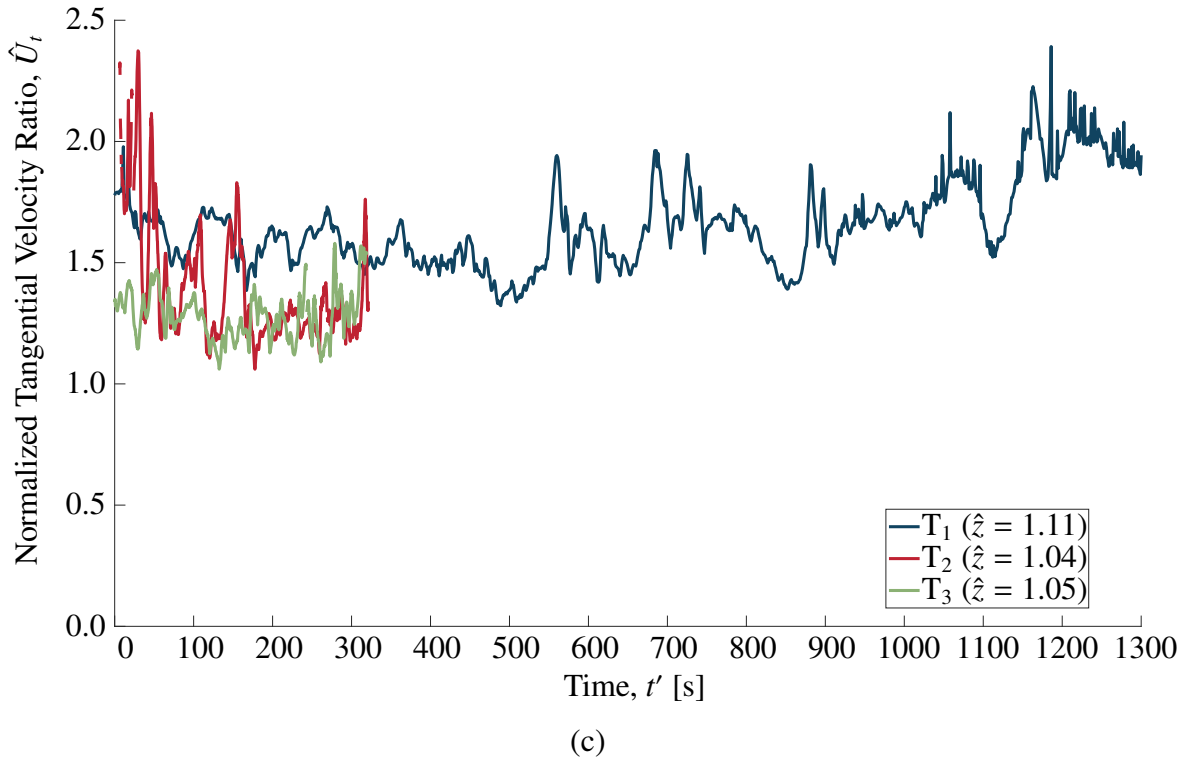


Figure 3.9: The ratio, \hat{U}_t , of the peak maximum tangential velocity, $\langle u_t \rangle$, present in the entire tornado to the peak circumferential average tangential velocity, u_t , at $\hat{z} \approx$ (a) 0.00, (b) 0.50, and (c) 1.00 plotted against time

The relationship was plotted as a time history for three representative heights, selected to be close to the ratios found in the literature (see Table 3.3) but also constrained by the smallest available \hat{z} in the present data (i.e., T_1) so that there was a low, a middle, and a high value. Therefore, a location as close to the ground level as possible was selected first. Then, $\hat{z} \approx 0.5$ represented a mid-height location and, finally, $\hat{z} \approx 1.0$ represented a far above the ground location. This final ratio approached the maximum height available in T_1 but was only approximately one-fifth of the way up the total tornadoes in T_2 and T_3 , however, this kept consistency amongst the datasets and allowed for comparison with all of the desired literature referenced in Sect. 3.2.3. These ratios are used in all of the remaining computations herein.

In general, \hat{U}_t was larger for T_1 than the other two datasets at around 1.75. The \hat{U}_t value

for T_2 was less consistent but was aligned closely with T_3 at approximately 1.25. Given that the results were similar for each selected height, the variation with height was also explored in Fig. 3.10.

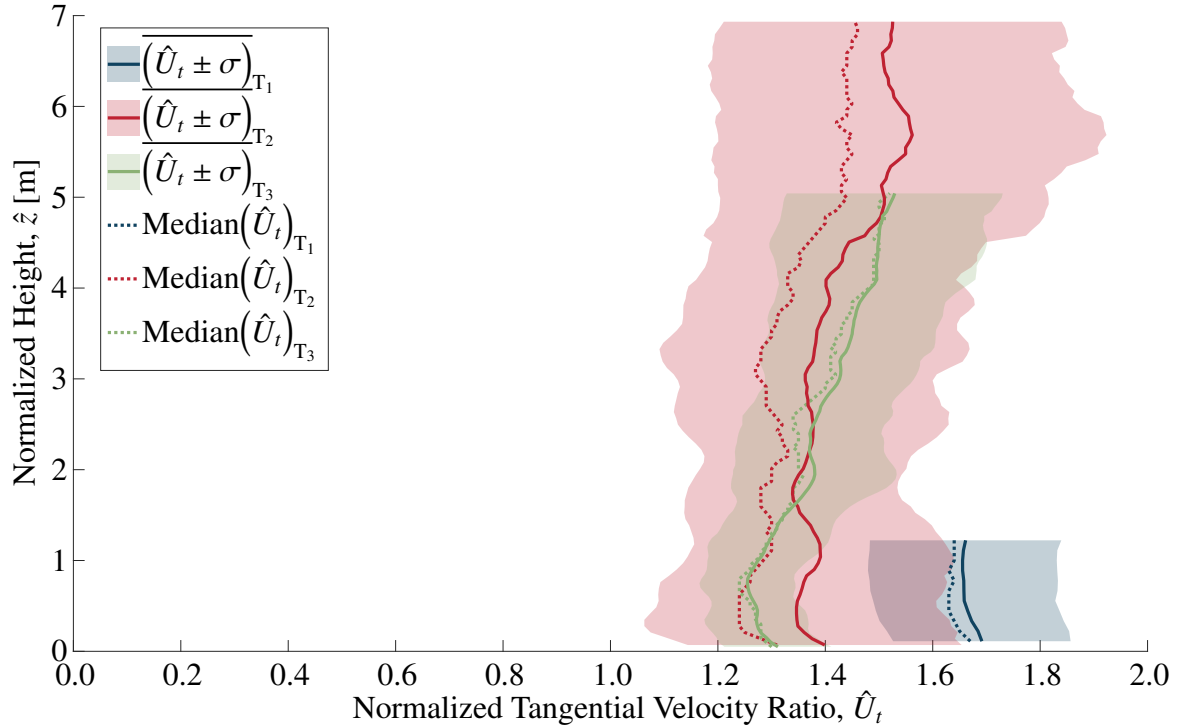
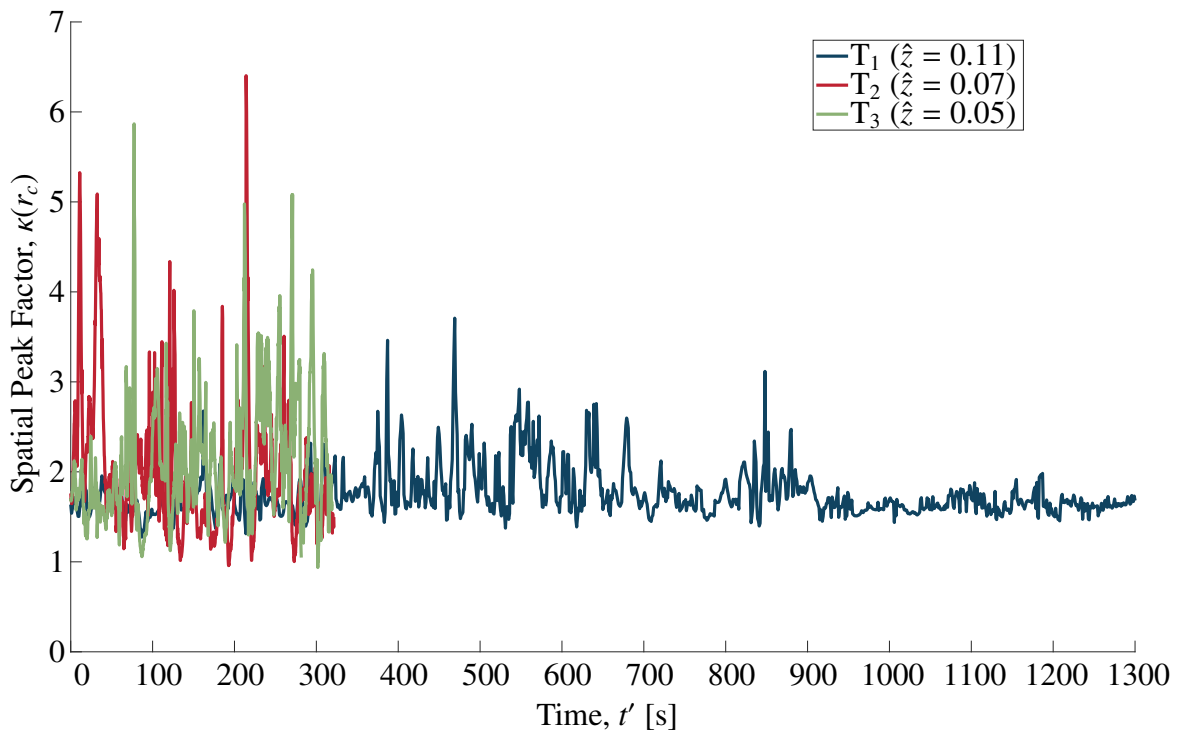


Figure 3.10: Time averaged statistics of the ratio of the peak maximum tangential velocity present in the entire tornado to the peak circumferential average tangential velocity over all heights

The tangential velocity ratio was computed as a time-averaged value for each case with a single standard deviation from the mean in both directions (as demonstrated in the previously discussed figures). Again, this resulted in a clear difference between T_1 and the other tornadoes. T_1 was approximately constant with a ratio of 1.65 ± 0.15 . T_2 and T_3 demonstrated a gradual growth with height but the former had slightly more spread, with a value of around 1.40 ± 0.25 , whereas the latter was around 1.40 ± 0.10 . The median is also shown and was consistently slightly lower than the mean value, although, in all cases, it was only less by 0.25 to 0.50. It should be expected that this would be the case as the large velocities further away from the core radius occupy less of the circumference number of points at that radius, n_r , increases and thus causes more skew to the distribution.

It can be observed that, for the two weaker tornadoes, if one were to approximate their peak instantaneous velocity based on the peak average, using a ratio of around 1.40 would be reasonable. For T_1 , a higher rated tornado for most of its lifespan, a ratio of 1.65 would be more appropriate. Although more data should be analysed before making any definitive statements about general relationships based on tornado EF rating, the present analysis method could be adopted in future studies and, perhaps, a consistent trend will emerge.

Following this analysis and discussion of the temporal distribution of instantaneous to average velocities, the spatial-peak factor was computed next (see Fig. 3.11).



(a)

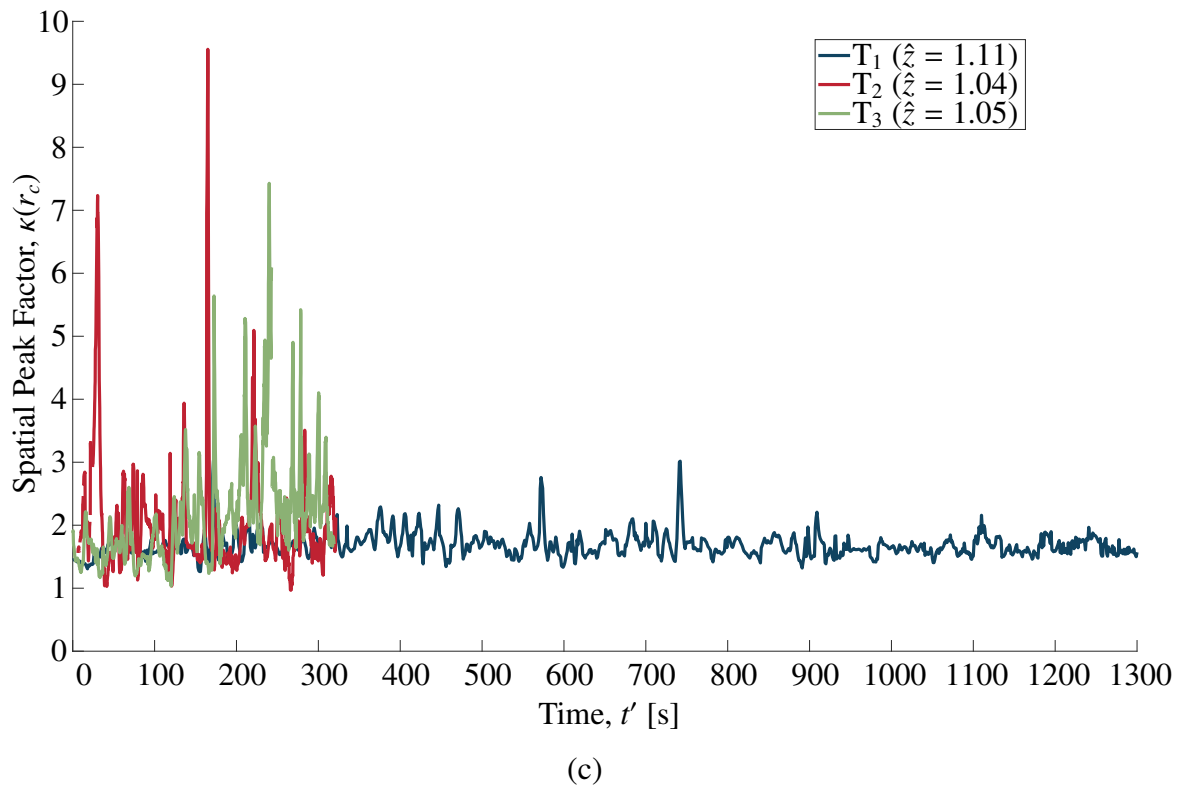
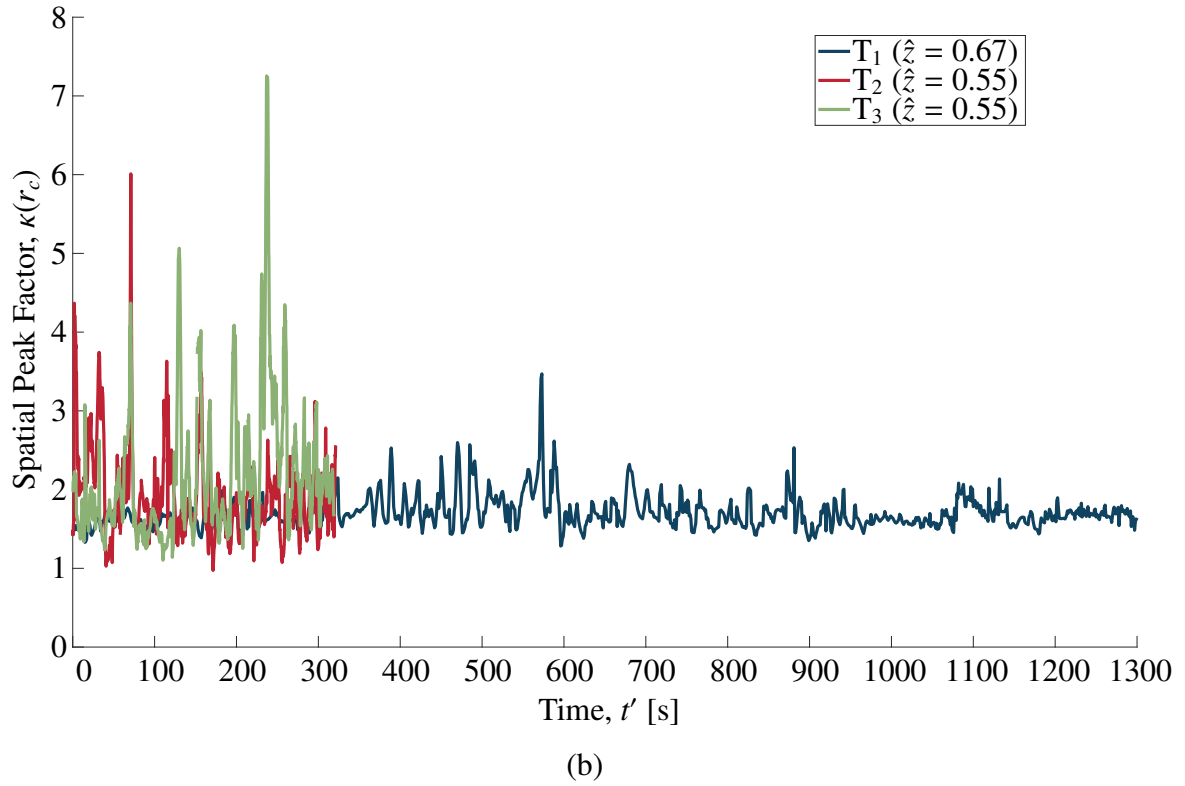


Figure 3.11: The variation of the spatial peak factor, κ , (see Eq. 3.15) with time at $\hat{z} \approx$ (a) 0.00, (b) 0.50, and (c) 1.00

Although there was a great deal of fluctuation in κ for T_2 and T_3 over their short lifespans, it was observed that the values for all three tornadoes centred on approximately 1.75–2.00. The different heights selected did not significantly modify this result. This was further corroborated when, again, the relationship of the variation of these values was taken with respect to height by temporally averaging the data (Fig. 3.12).

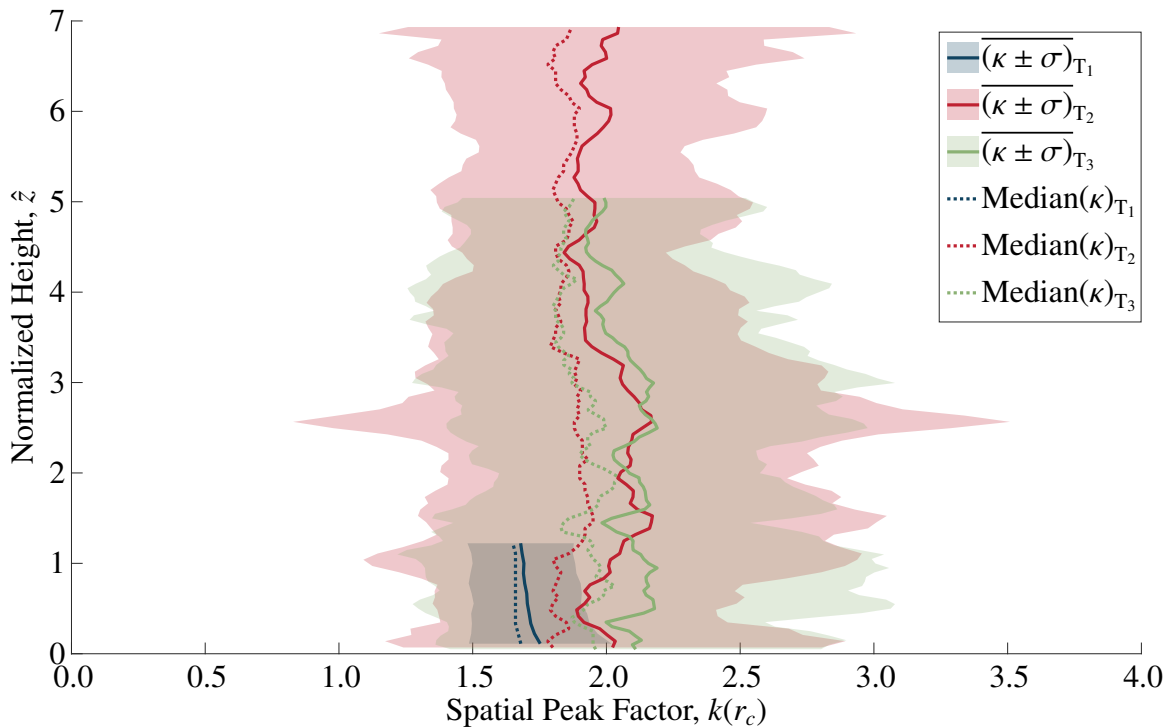


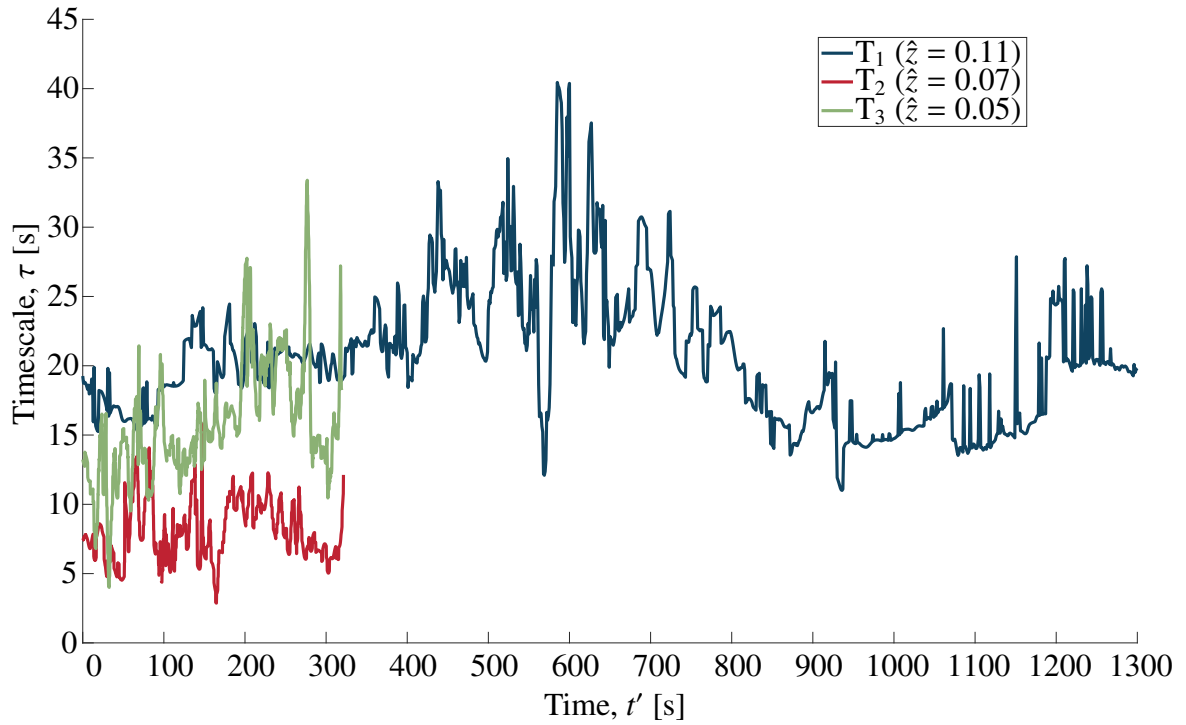
Figure 3.12: Time averaged statistics of the spatial peak factor over all heights

The value of κ was observed to have a temporal mean of approximately 1.75 with a standard deviation of 0.25 for all heights and for T_2 and T_3 the mean and variation were 2.00 ± 0.75 near the ground and approximately 1.90 ± 0.50 at their maximum heights. The median line is also shown for each case, and as was found previously for the velocity ratio, it appeared just below the mean by no more than 0.25. The minimal distance between the mean and the median occur just as in the previous case, large velocity values that are outliers on a given radius.

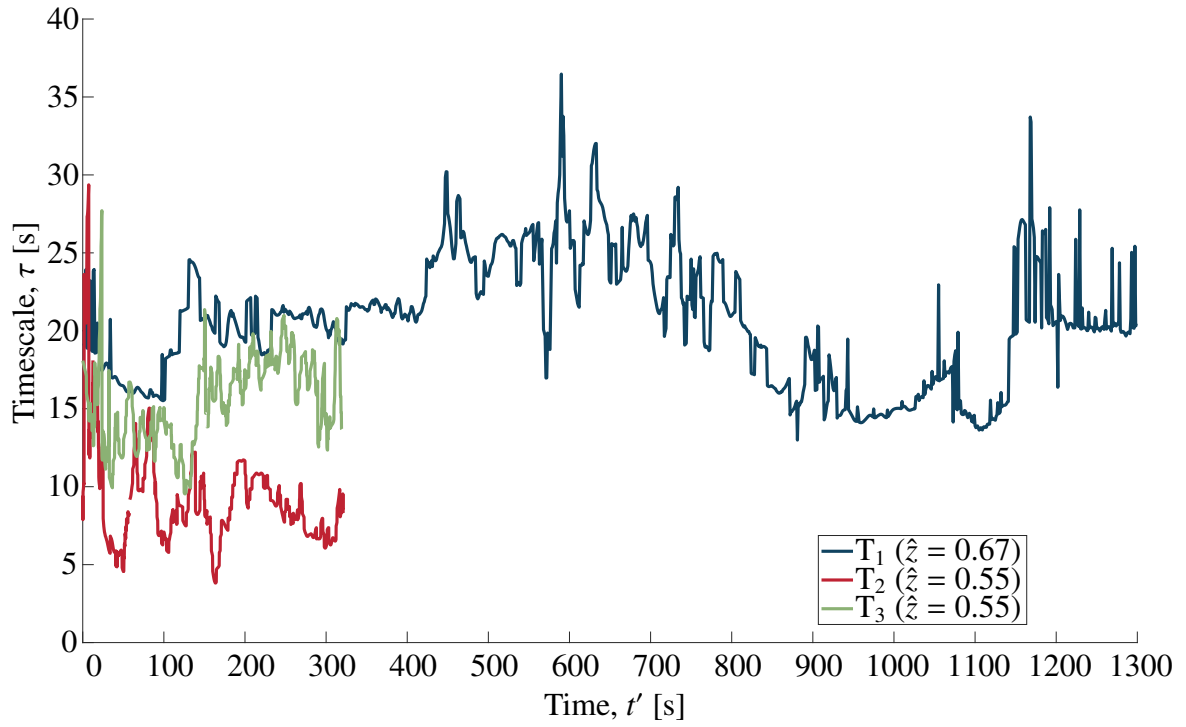
In a conventional tornado-like vortex analysis study, the value here would be zero since the maximum velocity and the peak averaged velocity would be identical. In this case, it is

clear that the averaged value is consistently less than the peak.

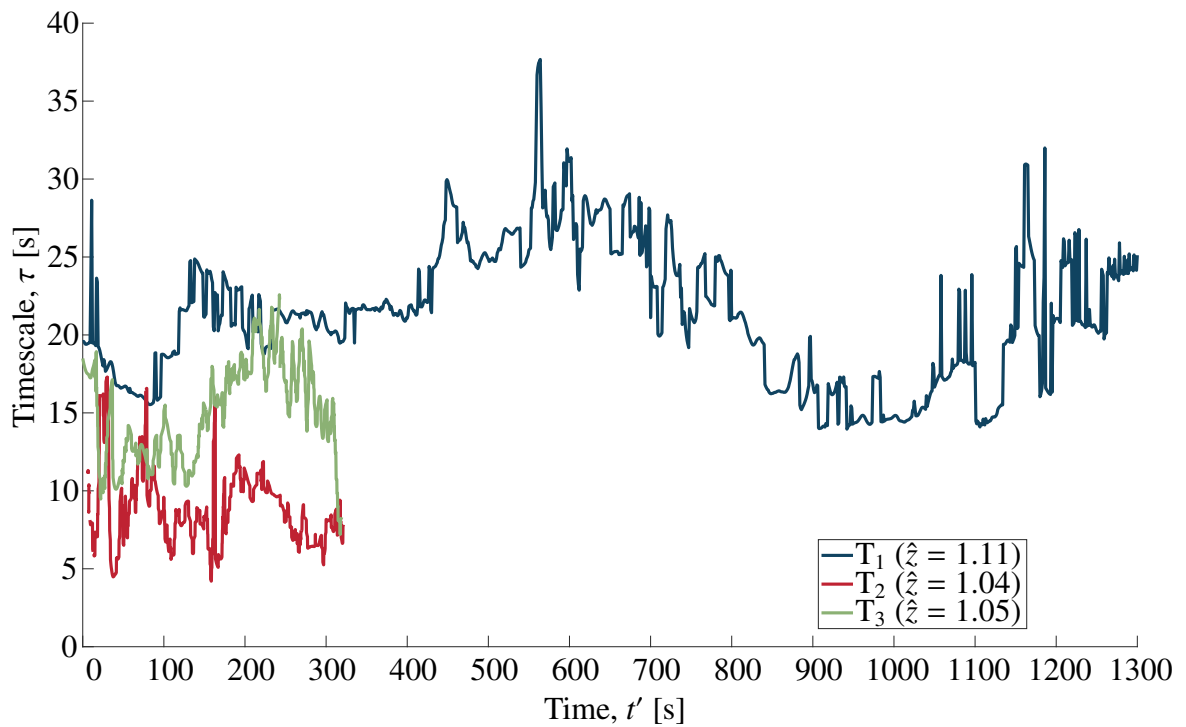
To better understand the dynamics of the tornado and how the fluctuations might be related to the larger scale motions, a potential timescale for each tornado was computed and the result can be seen for the representative height layers of each dataset in Fig. 3.13.



(a)



(b)



(c)

Figure 3.13: A visualisation of the change over time of the defined timescale, τ , at $\hat{z} =$ (a) 0.00, (b) 0.50, and (c) 1.00

The values fluctuated in each case but were consistent for the most part, with a value of around 20.0, 7.5, and 15.0 s in T_1 , T_2 , and T_3 , respectively. T_2 demonstrated a large fluctuation near the beginning of the window of analysis, but only for the second and third representative heights. In Ward [43], a “bulging” of the core radius was observed to move upwards through the tornado before dissipation. However, this outlier was likely caused by the wind-speed dominance of another vortex in the vicinity of the tornado at that particular timestep. The detection and elimination of such outliers was not possible with the currently employed definition for a tornado vortex and detection methodology and as such can result in the overestimation of the spread of τ . Therefore, the reader is advised to take caution in this result that defines the timescale of T_2 . Considering the time average of these quantities at each height mitigated the effects of these outliers on the results (Fig. 3.14).

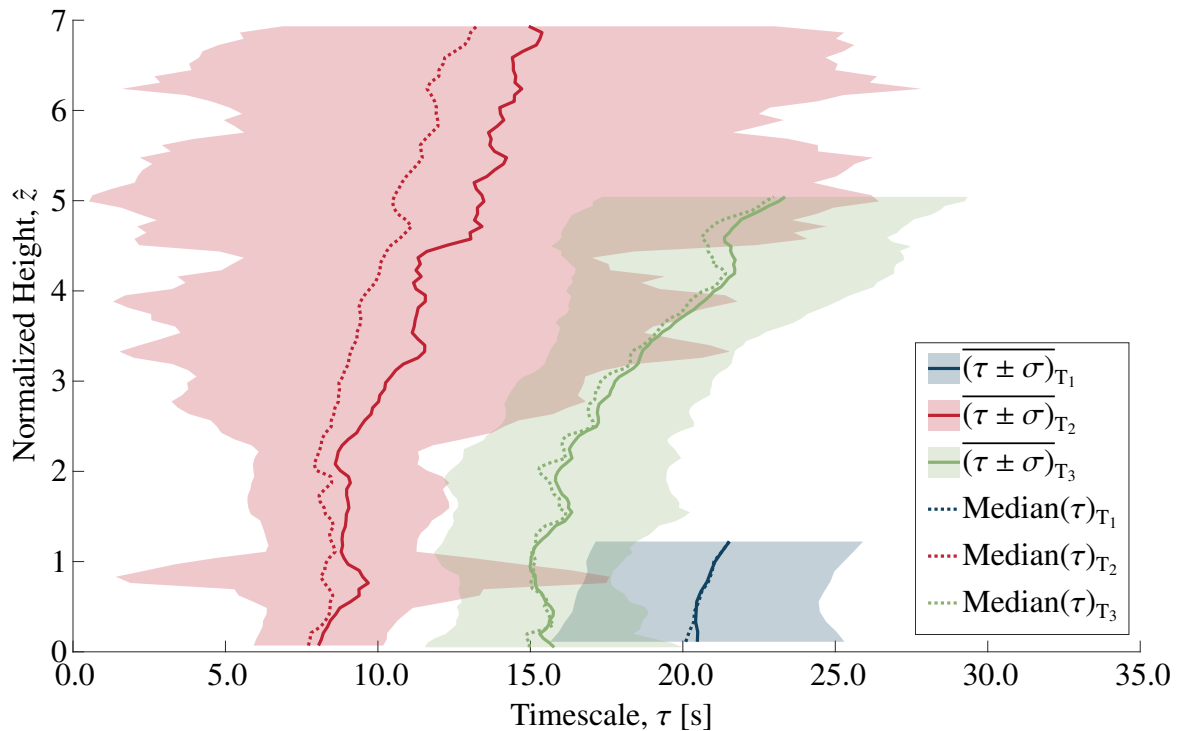


Figure 3.14: Time averaged statistics of a timescale computed for each height of each tornado dataset

T_1 and T_3 demonstrated relatively uniform spreads of τ values for all layers, with a slight increase with height. Overall, T_1 had a mean value with 1 standard deviation of variation

of approximately 20.0 ± 5.0 s and T_3 was around 15.0 ± 5.0 s up to 20.0 ± 7.5 s. The median in each case was very close to the mean value in each case. This indicates an even distribution of core radii about the mean value. T_2 , however, had a mean value of 7.5–15 s with a standard deviation of 2.5–12.5 s. The median value was also skewed lower than the mean, likely still an artefact of the detection process with regards to one (or more) vortices interacting. In general, these values provided an indication of a timescale that was associated with the mean vortex motion. These values act as the upper limit for the subsequent turbulence computations with regards to selecting the value of the temporal smoothing window index size, n_w .

The first part of the turbulence analysis considers the TKE for the data over the three time-blocks, $t_b = 1.0, 2.5,$ and 5.0 minutes, as described in Sect. 3.2.7, for the three representative heights, $\hat{z} \approx 0.0, 0.5,$ and 1.0 , and radii $\hat{r} \approx 0.33, 1.00,$ and 3.00 (see the schematic in Fig. 3.1 for a similar example). There was some variation in the exact \hat{z} and \hat{r} as dictated by the grid spacing and the fluctuation of r_c in time and over height, so a mean value for r_c was computed at each timestep so that each positional ratio was only a function of time. Much higher radii might have been chosen, however, by limiting the range of radii it was ensured that all datasets could be compared for the entire time series. Additionally, these radii represent three distinct regions of the tornadoes: within the core radius, on the core radius, and beyond the core radius. Selecting locations at greater distances from the vortex centre, especially for T_2 and T_3 would only result in observing the effects of the other vortices or atmospheric phenomena present in the domain. The aforementioned \hat{z} and \hat{r} ratios were duplicated for each of the main cardinal points about the tornado centre to provide information about the velocity fluctuations present all around the vortex. This meant that for each point, there were 42, 132, and 282 timesteps available for analysis of T_1 and 202, 652, and 1402 for the other two datasets in each of the time-blocks, t_b . Although it would have been better to quantify these turbulence results with an uncertainty, there were many factors present in the construction of these data. As such, only a relative uncertainty can be deter-

mined at this time, such that the average values presented here should decrease and steadily approach the true average value as a function of the inverse square root of the number of samples [81]. Furthermore, the statistical accuracy of these computations was limited by the short duration of the tornadoes (e.g., approximately 5 mins). More significant statistics would be obtained for longer events (e.g., of the order of 60 mins)⁴.

The analysis of TKE and TI was taken with respect to all of the velocity components because, firstly, the velocity residual, $u_i - (\overline{u_i})_{t_b}$, was found to be approximately equal across each of the components and with position relative to the centre of the vortex. Examining the RMS and the variance of these residuals was important for determining the total energy of the fluctuations filtered out by the time-block analyses and how much of the low frequency fluctuations were being removed in the windowing process of size n_w s. The RMS and variance of the radial velocity residual were often much larger with increasing radius but did not noticeably change with height. The tangential velocity residual was consistent in the two inner radii but much smaller further away from the vortex centre. Furthermore, it decreased significantly at the uppermost height in comparison to the ground level. The vertical velocity residual was smaller at the ground level and much greater higher up and also largest inside the core radius. The variance, as a proxy for the total kinetic energy contained in each of the velocity components, was found to be marginally lower in the vertical velocity but this could have been an artefact of limiting the analyses to $\hat{z} \leq 1.0$, given that the vertical velocity fluctuations tend towards zero as the ground is approached.

The residuals of the signal were between 25 and 75% of the total kinetic energy across all of the positions and components, although it was usually around 50% and, even when including the windowed signal, 5–10% of the raw signal energy was missing. This was considered to be a reasonable level of error, but it should be further investigated in the future. Even so, the analyses of TKE and TI were computed for this section with all velocity

⁴ $t_b = 5$ mins was the entire time range of valid data for T₂ and T₃ so there was no range to display

components together as any inconsistency across components and positions was nearly negligible. Therefore, the TKE and TI of the overall velocity component residual fluctuations for times smaller than τ .

Once n_w was more than approximately $\tau = 20$ s all of the various velocity signal quantities were observed to no longer be coupled to the size of the window, in agreement with the timescale analyses, and thus this value was used to temporally smooth all of the subsequent analyses. The results of not performing this windowing for each of the following three analyses can be found in Appendix C.

Before computing the TKE and TI values, it was desired to understand the relative ratios of grid-scale and SGS TKE to the total TKE (Fig. 3.15). It is important to note that T_1 is excluded because there were no SGS data and as such had only grid-scale data. Further, for \hat{z}_1 the SGS TKE were, due to limitations of the parent simulation model near the ground surface, essentially negligible. Focusing then on \hat{z}_2 and \hat{z}_3 , it is clear that the proportion of SGS TKE in the total TKE decreased with an increasing time-block length and radial location. The proportion of SGS TKE was also generally larger for T_2 than for T_3 . Overall, it can be seen that the SGS TKE made up approximately 10–30% of the total TKE with most of the values around 20%. The SGS TKE never made up more than 40% of the total TKE and this is to be expected given that, for the tornadoes analysed, r_c is of the order of 100 m (giving a diameter of 200 m) so that grid-scale TKE is computed for motions of 10–200 m in scale and the SGS TKE captured the remaining motions below 10 m in scale.

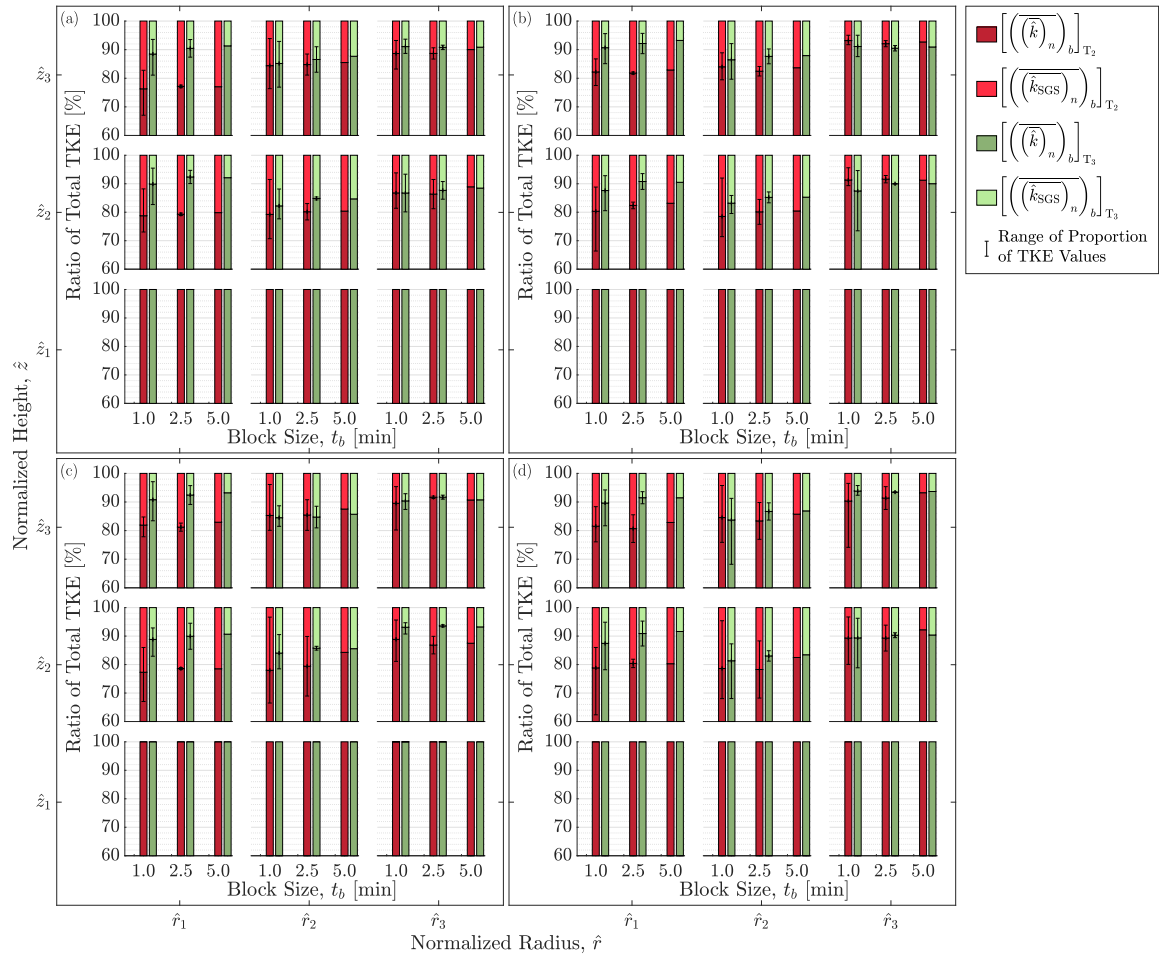


Figure 3.15: Temporally smoothed grid-scale and SGS TKE as a proportion of the total TKE averaged over different time-block lengths and shown at various vertical and radial locations surrounding the vortex at (a) north, (b) east, (c) south, and (d) west of the tornado centre

This is much more convenient to refer to when comparing between tornadoes as compared to contour plot slices such as in Lewellen *et al.*'s (1997) work [82]. In which a ratio of the SGS to grid-scale TKE is of the order of 10%, a comparable value to what was found here. The total TKE normalized by the temporal mean of the tangential velocity at all of the same locations were then computed with the results shown in Fig. 3.15.

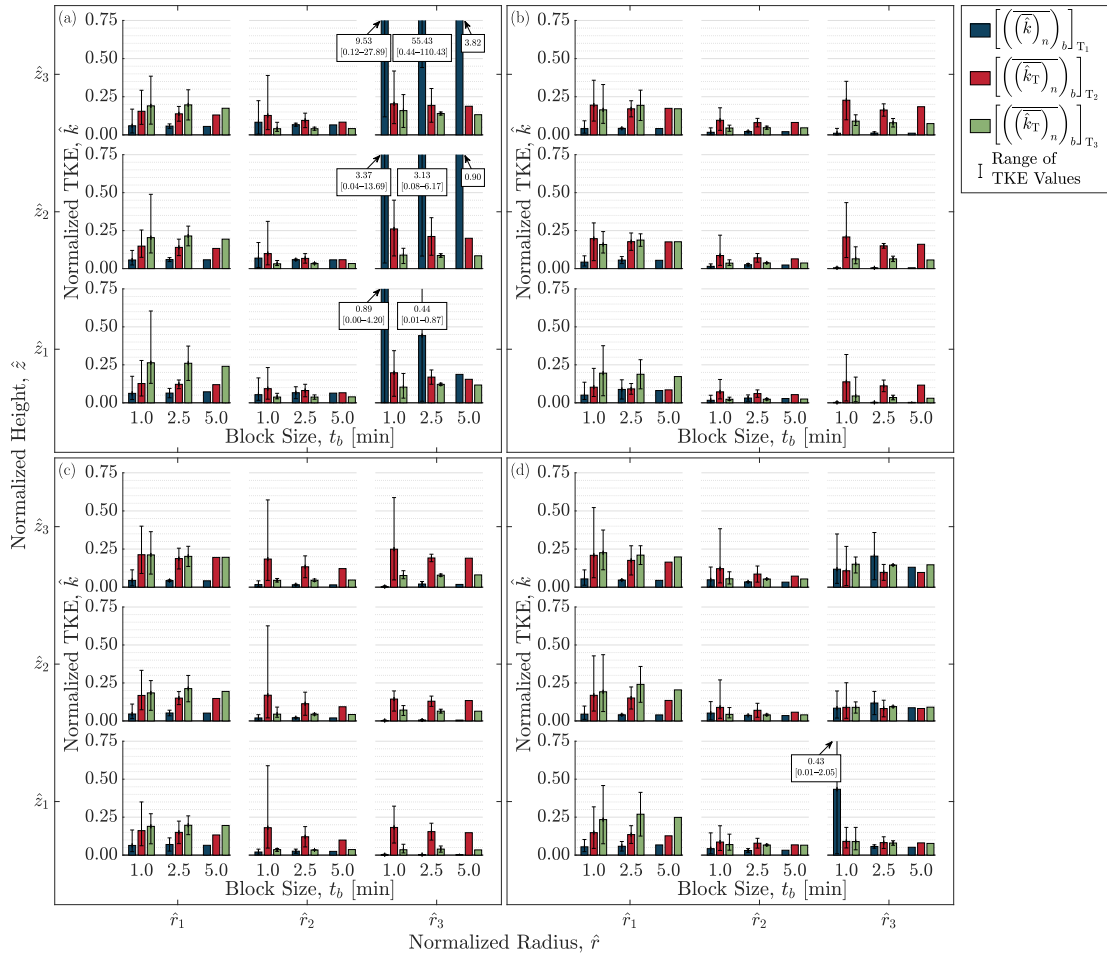


Figure 3.16: Temporally smoothed statistics of the normalized total TKE, \hat{k}_T , averaged over different time-block lengths and shown at various vertical and radial locations surrounding the vortex at (a) north, (b) east, (c) south, and (d) west of the tornado centre

The radial and vertical velocity components may also be used in the normalization of these values and this may assist in reducing the outliers to a more reasonable quantity. That is because, here, the tangential velocity component was significantly lower than the radial and vertical components further away from the core and higher off of the ground. Since this issue was mostly limited to T_1 , it was decided to proceed with just using u_t as the normalizing quantity as the other two datasets were the focus of the turbulence analysis.

The TKE was lowest at \hat{r}_2 , but the other two radial locations appear to be mostly equivalent. However, the values at \hat{r}_1 did not vary much with the Cardinal location whereas those at

\hat{r}_3 did. In particular, T_1 was extremely large north of the vortex, but this was an artifact of the tornado motion relative to the ground resulting in very small u_t values there. That is not to say that the asymmetry of the vortex should not be relevant, but that for the analysis of these small-scale fluctuations it is not decidedly critical to understanding the TKE. The normalized total TKE for T_1 was, on average, approximately 0.05 and up to 0.20, with the exception of the \hat{r}_3 north of the vortex. Caution should be applied to analysing T_1 here due to the missing SGS data but also the larger grid-scale size of 30 m in comparison to the other two datasets at 10 m. This means that the motions under 30 m remain unaccounted for and should then be more significant than for the other two datasets. For T_2 and T_3 , this value was more consistent, with an average of between 0.05 and 0.25 and no extreme larger than 0.70. The total TKE was usually highest for $t_b = 1.0$ min and lowest for 5.0 min, as one might expect since the fluctuations get smoothed out. Additionally, \hat{k}_T demonstrated moderate growth with height, but this is again a result of the decrease of u_t relative to the other components with height. Though challenging to read an exact value that was comparable to the results here, in Lewellen *et al* (1997) an approximate total TKE normalized by an average u_t was determined to be between 0.10 and 0.30, which agrees with the values found in this work reasonably well [82]. Finishing the analysis of these turbulent fluctuation quantities, the TI was then computed and can be seen in Fig. 3.17.

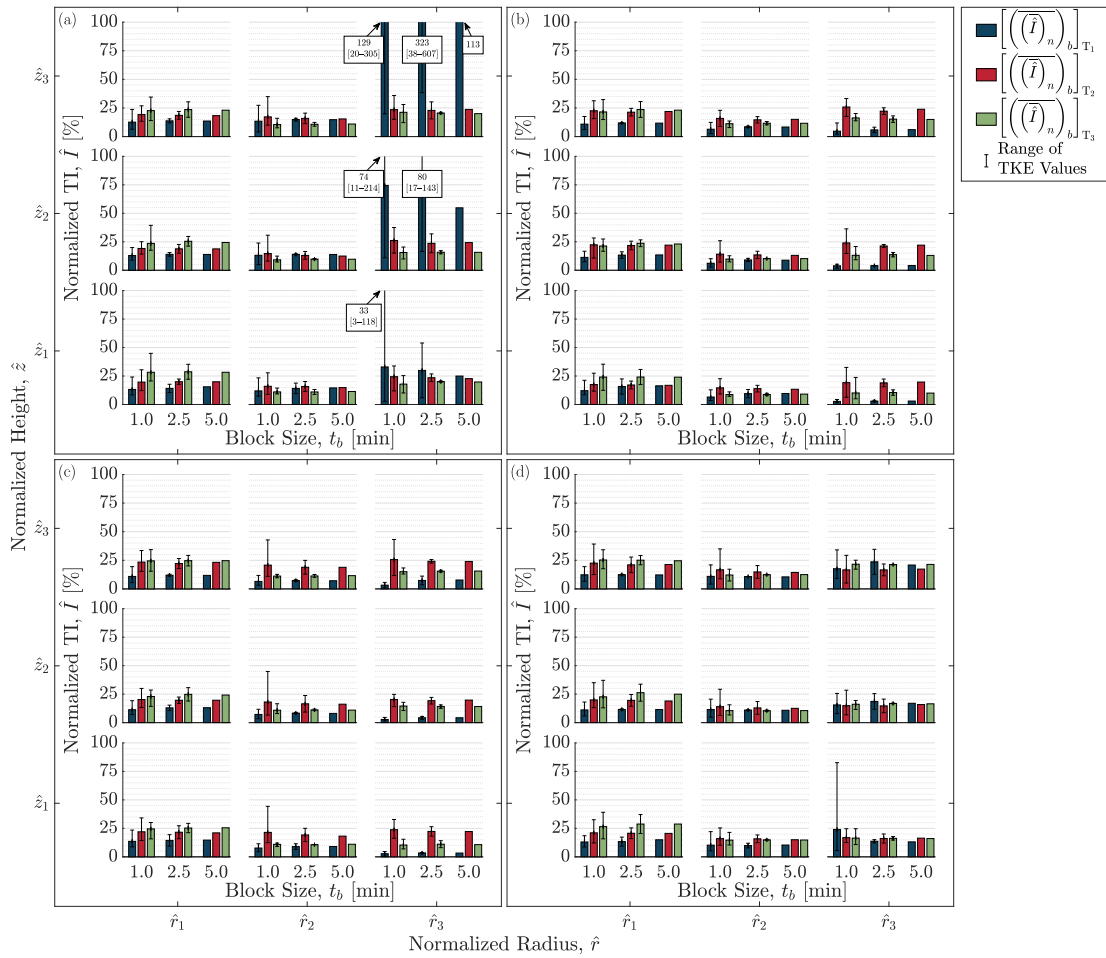


Figure 3.17: Temporally-smoothed statistics of the TI across different time-block lengths and positions, vertically and radially, surrounding the vortex at (a) north, (b) east, (c) south, and (d) west of the tornado centre

As was seen for the normalized total TKE, there were several instances of T_1 exceeding a reasonable value and thus these values were clipped and are indicated by a text-box instead. The values in each tornado are mostly equal for each position and time-block length, however, there was a slight but clear decrease in TI at \hat{r}_2 . The difference in values between \hat{r}_1 and \hat{r}_3 were small but in some cases one was larger than the other and in others the opposite was true without any clear pattern indicating the cause. There was also no clear dependence of TI on height or the Cardinal location. Similarly to the TKE, perhaps the TI can be taken to be axisymmetric but the results here are not sufficient to conclude

this for all tornadoes. In general, the TI could be said to be of the order of 5–15% for T_1 (with the exception of the \hat{r}_3 cases north of the vortex), 15–20% for T_2 (although most values appear to be clustered closer to 20%), and 10–25% for T_3 .

Finally, by analysing the velocity from the ground at a fixed location in time (in motion relative to the tornadoes), a vertical profile was produced for all times in which the towers remained within the available domain. The velocities were smoothed by the same windowing parameter, n_w , that was found for each tornado previously (Fig. 3.18).

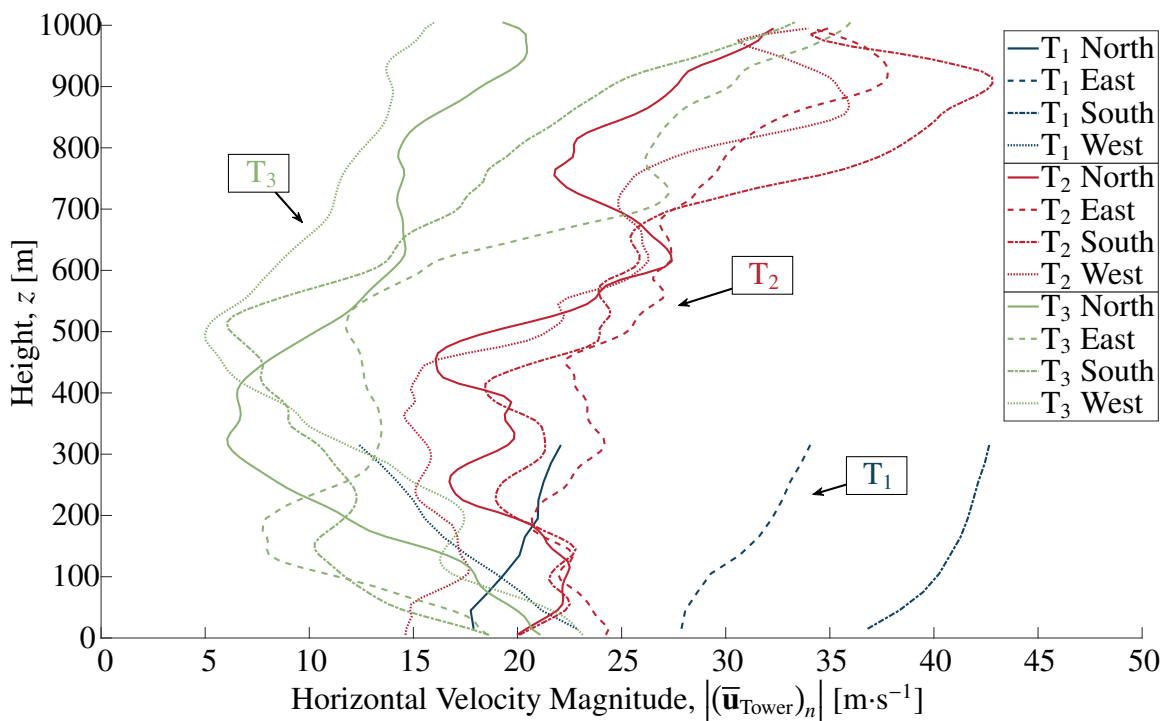


Figure 3.18: Horizontal velocity magnitude from sensors on a hypothetical tower at $r(t'_{1/2}, z_i = 1) = r_c$

For clarity, only the timestep, $t = t'_{1/2}$, is shown and not the spread of values. There was little consistency to be found in any of the cases and the velocity near the ground did not approach zero, in part due to the free-slip condition imposed on the ground boundary. However, T_2 and T_3 did, for the most part, have lower velocity values closer to the ground than T_1 . In all three cases, it could be approximately determined that the velocity was increasing with height, except for the point positioned to the West in T_1 that appeared to

display the opposite trend and decreased with height. Additionally, it was clear that the horizontal velocity vector magnitude about the centre of the vortex was not symmetric and a direct cause of the lack of consistency between towers as well as through time. The change in time would be caused by the approach and retreat of each tower relative to the vortex centre. Furthermore, this type of analysis is complicated by the inability at the moment to filter out any other vortices that may be present in the wind-field. The change in the velocity with the vertical position indicates that, in general, the vortices had higher velocities on the south and east sides of the circumference and so must be moving to the northeast. Furthermore, the horizontal layers of the vortex were moving more rapidly from the adjacent layers below once above 100–200 m from the ground.

3.4 Conclusions

This chapter demonstrates that, in wind-engineering, if the realistic characteristics of meteorologically accurate simulated tornadoes are neglected, this leads to potential dangerous fluctuations in the tangential wind profile being neglected. Analysis of three tornadoes spawned from spatially and temporally highly-resolved, supercell thunderstorm simulations demonstrated that, for these EF 2–3 tornadic events, a peak gust wind velocity of 1.75 times the conventional peak circumferential average tangential velocity is entirely possible and can be consistently maintained throughout the tornado lifetime. Additionally, such strong gusts can also be expected to occur outside of the edge of the tornado core, indicating that the region of damaging winds could be 125% of that distance or further. However, more work is needed to separate out the effects of surrounding vortices in the datasets used in this work, especially the more complex T_2 and T_3 tornadoes. The spatial-peak factor, conventionally a value of 0, was shown to reach beyond 2 and often up to 3 so that, for any given time within a tornado, there is a wide spread of velocities found above and below the average value.

Equipped with the knowledge that there is a spatial fluctuation to be expected within a tornado, it is also important to understand how it may fluctuate in time. In this study it was found that, using a timescale for the mean tornado motion, the tornado core grows with height. The value for this timescale, τ , was between 10–20 seconds across the three datasets and was used to filter larger-scale fluctuations from the data; leaving behind only the higher frequencies for turbulent analysis. The filtering meant that approximately 50% of the total energy fluctuations were attributed to residual value of the velocity components. After these checks to validate the window sizing, a spread of the average TKE (when normalized by the square of the tangential velocity) of between approximately 0.05 and 0.25 with an average TI (similarly normalized) of 10 to 25% across all of the tornadoes was observed. These values do not display much variation around the vortex core but including a range for even a small amount may be critical in understanding complex tornadoes. It would be, however, prudent to obtain longer time series for these types of analyses (where possible) or more datasets to compare against to improve the statistical uncertainty of these results. Then, a confidence interval may be provided rather than a simple range of values. Finally, an analysis of the velocity profile with height was performed. This analysis was limited by the constant grid spacing that, although is very highly spatially resolved for a meteorological simulation, was insufficient to make any conclusions about near the ground level region. The profile in each case did not demonstrate the tornado horizontal velocity approaching zero as $z \rightarrow 0$. However, it was clear that the horizontal velocity magnitude did vary significantly with height, and tended to increase from ground to the domain limit by as much as 200%. Therefore, it should be expected that the tornadoes are tilting significantly after about 100–200 m above the ground, as is observed in nature.

In conclusion, tornadoes, as analysed presently in wind-engineering, are artificially prevented from demonstrating significant asymmetry in the horizontal vortex profile. Careful analyses developed in this study show the extent of the deviations of gusting winds from the average profile and also significant tilting from the vertical axis. Further work is required

to understand the impact of the ground boundary conditions on the velocity magnitude as height approaches zero. However, this study sets the groundwork for future analysis of the spatial and temporal fluctuations present in the current research. This is true even for artificially symmetric and constrained tornadoes, which should not simply be temporally and spatially averaged.

References

- [1] M. K. Tippett and J. E. Cohen, “Tornado outbreak variability follows Taylor’s power law of fluctuation scaling and increases dramatically with severity,” *Nature Communications*, vol. 7, 2016.
- [2] S. M. Verbout, H. E. Brooks, L. M. Leslie, and D. M. Schultz, “Evolution of the U.S. tornado database: 1954–2003,” *Weather and Forecasting*, vol. 21, no. 1, pp. 86–93, 2006.
- [3] National Weather Service (NWS), “Storm prediction center maps, graphics, and data page,” Mar. 2023. Accessed: Mar. 28, 2023. [Online.] Available: <https://www.spc.noaa.gov/wcm/>
- [4] C. A. Doswell, A. R. Moller, and H. E. Brooks, “Storm spotting and public awareness since the first tornado forecasts of 1948,” *Weather and Forecasting*, vol. 14, no. 4, pp. 544–557, 1999.
- [5] H. E. Brooks and J. Correia, “Long-term performance metrics for National Weather Service tornado warnings,” *Weather and Forecasting*, vol. 33, no. 6, pp. 1501–1511, 2018.
- [6] W. S. Ashley, A. M. Haberlie, and V. A. Gensini, “The future of supercells in the United States,” *Bulletin of the American Meteorological Society*, vol. 104, no. 1, pp. E1–E21, 2023.
- [7] D. Arndt, J. Crouch, J. Blunden, and R. Lindsey, “2022 U.S. billion-dollar weather and climate disasters in historical context,” National Oceanic and Atmospheric Administration (NOAA), Jan. 2023. Accessed: Apr. 2, 2023. [Online.] Available: <https://www.climate.gov/news-features/blogs/2022-us-billion-dollar-weather-and-climate-disasters-historical-context>

- [8] A. B. Smith and R. W. Katz, “U.S. billion-dollar weather and climate disasters: data sources, trends, accuracy and biases,” *Natural Hazards*, vol. 67, no. 2, pp. 387–410, 2013.
- [9] A. B. Smith, “U.S. billion-dollar weather and climate disasters, 1980 - present (NCEI accession 0209268),” National Centers for Environmental Information (NCEI), 2020. Accessed: Apr. 4, 2023. [Online.] Available: <https://www.ncei.noaa.gov/archive/accession/0209268>
- [10] L. R. Lemon and C. A. Doswell, “Severe thunderstorm evolution and mesocyclone structure as related to tornadogenesis,” *Monthly Weather Review*, vol. 107, no. 9, pp. 1184–1197, 1979.
- [11] L. Orf, R. Wilhelmson, B. Lee, C. Finley, and A. Houston, “Evolution of a long-track violent tornado within a simulated supercell,” *Bulletin of the American Meteorological Society*, vol. 98, no. 1, pp. 45–68, 2017.
- [12] L. Orf, “A violently tornadic supercell thunderstorm simulation spanning a quarter-trillion grid volumes: Computational challenges, I/O framework, and visualizations of tornadogenesis,” *Atmosphere*, vol. 10, no. 10, p. 578, 2019.
- [13] R. A. Maddox, “Mesoscale convective complexes,” *Bulletin of the American Meteorological Society*, vol. 61, no. 11, pp. 1374–1387, 1980.
- [14] P. M. Markowski, T. P. Hatlee, and Y. P. Richardson, “Tornadogenesis in the 12 May 2010 supercell thunderstorm intercepted by VORTEX2 near Clinton, Oklahoma,” *Monthly Weather Review*, vol. 146, no. 11, pp. 3623–3650, 2018.
- [15] C. K. Potvin, B. T. Gallo, A. E. Reinhart, B. Roberts, P. S. Skinner, R. A. Sobash, K. A. Wilson, K. C. Britt, C. Broyles, M. L. Flora *et al.*, “An iterative storm segmentation and classification algorithm for convection-allowing models and gridded

- radar analyses,” *Journal of Atmospheric and Oceanic Technology*, vol. 39, no. 7, pp. 999–1013, 2022.
- [16] J. Yang, M. Astitha, L. D. Monache, and S. Alessandrini, “An analog technique to improve storm wind speed prediction using a dual NWP model approach,” *Monthly Weather Review*, vol. 146, no. 12, pp. 4057–4077, 2018.
- [17] H. B. Bluestein, K. J. Thiem, J. C. Snyder, and J. B. Houser, “Tornadogenesis and early tornado evolution in the El Reno, Oklahoma, supercell on 31 May 2013,” *Monthly Weather Review*, vol. 147, no. 6, pp. 2045–2066, 2019.
- [18] N. Snook, M. Xue, and Y. Jung, “Tornado-resolving ensemble and probabilistic predictions of the 20 May 2013 Newcastle–Moore EF5 tornado,” *Monthly Weather Review*, vol. 147, no. 4, pp. 1215–1235, 2019.
- [19] J. Wurman, D. Dowell, Y. Richardson, P. Markowski, E. Rasmussen, D. Burgess, L. Wicker, and H. B. Bluestein, “The second verification of the origins of rotation in tornadoes experiment: VORTEX2,” *Bulletin of the American Meteorological Society*, vol. 93, no. 8, pp. 1147–1170, 2012.
- [20] J. A. Brotzge, S. E. Nelson, R. L. Thompson, and B. T. Smith, “Tornado probability of detection and lead time as a function of convective mode and environmental parameters,” *Weather and Forecasting*, vol. 28, no. 5, pp. 1261–1276, 2013.
- [21] E. Savory, G. A. Parke, M. Zeinoddini, N. Toy, and P. Disney, “Modelling of tornado and microburst-induced wind loading and failure of a lattice transmission tower,” *Engineering Structures*, vol. 23, no. 4, pp. 365–375, 2001.
- [22] F. L. Haan, V. K. Balaramudu, and P. P. Sarkar, “Tornado-induced wind loads on a low-rise building,” *Journal of Structural Engineering*, vol. 136, no. 1, pp. 106–116, 2010.

- [23] A. Elshaer, H. Aboshosha, G. Bitsuamlak, A. El Damatty, and A. Dagneu, “LES evaluation of wind-induced responses for an isolated and a surrounded tall building,” *Engineering Structures*, vol. 115, pp. 179–195, 2016.
- [24] W. Rankine, *Motions of fluids—hydrodynamics*. Charles Griffin and Company, London, 1877, pp. 574–577.
- [25] J. Burgers, “A mathematical model illustrating the theory of turbulence,” vol. 1, pp. 171–199, 1948.
- [26] R. D. Sullivan, “A two-cell vortex solution of the Navier-Stokes equations,” *Journal of the Aerospace Sciences*, vol. 26, no. 11, pp. 767–768, 1959.
- [27] H. L. Kuo, “Axisymmetric flows in the boundary layer of a maintained vortex,” *Journal of Atmospheric Sciences*, vol. 28, no. 1, pp. 20–41, 1971.
- [28] Y.-K. Wen, “Dynamic tornadic wind loads on tall buildings,” *ASCE Journal of the Structural Division*, vol. 101, no. 1, pp. 169–185, 1975.
- [29] Y. Wen and A. Ang, “Tornado risk and wind effect on structures,” in *Proceedings of the Fourth International Conference on Wind Effects on Buildings and Structures, London, U.K., 1975*, pp. 63–74.
- [30] F. W. Leslie and J. T. Snow, “Sullivan’s two-celled vortex,” *AIAA Journal*, vol. 18, no. 10, pp. 1272–1274, 1980.
- [31] M. C. Jischke and M. Parang, “Properties of simulated tornado-like vortices,” *Journal of Atmospheric Sciences*, vol. 31, no. 2, pp. 506–512, 1974.
- [32] Y. Mitsuta and N. Monji, “Development of a laboratory simulator for small scale atmospheric vortices,” *Natural Disaster Science*, vol. 6, no. 1, pp. 43–54, 1984.

- [33] A. R. Mishra, D. L. James, and C. W. Letchford, “Physical simulation of a single-celled tornado-like vortex, part a: Flow field characterization,” *Journal of Wind Engineering and Industrial Aerodynamics*, vol. 96, no. 8, pp. 1243–1257, 2008.
- [34] F. L. Haan, P. P. Sarkar, and W. A. Gallus, “Design, construction and performance of a large tornado simulator for wind engineering applications,” *Engineering Structures*, vol. 30, no. 4, pp. 1146–1159, 2008.
- [35] P. Hashemi Tari, R. Gurka, and H. Hangan, “Experimental investigation of tornado-like vortex dynamics with swirl ratio: The mean and turbulent flow fields,” *Journal of Wind Engineering and Industrial Aerodynamics*, vol. 98, no. 12, pp. 936–944, 2010.
- [36] W. Zhang and P. P. Sarkar, “Near-ground tornado-like vortex structure resolved by particle image velocimetry (PIV),” *Experiments in Fluids*, vol. 52, pp. 479–493, 2012.
- [37] M. Refan, H. Hangan, and J. Wurman, “Reproducing tornadoes in laboratory using proper scaling,” *Journal of Wind Engineering and Industrial Aerodynamics*, vol. 135, pp. 136–148, 2014.
- [38] M. Refan and H. Hangan, “Characterization of tornado-like flow fields in a new model scale wind testing chamber,” *Journal of Wind Engineering and Industrial Aerodynamics*, vol. 151, pp. 107–121, 2016.
- [39] M. Refan and H. Hangan, “Near surface experimental exploration of tornado vortices,” *Journal of Wind Engineering and Industrial Aerodynamics*, vol. 175, pp. 120–135, 2018.
- [40] Z. Tang, C. Feng, L. Wu, D. Zuo, and D. L. James, “Characteristics of tornado-like vortices simulated in a large-scale ward-type simulator,” *Boundary-Layer Meteorology*, vol. 166, pp. 327–350, 2018.

- [41] Z. Tang, D. Zuo, D. James, Y. Eguchi, and Y. Hattori, “Experimental study of tornado-like loading on rectangular prisms,” *Journal of Fluids and Structures*, vol. 113, p. 103672, 2022.
- [42] S. J. Ying and C. C. Chang, “Exploratory model study of tornado-like vortex dynamics,” *Journal of Atmospheric Sciences*, vol. 27, no. 1, pp. 3–14, 1970.
- [43] N. B. Ward, “The exploration of certain features of tornado dynamics using a laboratory model,” *Journal of Atmospheric Sciences*, vol. 29, no. 6, pp. 1194–1204, 1972.
- [44] C. A. Wan and C. C. Chang, “Measurement of the velocity field in a simulated tornado-like vortex using a three-dimensional velocity probe,” *Journal of Atmospheric Sciences*, vol. 29, no. 1, pp. 116–127, 1972.
- [45] C. R. Church, J. T. Snow, and E. M. Agee, “Tornado vortex simulation at Purdue Univ.” *Bulletin of the American Meteorological Society*, vol. 58, no. 9, pp. 900–909, 1977.
- [46] G. L. Baker and C. R. Church, “Measurements of core radii and peak velocities in modeled atmospheric vortices,” *Journal of Atmospheric Sciences*, vol. 36, no. 12, pp. 2413–2424, 1979.
- [47] C. R. Church, J. T. Snow, G. L. Baker, and E. M. Agee, “Characteristics of tornado-like vortices as a function of swirl ratio: A laboratory investigation,” *Journal of Atmospheric Sciences*, vol. 36, no. 9, pp. 1755–1776, 1979.
- [48] G. L. Baker, “Boundary layer in laminar vortex flows,” Ph.D. dissertation, Purdue Univ., West Lafayette, IN, U.S.A., 1981.
- [49] C. J. Diamond and E. M. Wilkins, “Translation effects on simulated tornadoes,” *Journal of Atmospheric Sciences*, vol. 41, no. 17, pp. 2574–2580, 1984.

- [50] F. H. Harlow and L. R. Stein, “Structural analysis of tornado-like vortices,” *Journal of Atmospheric Sciences*, vol. 31, no. 8, pp. 2081–2098, 1974.
- [51] R. Rotunno, “Numerical simulation of a laboratory vortex,” *Journal of Atmospheric Sciences*, vol. 34, no. 12, pp. 1942–1956, 1977.
- [52] R. Rotunno, “A study in tornado-like vortex dynamics,” *Journal of Atmospheric Sciences*, vol. 36, no. 1, pp. 140–155, 1979.
- [53] T. Wilson and R. Rotunno, “Numerical simulation of a laminar end-wall vortex and boundary layer,” *The Physics of Fluids*, vol. 29, no. 12, pp. 3993–4005, Dec. 1986.
- [54] B. H. Fiedler, “Numerical simulation of axisymmetric tornadogenesis in forced convection,” pp. 41–48, 1993.
- [55] D. S. Nolan and B. F. Farrell, “The structure and dynamics of tornado-like vortices,” *Journal of the Atmospheric Sciences*, vol. 56, no. 16, pp. 2908–2936, 1999.
- [56] R. P. Selvam and P. C. Millett, “Computer modeling of tornado forces on a cubic building using large eddy simulation,” *Journal of the Arkansas Academy of Science*, vol. 57, no. 1, pp. 140–146, 2003.
- [57] D. S. Nolan, “A new scaling for tornado-like vortices,” *Journal of the Atmospheric Sciences*, vol. 62, no. 7, pp. 2639–2645, 2005.
- [58] A. Sengupta, F. L. Haan, P. P. Sarkar, and V. Balaramudu, “Transient loads on buildings in microburst and tornado winds,” *Journal of Wind Engineering and Industrial Aerodynamics*, vol. 96, no. 10, pp. 2173–2187, 2008.
- [59] T. Ishihara, S. Oh, and Y. Tokuyama, “Numerical study on flow fields of tornado-like vortices using the LES turbulence model,” *Journal of Wind Engineering and Industrial Aerodynamics*, vol. 99, no. 4, pp. 239–248, 2011.

- [60] T. Ishihara and Z. Liu, “Numerical study on dynamics of a tornado-like vortex with touching down by using the LES turbulence model,” *Wind and Structures*, vol. 19, no. 1, pp. 89–111, 2014.
- [61] Z. Liu and T. Ishihara, “Study of the effects of translation and roughness on tornado-like vortices by large-eddy simulations,” *Journal of Wind Engineering and Industrial Aerodynamics*, vol. 151, pp. 1–24, 2016.
- [62] Z. Liu, C. Zhang, and T. Ishihara, “Numerical study of the wind loads on a cooling tower by a stationary tornado-like vortex through LES,” *Journal of Fluids and Structures*, vol. 81, pp. 656–672, 2018.
- [63] A. Gairola and G. Bitsuamlak, “Numerical tornado modeling for common interpretation of experimental simulators,” *Journal of Wind Engineering and Industrial Aerodynamics*, vol. 186, pp. 32–48, 2019.
- [64] A. Gairola, G. T. Bitsuamlak, and H. M. Hangan, “An investigation of the effect of surface roughness on the mean flow properties of “tornado-like” vortices using large eddy simulations,” *Journal of Wind Engineering and Industrial Aerodynamics*, vol. 234, p. 105348, 2023.
- [65] H. Hangan and J. Kim, “Swirl ratio effects on tornado vortices in relation to the Fujita scale,” *Wind and Structures*, vol. 11, no. 4, pp. 291–302, 2008.
- [66] L. Kuai, F. L. Haan Jr, W. A. Gallus Jr, and P. P. Sarkar, “CFD simulations of the flow field of a laboratory-simulated tornado for parameter sensitivity studies and comparison with field measurements,” *Wind and Structures*, vol. 11, no. 2, pp. 75–96, 2008.
- [67] D. Natarajan and H. Hangan, “Large eddy simulations of translation and surface roughness effects on tornado-like vortices,” *Journal of Wind Engineering and Industrial Aerodynamics*, vol. 104-106, pp. 577–584, 2012.

- [68] Z. Liu and T. Ishihara, “Numerical study of turbulent flow fields and the similarity of tornado vortices using large-eddy simulations,” *Journal of Wind Engineering and Industrial Aerodynamics*, vol. 145, pp. 42–60, 2015.
- [69] C. D. Karstens, T. M. Samaras, B. D. Lee, W. A. Gallus, and C. A. Finley, “Near-ground pressure and wind measurements in tornadoes,” *Monthly Weather Review*, vol. 138, no. 7, pp. 2570–2588, 2010.
- [70] L. Orf, “High-resolution thunderstorm modeling,” Oxford Research Encyclopedias, Jan. 2020. Accessed: Mar. 23, 2020. [Online.] Available: <https://oxfordre.com/climatescience/view/10.1093/acrefore/9780190228620.001.0001/acrefore-9780190228620-e-667>
- [71] N. Bannigan, L. Orf, and E. Savory, “Tracking the centre of asymmetric vortices using wind velocity vector data fields,” *Boundary-Layer Meteorology*, vol. 186, no. 1, pp. 1–26, 2023.
- [72] K. Y. Wong and C. L. Yip, “Identifying centers of circulating and spiraling vector field patterns and its applications,” *Pattern Recognition*, vol. 42, no. 7, pp. 1371–1387, 2009.
- [73] Y. Levy, D. Degani, and A. Seginer, “Graphical visualization of vortical flows by means of helicity,” *AIAA Journal*, vol. 28, no. 8, pp. 1347–1352, 1990.
- [74] J. Jeong and F. Hussain, “On the identification of a vortex,” *Journal of Fluid Mechanics*, vol. 285, pp. 69—94, 1995.
- [75] D. Sujudi and R. Haimes, “Identification of swirling flow in 3-D vector fields,” in *Proceedings of 12th Computational Fluid Dynamics Conference*, 1995, p. 1715.
- [76] M. Jiang, R. Machiraju, and D. S. Thompson, “A novel approach to vortex core region detection,” in *Proceedings of VisSym’02*, vol. 2, 2002, pp. 217–225.

- [77] MATLAB, “Kurtosis - algorithms,” The MathWorks, Inc. Accessed: Oct. 13, 2023.
[Online.] Available: <https://www.mathworks.com/help/stats/kurtosis.html>
- [78] MATLAB, “Skewness - algorithms,” The MathWorks, Inc. Accessed: Oct. 13, 2023.
[Online.] Available: <https://www.mathworks.com/help/stats/skewness.html>
- [79] G. H. Bryan, “The governing equations for CM1,” *National Center for Atmospheric Research Tech. Rep*, 2021.
- [80] R. Shanmugam and R. Chattamvelli, *Skewness and Kurtosis*. John Wiley & Sons, Ltd, 2015, ch. 4, pp. 89–110.
- [81] A. Wheeler and A. Ganji, *Statistical Analysis of Experimental Data*. Pearson Higher Education, London, U.K., 2010.
- [82] W. S. Lewellen, D. C. Lewellen, and R. I. Sykes, “Large-eddy simulation of a tornado’s interaction with the surface,” *Journal of the Atmospheric Sciences*, vol. 54, no. 5, pp. 581–605, 1997.

Chapter 4

4 Concluding Remarks

The methods developed in the previous chapters attempt to use remarkably well-resolved tornado simulation data to understand the extent and significance of tornado asymmetry that would not have been captured by conventional analysis techniques. In the following sections, the thesis is concluded with a summary of the major findings, their impact on the field of tornado and tornado-like vortex research, and suggestions for the direction of future research.

4.1 Summary and Conclusions

This thesis introduces new methods to account for the complexity of real-life tornadoes. Wind-field data from three different supercell thunderstorm simulations were used in this work. These simulations are full-scale meteorological studies that cover domains spanning tens of kilometres in all directions with the right conditions for natural formation of tornado vortices. This differs from traditional wind-engineering tornado-like vortex simulation where the domain artificially imposes the formation conditions of the vortex, generating an axisymmetric rotation. Results of such simulations neglect any movement of the position of the vortex or fluctuations in the velocity profiles.

It is not necessarily the case that a physical TVC can produce an entire supercell thunderstorm or a numerical modeller can get access a machine capable of generating such highly resolved yet large-scale data. Therefore, this work presents improved methods for analysing tornado-like vortices that follow the conventional averaging processes so that comparisons to previous work are not lost, but which additionally capture any realistic vortex characteristics from the raw data that are still present in the simplified models. Therefore, in cases where asymmetry, wandering, and tilting were observed (either intentionally

or by chance), these characteristics may be retained in the data, contributing to a desired level of statistical confidence in the averaged values that are currently generated in the literature.

Before investigating the asymmetric characteristics of the tornado data used in this thesis, it was necessary to fix the analyses to a coordinate system common to all tornado-like vortex studies. Typically, the variables in tornado-like vortex data are discussed on the radial axis, r , with the centre of the cylindrical coordinates at the centre position of the vortex. This position is almost always defined such that its horizontal velocity is zero, in theory. In practice, it is often approximated or assumed to be at a convenient location. In the data used in this thesis, the tornadoes were approximately followed by a sub-domain and as such were not fixed to any specific location. Additionally, the vortices' axial profile shifted and morphed significantly through time. To the best of the author's knowledge, no readily applicable solutions that could reliably and rapidly narrow in on a point location for the centreline. As a result, a novel vortex centre finding algorithm that is robust to asymmetric deviations about the centre axis was developed to ensure a consistent and reliable point was located.

The developed solution for tracking tornado centres through space and time permitted the conversion of the points surrounding the centre into a cylindrical coordinate domain. The variation of the centreline with height was handled by considering the horizontal planes as distinct from one another, rather than sliding them upon an artificial vertical axis. Velocity profiles could then be constructed on the radial line from the centre by averaging around each circumference at select heights and timesteps. This provided a basis for the proposed methods and a set of curves that could demonstrate the spatiotemporal variation of velocity about the averaged profiles. Furthermore, novel scaling factors for the excess wind above the peak of the averaged profile, the spatial variation of wind from the averaged circumference, and the duration of revolution about the vertical axis were also presented. These can

be applied to any dataset, as long as the raw signal can be accessed, to determine how close or far from axisymmetry a given vortex is.

Finally, a timescale for the mean tornado motion was developed and allowed for the analysis of the turbulent fluctuations present in the tornado data by providing the minimum cut-off for a time window of analysis. This allowed the computation of the turbulent kinetic energy, the turbulent intensity, and the vertical wind speed profile in a smoothed time window for 36 representative locations about the tornado centre. These findings demonstrate the proportion of total energy contribution to the tornado vortex by the higher frequency fluctuations and also how that varies by the position about the vortex.

4.1.1 Tracking the Centre of Asymmetric Vortices

Many algorithms and methods for detecting vortices from the literature were considered and a few select ones were applied to the tornado data used in this research. Whilst they were all able to identify a region or point(s) that could be further refined to a definite centre point, they were unable to either provide a single point or do so in a computationally efficient time frame with minimal user input. The methods requiring the least user input were those that detect the region containing a vortex, which were useful in highlighting all vortices and, in one case, were able to run faster than the proposed method (approximately 50% faster). However, the region highlighted was large in one case spanning more than eight grid points in either direction and often highlighted more than one region requiring either user intervention, which would make it unsuitable for large datasets or additional steps to refine the highlighted regions, thus losing computational efficiency. Of the region-detecting methods, only one could detect a single region in the vortex of greatest interest, but nearly 10000 times slower than the proposed method. Existing point detection methods suffered similar drawbacks to the region-detecting methods: too imprecise, requiring excessive user intervention, or too time-consuming. These methods also usually provided more than one point, requiring additional steps to reduce these points to a single location.

Only one of the tested methods could identify a single point but would do so only at indexed locations rather than the exact interpolated position desired. This method was the basis of the method presented in this thesis.

The proposed algorithm can accurately detect the strongest available vortex at a given timestep for a single horizontal layer of tornado data and suggest a position between the grid points that is likely the location of zero horizontal velocity. Additionally, the algorithm is fast enough to be applied to datasets with high spatial and temporal resolution and of extensive size and duration. This point location allows for the subsequent analyses of the data with respect to a single consistent point.

It should be noted that the algorithm was developed with the lower resolution tornado dataset, T_1 , which posed less of a challenge than the subsequent datasets (which had not yet been produced at the time of the research). These latter tornadoes were in a much more transient domain full of other vortices near to the main one and were occasionally even larger or more powerful. Thus, additional work is required to better separate out a vortex from its surroundings and keep track of multiple vortices at once. The solution applied to T_2 and T_3 was to only run the algorithm for a representative timestep, where the main vortex clearly stood out, return the starting time, t , of each dataset, and provide a “seed” location to bias the search and then prevent continual recalculation of the centre location from the entire horizontal plane. This was only required for the first timestep. This solution is only temporary, however, as it reduces the robustness and utility of the searching algorithm. Future research should focus on defining a more efficient solution to further refine the algorithm.

4.1.2 Quantifying the Asymmetry in Tornado Vortex Wind-Fields

A detailed review of the available methods to generate tornado-like vortices is provided. This background demonstrates the lack of attention to analysing beyond the spatially and

temporally averaged tangential velocity profiles. Of the analytical models, at most height is considered, but an azimuthal dependence is not incorporated. TVC and CFD tornado-like vortices demonstrated similar limitations, with most studies unable to or opting to neglect and remove the effects of asymmetry in their results. To compare the present tornado data as analysed with conventional methods versus those proposed, key parameters consistent with those in the published literature were computed. This involved calculating the range of the ratio of vertical and radial to the size of the core radius, r_c , available in each of the datasets as well as the approximate S values. Though these do not guarantee an exact match across datasets, they provide a physical non-arbitrary basis for data selection. The S , \hat{z} , and \hat{r} were approximated from the present data and in all of the reviewed literature (when possible with the available data). Since r_c varied both in time and with height, r_c was simplified by taking the mean value from ground level to the top of the domains at each timestep. All of the associated computations were performed for each timestep so that the temporal dependence was not lost.

Next, data from the literature were matched as closely as possible to the present data and a plot of the radial dependence of the normalized tangential velocity as generated. There was close agreement between each tornado dataset and at least one of the reference datasets. However, this is expected to some degree and only intended as a means of demonstrating that the current data do not substantially deviate from the previous literature. The variation about the averaged profile was then demonstrated. Selecting a sample in time in the middle of the most active period of each tornado revealed gusts of 1.75 times the conventionally averaged profile peak. Furthermore, these gusts occurred outside of the core radius, in some cases up to 25% further away. It is, however, possible that some of these results could be partially explained by external vortices present in the datasets that the current algorithm could not account for, particularly T_2 and T_3 , but it does highlight the potential risk of simplifying the tornado vortex velocity profiles down to just an averaged value.

To analyze the potential high frequency fluctuations of the velocity in the wind-field, a timescale to attempt to classify the cut-off for longer-scale fluctuation was defined. This is defined by τ , a timescale to describe the mean tornado motion. τ was between 10 and 20 s for all three datasets. This was used as reference to find an appropriate value for a window size, n_w , for smoothing the signal data for the turbulence analyses. Testing different values of n_w until the results stabilized revealed that the high frequency fluctuations occurred in under approximately less than τ s so $n_w = \tau$ s was used for smoothing the velocity values. After this filtering process, approximately 50% of the total energy remained so the remaining 50% had to be from the lower frequency motions in the tornado. The TKE was, on average, 0.05–0.25, when normalized by the square of the tangential velocity, across 36 representative points spread out and fixed in space relative to the tornado vortex centre. Similarly, the normalized TI was between 10 and 25% across all tornadoes. A caveat of these results is that they are averaged across very few time blocks because only about 5 minutes of usable data were available for T₂ and T₃. Thus, it would be desirable to acquire data from longer-lasting tornadoes, however, this is not necessarily possible and analysing more tornado vortices would be preferable to forcing vortices to stay coherent.

Finally, to simulate the effect of the tornado passing in close proximity to a structure, a set of four hypothetical towers were placed at the cardinal points about the vortex centre such that at the halfway mark in the time series, $t'_{1/2}$, they were on the circumference of the core radius. These “probe towers” were set to detect the horizontal velocity, a sum of the average of each of the horizontal velocity components, at each height. Velocity increased with height, and significantly so, up to double the ground velocity, once at the top of the tower. This demonstrates that a significant amount of tilting must be present in the vortex once more than 100–200 m off of the ground, as was found in the literature. However, this analysis also revealed a weakness in the resolution properties of the present simulations; having isogrid spacing means that the near-ground resolution is too low to adequately observe the boundary effects. However, for tornadoes to form in the supercell thunderstorm

simulations, it was necessary to use free-slip boundary conditions, as was consistently seen in full-scale tornado models in the literature. Therefore, instead of approaching zero at the ground, the velocities in all three cases remained more than $15 \text{ m}\cdot\text{s}^{-1}$. Higher resolutions in future simulations for close to the ground boundary will be required to validate the present probe analysis, but the method itself is useful in displaying tilting, translation, and asymmetry of the vortex velocity profile.

4.2 Contributions

This thesis contributes understanding to our scientific knowledge in the following ways:

- a) Detailed reviews of previous tornado-related literature including field research and simulations, have been presented, highlighting the deficiencies in acknowledgement of asymmetry present in the tornado vortex cross-sectional profile,
- b) A novel algorithm for generating the true centreline of a tornado vortex, even for highly asymmetric cases, has been developed and proven to adequately satisfy the deficiencies of pre-existing methods. This allows for a consistent definition of the centre position that can be applied generally to any tornado dataset with isometric grid spacing and executed with a high degree of computational efficiency, and
- c) A detailed set of methods to quantify the asymmetry of a tornado vortex have been laid out. This complements existing literature by providing two different methods to scale existing data, should the raw data without spatial averaging exist, with the \hat{U}_t and κ ratios. These ratios demonstrate how the tornado vortex can vary in space and therefore should be used to give a range of expected velocities for a given tornado rating for use in wind-loading experiments. A timescale is also suggested to help separate the larger-scale fluctuations of the tornado motion from its turbulent fluctuations. This was used to classify the turbulence in the TKE and TI computations. It

was found that, for these data, there is a large amount of fluctuation energy in the higher frequency motions at a given point in time; however, further analyses of different data should be performed to determine if this finding can be replicated. The probe tower analysis allows for the subsequent analysis of a building or other infrastructure in the path of a tornado and, because of the availability of the large dataset, permits analysis of the ABL profile as the tornado passes in close proximity when permitting asymmetry. The resulting data demonstrate the tilting presence of the vortex and the clear presence of the spatial deviation about a given circumference of the tornado. This indicates a clear need to account for the velocity fluctuations about the average velocity because of the inherent excess damage the additional associated wind-loading could pose to infrastructure.

4.3 Recommendations for Future Work

Through the research process, the following recommendations for potential future work have arisen:

- a) The tracking of an asymmetric vortex in a complex wind-field is possible with the proposed method but it is not exhaustive and requires further refinement to properly account for multiple vortices of varying strengths throughout their lifetimes in close proximity to one another. This would require perhaps using weighting of the identified centre locations by their distance to the previous timestep or height and continual tracking of all vortices at all timesteps, keeping the tracked locations as distinct as possible. A complication to this is that often, two or more tornadoes will coalesce to form one large vortex. Thus, more rigorous definitions for what constitutes a single vortex versus a vortex made up of multiple smaller vortices during such a transition is also required,
- b) Additional development of all of the asymmetry analyses presented here, particu-

larly the turbulence ones, to build statistical confidence with a large sample size is required. This would permit development of guidelines for tornadoes of a given EF intensity and an understanding of what range of wind speeds or other fluctuations either side of an average could be expected, and

- c) The ability to precisely track the centre of a tornado vortex produced even in full-scale simulations permits the placement of a theoretical boundary far from the event and the measurement of various parameters, such as the velocity vector around the entire surface (including the top of the domain) and comparison to conventional experimental and numerical TVC studies. Furthermore, this could be applied in reverse where the same parameters are applied at the same theoretical boundary to determine if it is possible to generate a valid vortex reminiscent of the original tornado.

Appendices

A Summary of Processing Algorithm

The centre of a vortex may be tracked with the proposed method by performing the following series of calculations on a two-dimensional, horizontal slice of data from a tornado dataset. Here, each layer is analyzed without consideration of the layers above or below (Fig. 2.6a). If not already available in the dataset, the vorticity, ω , is computed for the two-dimensional plane:

$$\omega = \nabla \times \mathbf{u} = \left(\frac{\partial u_z}{\partial y} - \frac{\partial u_y}{\partial z} \right) \hat{\mathbf{i}} + \left(\frac{\partial u_x}{\partial z} - \frac{\partial u_z}{\partial x} \right) \hat{\mathbf{j}} + \left(\frac{\partial u_y}{\partial x} - \frac{\partial u_x}{\partial y} \right) \hat{\mathbf{k}} \quad (\text{A.1})$$

where $\mathbf{u} = u_x \hat{\mathbf{i}} + u_y \hat{\mathbf{j}} + u_z \hat{\mathbf{k}}$ is the wind-field velocity vector where u_x , u_y , and u_z are the wind speeds in the x , y , and z directions, respectively, but only the $\hat{\mathbf{k}}$ remains. Then, to ensure that the analysis does not proceed with too many datapoints for each step, a scale is determined based on the resolution and dimensions of the dataset using

$$n_s = \left\lceil \frac{\min |n_x, n_y|}{c} \right\rceil \quad (\text{A.2})$$

where n_s is the scaling-factor (rounded to the nearest integer) based on the size of the dataset, n_x is the number of points in x , n_y is the number of points in y , and c is the scaling parameter (see Appendix B).

The first n_s largest curl points (Fig. 2.6b), $[x_c, y_c]$, are spatially averaged using

$$\begin{aligned} \langle x_c \rangle &= \frac{\sum_{i=1}^{n_s} x_{c,i}}{n_s} \\ \langle y_c \rangle &= \frac{\sum_{i=1}^{n_s} y_{c,i}}{n_s}. \end{aligned} \quad (\text{A.3})$$

The standard deviation, σ , of these locations, in x and y , respectively, is calculated us-

ing

$$\sigma_x = \left[\sqrt{\frac{\sum_{i=1}^{n_s} (x_{c,i} - \langle x_{c_i} \rangle)^2}{n_s - 1}} \right]$$

$$\sigma_y = \left[\sqrt{\frac{\sum_{i=1}^{n_s} (y_{c,i} - \langle y_{c_i} \rangle)^2}{n_s - 1}} \right].$$
(A.4)

The values are rounded up to accommodate that the data locations are not continuous and also to take a more conservative selection approach.

Then a desired number of standard deviations, ϕ , from the averaged position is selected such that all of the maximum curl locations outside of the bounds of the ellipse, drawn by the following curve, are excluded:

$$\frac{(x_{c,i} - \langle x_c \rangle)^2}{\sigma_x^2} + \frac{(y_{c,i} - \langle y_c \rangle)^2}{\sigma_y^2} \leq \phi.$$
(A.5)

The remaining number of positions, N , will be used as the starting point of lines drawn perpendicular to the vector direction of the datapoint at each location (Fig. 2.6c). The location of each intersection, $[x_t, y_t]$, between each line is computed using

$$x_{\text{int}} = \frac{b_j - b_i}{m_i - m_j}$$

$$y_{\text{int}} = \frac{m_j b_i - m_i b_j}{m_j - m_i}$$
(A.6)

where b is the y-intercept of the lines with the domain ordinate, m is the slope of the lines, and i and j are referring to the indexing of each line being compared such that i varies from 1 to $N - 1$ and j from $i + 1$ to N (Fig. 2.6d). The definition of N is modified to encompass only the intersections that are located within the domain range. The location of $[\langle x_t \rangle, \langle y_t \rangle]$ is then computed using

$$\langle x_{\text{int}} \rangle = \frac{\sum_{i=1}^N x_{t,i}}{N}$$

$$\langle y_{\text{int}} \rangle = \frac{\sum_{i=1}^N y_{t,i}}{N}.$$
(A.7)

The standard deviation, σ , of these locations, in x and y , respectively, is calculated using

$$\begin{aligned}\sigma_{x_{\text{int}}} &= \left[\sqrt{\frac{\sum_{i=1}^{n_s} (x_{t,i} - \langle x_{\text{int}_t} \rangle)^2}{N-1}} \right] \\ \sigma_{y_{\text{int}}} &= \left[\sqrt{\frac{\sum_{i=1}^{n_s} (y_{t,i} - \langle y_{\text{int}_t} \rangle)^2}{N-1}} \right].\end{aligned}\tag{A.8}$$

Then, a desired number of standard deviations, ϕ (its value may differ from that previously used), from the averaged position is selected such that all of the intersections outside of the bounds of the ellipse, drawn by the following curve, are excluded:

$$\frac{(x_{\text{int},i} - \langle x_{\text{int}} \rangle)^2}{\sigma_{x_{\text{int}}}^2} + \frac{(y_{\text{int},i} - \langle y_{\text{int}} \rangle)^2}{\sigma_{y_{\text{int}}}^2} \leq \phi.\tag{A.9}$$

From the remaining number of intersections, n_I , an average location is computed using

$$\begin{aligned}\langle x_I \rangle &= \frac{\sum_{i=1}^{n_I} x_{\text{int},i}}{n_I} \\ \langle y_I \rangle &= \frac{\sum_{i=1}^{n_I} y_{\text{int},i}}{n_I}.\end{aligned}\tag{A.10}$$

This final location (Fig. 2.6e) should be a valid position and also sufficiently far from the domain edge such that the subsequent centre search does not attempt to collect data from outside of the domain. In the event that this does occur, the maximum z -vorticity or minimum pressure location can be substituted in place of $[\langle x_I \rangle, \langle y_I \rangle]$.

The nearest indexed position to $[\langle x_I \rangle, \langle y_I \rangle]$ is used as the centre of a grid of size c -by- c that will be used to identify the tornado centre, defined where there is zero horizontal, storm-relative velocity. The location of minimum velocity of these points is identified and, unless it is actually the tornado centre, is then used as the centre of a new smaller grid of size three-by-three. Each possible combination of loop pattern is identified so that there can be four quadrants made up of four positions in the new grid, four quadrants of six positions in the new grid, and a large loop around the outside of the new grid (see Fig. 2.7). The

values of the signs of the vectors, $\text{sgn } \mathbf{u}$, in each loop are summated so that only the loops where this sum is equal to zero are noted as being the possible location of the tornado centre:

$$\sum_{i=1}^n \text{sgn } \mathbf{u} = 0. \quad (\text{A.11})$$

The sum of the magnitude of the tangential velocity vector, u_t , around each of these identified loops is calculated so that the one with the minimum $|u_t|$ sum is taken to be the one with the tornado centre (Fig. 2.6f):

$$\min \sum_{i=1}^n |u_{t_i}|. \quad (\text{A.12})$$

If the smaller grid is still too large, the above steps are applied iteratively until the grid is sufficiently small. If there is no path successfully identified, then the above steps are repeated but the previously identified minimum velocity vector is skipped. The number of repetitions should be limited to a total of c . Should this still fail to yield a path, the point used for the final averaged intersection location may be substituted as the tornado centre.

The four corners of the loop found above are bilinearly interpolated for the position where $u_x = 0$ and $u_y = 0$ (see Fig. A.1a), unless no path is found in which case this interpolation step is omitted. These corner points are arranged such that $x(1) = x(3)$, $x(2) = x(4)$, $y(1) = y(2)$, and $y(3) = y(4)$ and such that $x(1) < x(2)$ and $y(1) > y(3)$ (Fig. A.1b). The process of the bilinear interpolation is given for the first step in finding the interpolation of the x -position between points 1 and 2 by

$$x_{12} = x(1) + \left[\frac{0 - u_{y,1}}{u_{y,2} - u_{y,1}} \right] (x(2) - x(1)) \quad (\text{A.13})$$

and 3 and 4 by

$$x_{34} = x(3) + \left[\frac{0 - u_{y,3}}{u_{y,4} - u_{y,3}} \right] (x(4) - x(3)) \quad (\text{A.14})$$

for zero velocity in the y -direction, and then the interpolation of the y -position between points 1 and 3 by

$$y_{13} = y(1) + \left[\frac{0 - u_{x,1}}{u_{x,3} - u_{x,1}} \right] (y(3) - y(1)) \quad (\text{A.15})$$

and 2 and 4 by

$$y_{24} = y(2) + \left[\frac{0 - u_{x,2}}{u_{x,4} - u_{x,2}} \right] (y(4) - y(2)) \quad (\text{A.16})$$

for zero velocity in the x -direction (Fig. A.1c). Next, the velocities of these interpolated points are calculated for use in the final interpolation of the position of zero tangential velocity that identifies the centre of the tornado. The velocity in the x -direction between points 1 and 2 is interpolated using

$$u_{x,12} = u_{x,1} + \left[\frac{x_{12} - x(1)}{x(2) - x(1)} \right] (u_{x,2} - u_{x,1}) \quad (\text{A.17})$$

and 3 and 4 by

$$u_{x,34} = u_{x,3} + \left[\frac{x_{34} - x(3)}{x(4) - x(3)} \right] (u_{x,4} - u_{x,3}) \quad (\text{A.18})$$

for zero velocity in the y -direction, and then the interpolation of the y -position between points 1 and 3 by

$$u_{y,13} = u_{y,1} + \left[\frac{y_{13} - y(1)}{y(2) - y(1)} \right] (u_{y,2} - u_{y,1}) \quad (\text{A.19})$$

and 2 and 4 by

$$u_{y,24} = u_{y,2} + \left[\frac{y_{24} - y(2)}{y(4) - y(2)} \right] (u_{y,4} - u_{y,2}). \quad (\text{A.20})$$

Hence, the x and y positions of zero tangential velocity between these calculated velocities can be interpolated to identify the centre of the tornado (Fig. A.1e)

$$\begin{aligned} x &= x_{12} + \left[\frac{0 - u_{x,12}}{u_{x,34} - u_{x,12}} \right] (x_{34} - x_{12}) \\ y &= y_{13} + \left[\frac{0 - u_{y,13}}{u_{y,24} - u_{y,13}} \right] (y_{24} - y_{13}) \end{aligned} \quad (\text{A.21})$$

which concludes the searching portion of the algorithm (Fig. A.1f).

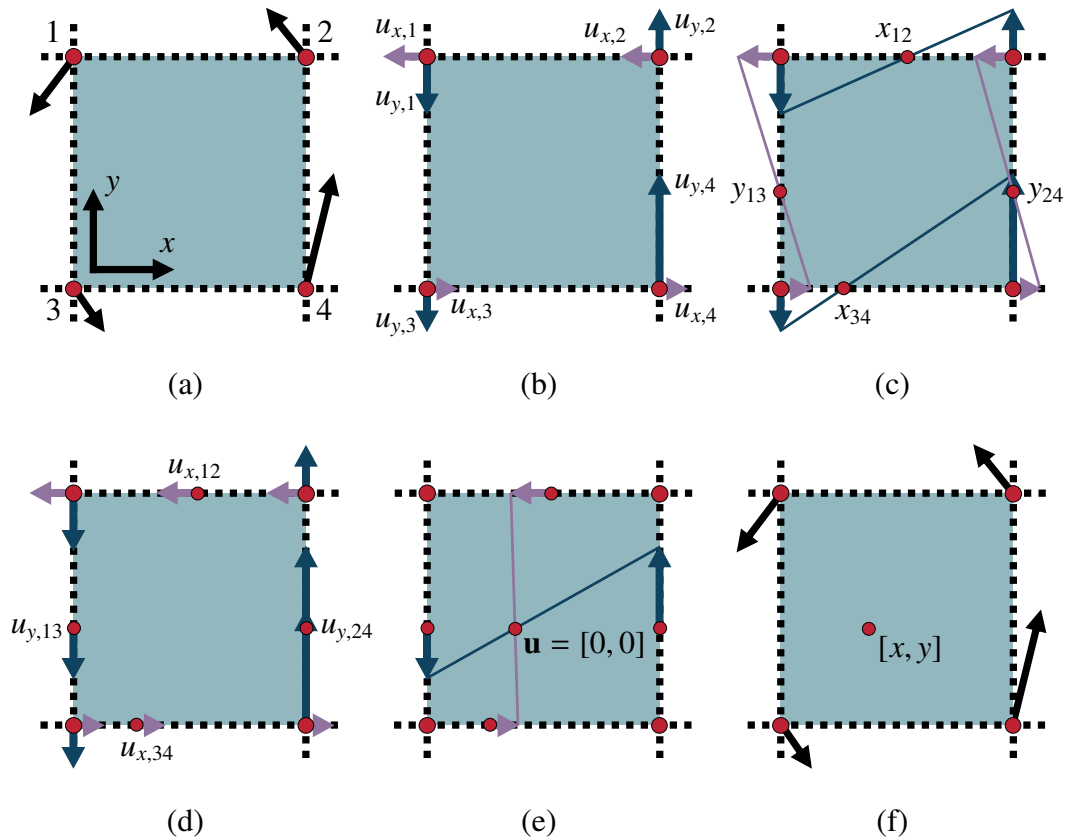


Figure A.1: Finding the tornado centre using artificial data for illustrative purposes as an example. (a) Schematic example of tornado dataset with vectors (shown as black arrows) on an isotropic grid (shown as dashed lines), (b) vector components (x in purple and y in blue), (c) location of zero velocity (between x components in purple and y components in blue), (d) interpolated vector components, (e) location of zero horizontal velocity (shown as red circle), and (f) tornado centre location

B Comparison of Scale Factor, c

To test the effects of changing the number of points selected in the maximum curl identification process, c was varied from 1 to 10, as an integer only for simplicity, and, based on trial-and-error, was found to be an appropriate range. Although the overall effect of changing this value appears to be minimal, selecting an extreme value in this range will quickly deteriorate the accuracy of the centre detection capabilities of the proposed method and increase the chance of another smaller, less-defined vortex being included in the search (see Table B.1).

c Value	Number of Re-attempts	Number of Failed Attempts	Failure Rate (%)
1	19	268	20.60
2	11	65	5.00
3	5	14	1.00
4	5	1	0.08
5	5	1	0.08
6	3	1	0.08
7	4	1	0.08
8	4	1	0.08
9	5	3	0.23
10	6	4	0.31

Table B.1: Comparison of the number of times the program failed to find a loop about a centre and/or interpolate for a centre using different c values

An optimum value of $c = 6$ was determined for the current data based on the least number of errors and re-attempts, even though a non-integer value may be optimal. The paths determined for each different c -value can be seen in Fig. B.1. Adjusting c appears to only affect the searching algorithm negatively at either end of the range selected. This is because it begins to either exclude so many points that almost none are left for the analysis or, at the other extreme, include so many points that the selection criterion of maximum curl

becomes meaningless. This scaling factor acts as a tool to eliminate the many data points identified as having a high curl but that only represent partially formed or small vortices and would otherwise skew the centre locating of the program. It should only need to be adjusted once by the user for a given dataset before proceeding with further analyses.

The searches performed neglected the results of the search from each preceding timestep, resulting in errors introduced by sweeping through the entire domain unnecessarily. Given the high spatial and temporal resolution of the dataset used in this paper, the search domain after the centre is successfully located the first time may be reduced to a very small region and carried through to each subsequent timestep processed.

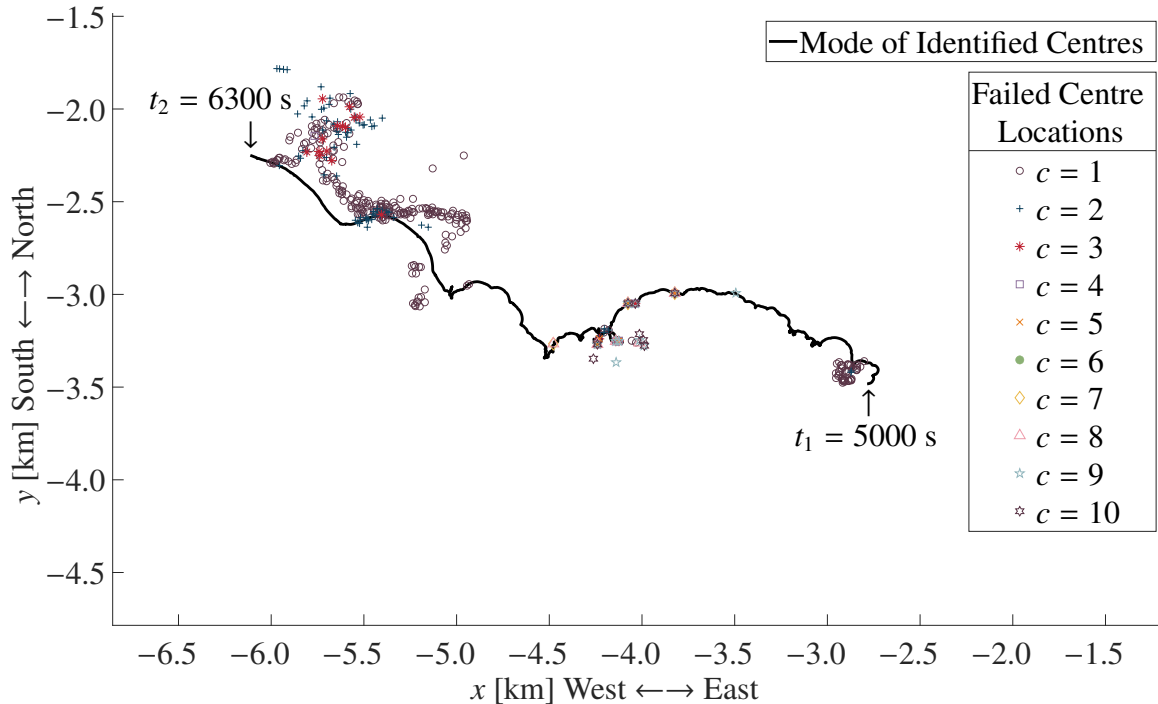


Figure B.1: Comparing the mode of identified tornado centre points, found by varying c , with the failed results of the different c values used. The data shown are taken relative to the simulation domain for all timesteps at height $z = 15$ m a.g.l.

C TKE and TI Analyses Without Temporal Smoothing

The temporal smoothing of data through use of a window size, n_w , is neglected here and instead the raw signal is only time-averaged over the given time-block length, t_b . This is presented as a point of comparison with the windowing and in general appeared to cause an increase in the values computed over all of the analyses.

First, the ratio of the SGS TKE to the grid-scale TKE (Fig. C.1) showed a much lower proportion of SGS to grid-scale for all locations and both tornadoes, an average change of about 5–10% from the windowed quantities.

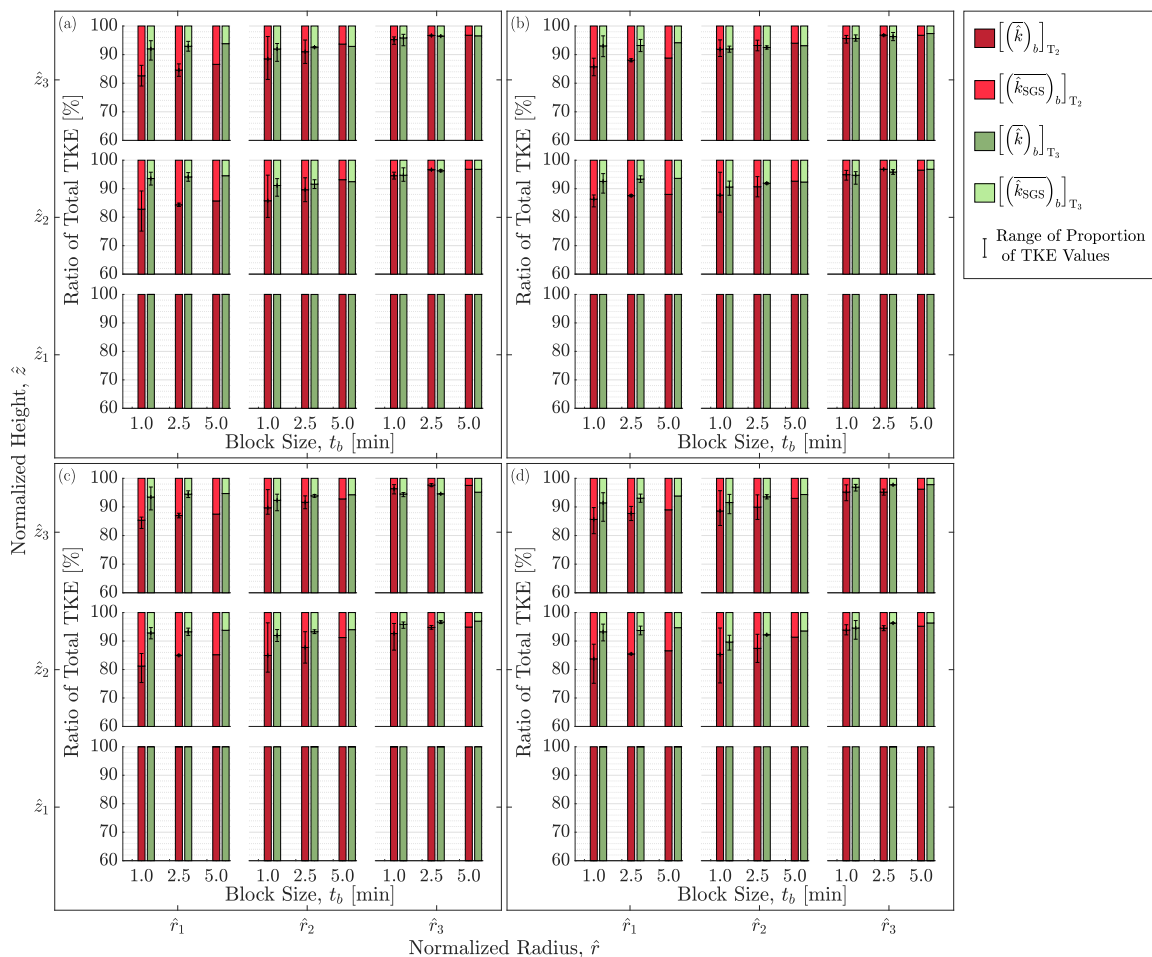


Figure C.1: Non-smoothed grid-scale and SGS TKE as a proportion of the total TKE averaged over different time-block lengths and shown at various vertical and radial locations surrounding the vortex at (a) north, (b) east, (c) south, and (d) west of the tornado centre

The relative change in values was still such that there was less contribution of the SGS TKE with an increase in t_b and \hat{r} . Just as for the windowed cases, there was more contribution of SGS TKE for T_2 than in T_3 , in general. Again, the reader must note that the ground level SGS was nearly negligible but only as an artefact of the limitations in the parent simulation at the ground boundary. Thus, looking at \hat{z}_2 and \hat{z}_3 , the average SGS TKE made up approximately 5–20% of the total TKE with a bias towards the lower side of that range.

The total TKE without temporal window smoothing applied to it can be seen in Fig. C.2. As explained previously, the \hat{k} for T_1 does not include the SGS TKE and should be regarded with caution, as described in the smoothed case results (see Sect. 3.3). It is clear that the total TKE values were much larger than in the smoothed case, at all locations and for all time-blocks. The values were seemingly slightly more dependent on the height than in the smoothed case, but this depended on the Cardinal position. For example, the west and east locations seem to show a growth of 0.10 from the first to last \hat{z} location for \hat{r}_1 for T_2 but the exact opposite for T_3 . Overall, the values appear to be, as for the smoothed cases, much lower at \hat{r}_2 than otherwise. The extreme values appeared to be even more extreme than before, so for a lower windowing value it would be prudent to take care in the normalization process. The values for T_1 were, on average, between 0.05 and 0.15. For T_2 , this range was between 0.10 and 0.70 but with a bias towards the lower end of the range. For T_3 , this range was between 0.10 and 0.50 with, again, a bias towards the lower end.

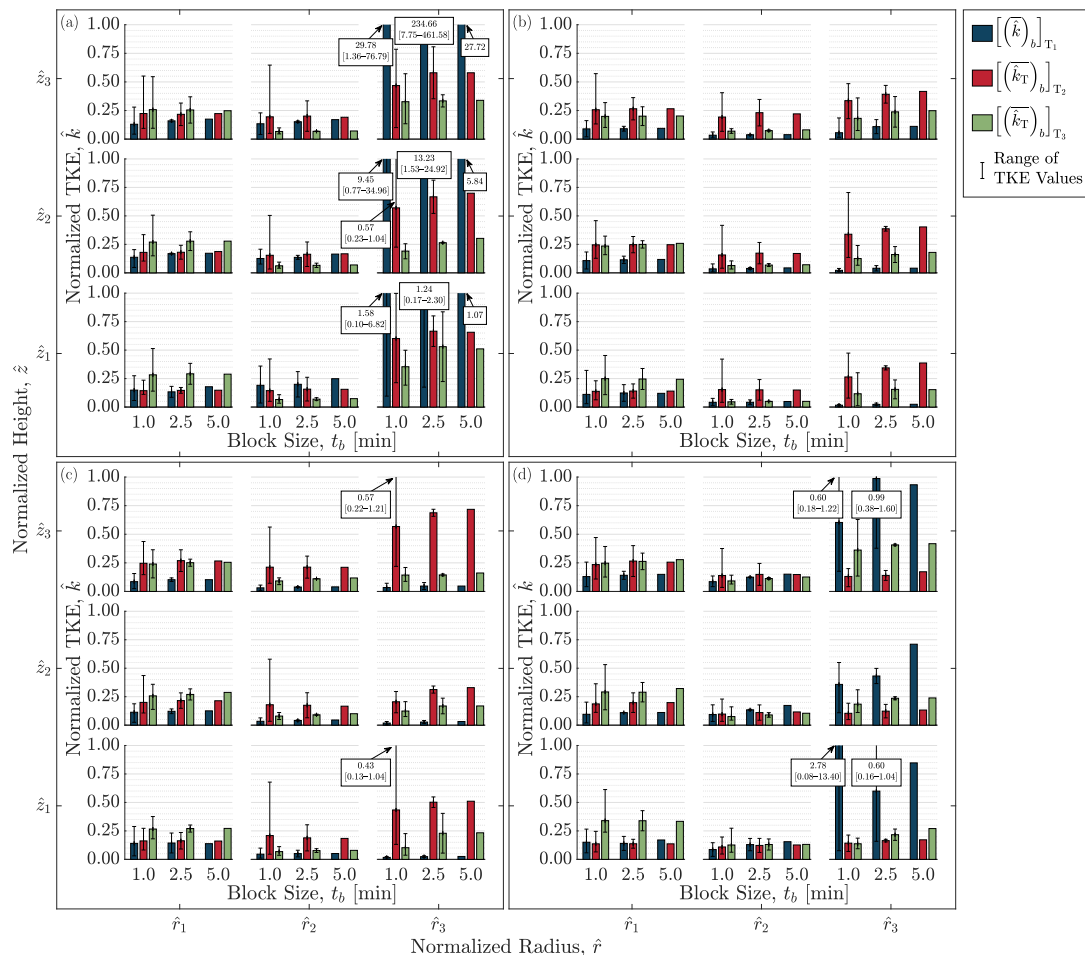


Figure C.2: Non-smoothed statistics of the normalized total TKE, \hat{k}_T , averaged over different time-block lengths and shown at various vertical and radial locations surrounding the vortex at (a) north, (b) east, (c) south, and (d) west of the tornado centre

Finally, the non-smoothed TI were plotted in Fig. C.3. Unlike for the TKE, the TI values were only moderately in the non-smoothed case, usually within 5–10% of the \hat{I} value in the smoothed case¹. Notable exceptions to that can be seen north of the vortex and for \hat{r}_3 where, again, the normalization process seems to be particularly sensitive to the relative decrease in u_t in the velocity vector magnitude compared to the other components. Unlike for the non-smoothed TKE, however, there seemed to be little change in TI with height for any of the cases and, other than the outliers, no dependence on the Cardinal location either.

¹Not relative to each other, but in terms of the TI quantity itself.

Here, unlike in the smoothed case, there seemed to be much less drop in TI at \hat{r}_2 resulting in fairly constant values no matter the radial or vertical position. On average, the TI for T_1 was between 15 and 50%, for T_2 between 20 and 35%, and for T_3 between 15 and 30%. With the latter two datasets having no TI value larger than 50% and in general tended to be closer in value to the lower end of the ranges given.

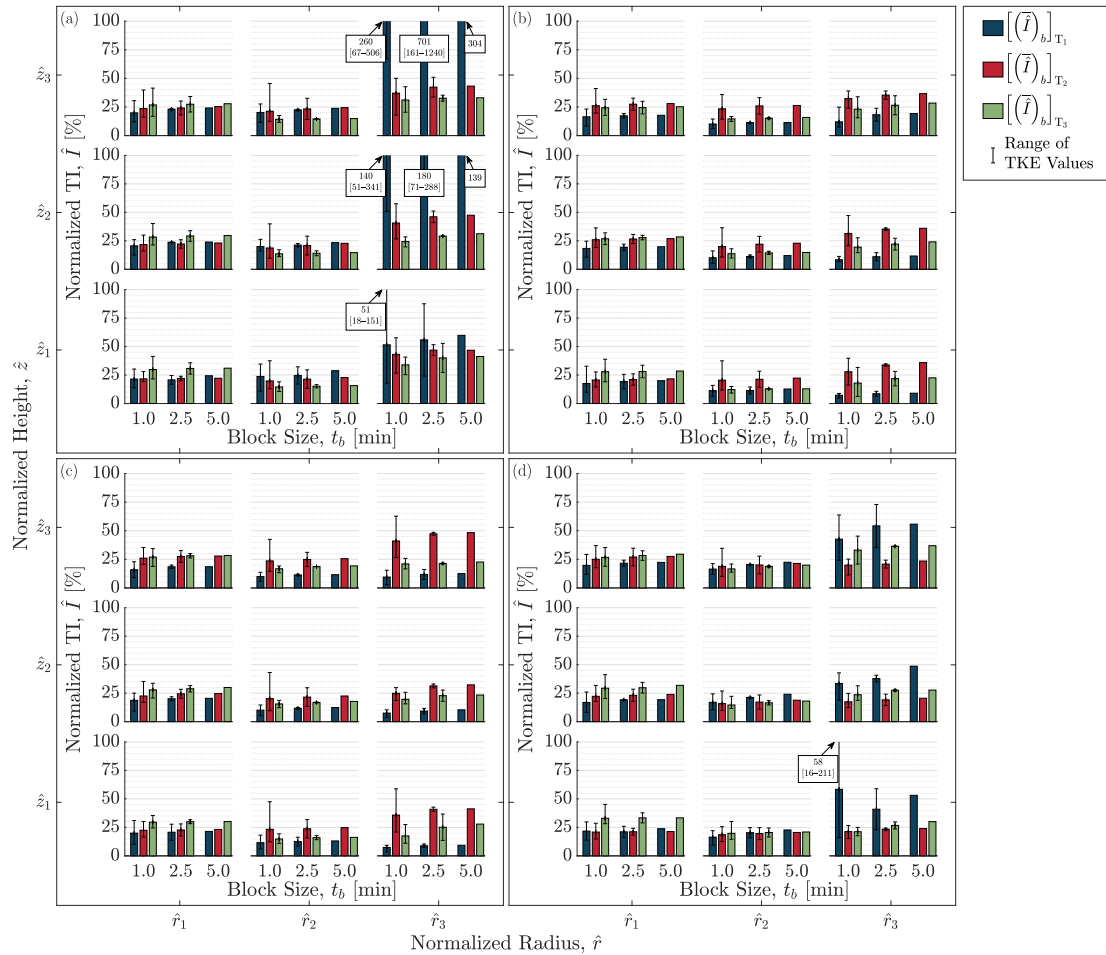


Figure C.3: Non-smoothed statistics of the TI across different time-block lengths and positions, vertically and radially, surrounding the vortex at (a) north, (b) east, (c) south, and (d) west of the tornado centre

Curriculum Vitae

Name: Niall Bannigan

Post-Secondary Education and Degrees: University of Western Ontario
London, ON, Canada
2016–2020 B.E.Sc.

University of Western Ontario
London, ON, Canada
2018–2021 B.Sc.

University of Western Ontario
London, ON, Canada
2021–2024 M.E.Sc.

Honours and Awards: Ontario Graduate Scholarship (Opted to Decline)
2021–2022

Canada Graduate Scholarship–Master’s Award
2021–2022

Ontario Graduate Scholarship
2022–2023

Related Work Experience: Teaching Assistant
The University of Western Ontario
2021 - 2023

Publications:

Bannigan, N., Orf, L., Savory, E., 2022. Developing More Accurate Models of Tornados [Paper presentation]. *Proceedings of the Canadian Society for Mechanical Engineering International Congress 2022*, Edmonton, Alberta, Canada.

Bannigan, N., Orf, L., Savory, E., 2023. Tracking the centre of asymmetric vortices using wind velocity data fields. *Boundary-Layer Meteorology* 186, 1–26.